FROM LAB TESTING TO SCIENCE: APPLYING SAPHIRA HGCDTE L-APD DETECTORS TO ADAPTIVE OPTICS

A DISSERTATION SUBMITTED TO THE GRADUATE DIVISION OF THE UNIVERSITY OF HAWAIʻI IN PARTIAL FULFILLMENT OF THE REQUIREMENTS FOR THE DEGREE OF

DOCTOR OF PHILOSOPHY

IN

ASTRONOMY

August 2018

By
Sean B. Goebel

Dissertation Committee:

Donald Hall, Chairperson
Olivier Guyon
Mark Chun
Andrew Howard
Michael Connelley
John Learned

We certify that we have read this dissertation and that, in our opinion, it is satisfactory in scope and quality as a dissertation for the degree of Doctor of Philosophy in Astronomy.

DISSERTATION COMMITTEE

_____

Chairperson

_____

_____

_____

_____

_____

Acknowledgments

Sean gratefully thanks his advisors, Donald Hall and Olivier Guyon, for the time and expertise they have shared with him and the innumerable questions they have answered.

Sean greatly appreciates the contributions to the papers presented in the following pages by his co-authors. He thanks Shane Jacobson, without whom none of the cameras and equipment would work. He expresses his gratitude to Charles Lockhart and Eric Warmbier for tirelessly working on the Pizza Box readout electronics outside their work duties and troubleshooting the late-night crises of his observing runs.

Sean particularly thanks his parents for putting up with him as a weird child, supporting his university education, and continuing to care for him as a (still weird) adult.

Abstract

Due to their high frame rates, high sensitivity, low noise, and low dark current, SAPHIRA detectors provide new capabilities for astronomical observations. The SAPHIRA detector is a 320×256@24 μm pixel HgCdTe linear avalanche photodiode array manufactured by Leonardo. It is sensitive to $0.8-2.5$ μm light. Unlike other near-infrared arrays, SAPHIRA features a user-adjustable avalanche gain, which multiplies the photon signal but has minimal impact on the read noise. This enables the equivalent of sub-electron read noise and therefore photon-counting performance, which has not previously been achieved with astronomical near-infrared arrays. SAPHIRA is intended for high clocking speeds, and we developed a new readout controller to utilize this capability and thereby enable the high frame rates ($\sim$ 400 Hz for the full frame or $\sim$ 1.7 kHz for a 128×128 pixel subarray). Beginning with the first science-grade SAPHIRA detectors and continuing with later improved devices, we deployed SAPHIRAs to the SCExAO instrument at Subaru Telescope. SCExAO is an extreme adaptive optics instrument intended for observations of high-contrast objects such as debris disks and extrasolar planets. While at SCExAO, we demonstrated the ability of SAPHIRA to function as a focal-plane wavefront sensor, and we performed extensive studies of speckle evolution. Our demonstration of SAPHIRAs ability to wavefront sense behind pyramid optics contributed to the decision to select a SAPHIRA detector and pyramid optics for the facility-class Keck Planet Imager. Additionally, we utilized the high Strehl provided by SCExAO to characterize the morphology of the HIP 79977 debris disk. Due largely to our characterization of the performance of SAPHIRA

detectors and our demonstration of their capabilities, numerous facilities throughout the world have recently proposed to use them in instruments currently in development.

Table of Contents

Acknowledgements iv

Abstract v

List of Tables ix

List of Figures x

Chapter 1: Introduction 1

1.1 Adaptive Optics 1

1.2 The SAPHIRA Detector 6

1.3 Lab Testing and Deployments of SAPHIRA 11

1.4 Future Work Building upon Our Foundation 15

1.5 From Lab Testing to Science: a Road Map to the Chapters Ahead 16

Chapter 2: Overview of the SAPHIRA Detector for AO Applications 22

2.1 Introduction 23

2.2 Readout Modes 26

2.2.1 Sampling Up-the-ramp Mode 27

2.2.2 Read-reset-read Mode 28

2.2.3 Read-reset Mode 29

2.2.4 Comparison of the Readout Modes 31

2.3 Subarray Operation and Calculation of Frame Rate 33

2.4 Radio Frequency Noise and Cryogenic Preamplifiers 38

2.5 Avalanche Gain, Charge Gain, and the Excess Noise Factor 39

2.6 Conclusions 43
Chapter 3: Commissioning of cryogenic preamplifiers for SAPHIRA detectors 48
3.1 Introduction 49
3.2 SAPHIRA without Preamplifiers 51
3.3 The ANU Preamplifier 55
3.4 Lab Testing 56
3.5 SCExAO Deployment 58
3.6 Conclusions 61
Chapter 4: Measurements of Speckle Lifetimes in Near-Infrared Extreme Adaptive Optics Images for Optimizing Focal Plane Wavefront Control 66
4.1 Introduction 67
4.2 Experimental Setup and Observations 69
4.3 Speckle Lifetime Measurements for Real-Time Speckle Nulling 73
4.3.1 The Benefits and Techniques of Real-Time Speckle Nulling 73
4.3.2 Our Observations and their Interpretation 75
4.4 A different approach: extending the analysis of Milli et al. 82
4.4.1 Milli et al.'s Technique and Results 82
4.4.2 Analysis of Our Data Using this Technique 83
4.5 Conclusions 89
Chapter 5: SCExAO/CHARIS Near-IR High-Contrast Imaging and Integral Field Spectroscopy of the HIP 79977 Debris Disk 96
5.1 Introduction 97
5.2 SCExAO/CHARIS Data 99
5.2.1 Observations and Data Reduction 99
5.2.2 Detection of the HIP 79977 Debris Disk 102
5.3 Geometry of the HIP 79977 Debris Disk 103
5.4 Modeling of the HIP 79977 Debris Disk 105
5.4.1 Methodology 105

5.4.2 Results 111
5.5 HIP 79977 Disk Surface Brightness Profile and Colors 113
5.6 Discussion 115
Appendix: The Codes used to Produce the Preceding Results 136

List of Tables

2.1 Comparison of noise sources for different SAPHIRA read modes 32

2.2 SAPHIRA clocking timings 37

4.1 A summary of observations. 71

5.1 The grid of synthetic model disks used in our forward modeling. 110

5.2 Scattered Light Resolved Debris Disks Around 5-30 Myr old Stars 119

5.3 Table 5.2 Continued. 120

List of Figures

1.1 Schematic diagram of an adaptive optics system 3

1.2 Photograph of the SAPHIRA detector 7

1.3 Schematic diagram of the SAPHIRA avalanche multiplication process . . . 8

1.4 SAPHIRA cutaway diagram 9

1.5 The author and SAPHIRA camera at SCExAO 14

2.1 The problem with read-reset-read mode 30

2.2 SAPHIRA temporal settling 34

2.3 Image and power spectrum of radio frequency noise 40

2.4 SAPHIRA integrating node capacitance plotted against bias voltage 42

3.1 Image and power spectrum of radio frequency noise. 53

3.2 Photograph of SAPHIRA camera deployed to SCExAO 54

3.3 Photograph of the detector carrier board of the ANU preamplifier 56

3.4 Laboratory volt gain measurements before and after installation of the ANU preamps 58

3.5 Oscilloscope plot of pixel settling during clocking 59

3.6 SCExAO volt gain measurements before and after installation of the ANU preamps 60

3.7 Images showing the RFI noise before installation of the ANU preamplifiers and lack thereof afterward 61

4.1 Sine waves on the deformable mirror produce speckles at the focal plane . . 74
4.2 Example PSF images before and after alignment 76
4.3 Speckle lifetime measurements on May 31, 2017 in the regimes of Extreme AO, AO188 only, and no AO 77
4.4 Speckle lifetime measurements on August 13 and 15, 2017 in Extreme AO images 78
4.5 Speckle lifetime measurements on internal source data and unilluminated images 79
4.6 Pearson's correlation coefficients for on-sky data. 85
4.7 Pearson's correlation coefficients for internal source data. 86

5.1 Improvement in observations of HIP79977 with time 101
5.2 J-, H-, and K_p-band images and SNR maps of the HIP 79977 disk 103
5.3 Region of interest used in forward modeling χ^2 calculation 107
5.4 The best-fitting synthetic disk model 112
5.5 An example χ^2 map 113
5.6 Histograms of well-fitting parameters. 114
5.7 Surface brightness profiles 116
5.8 Surface brightness profiles corrected for star color 117
5.9 No planet found 118

Chapter 1

Introduction

Abstract

This chapter contextualizes the work described in the rest of the dissertation. It provides general information about adaptive optics and the SAPHIRA detector not contained following chapters. It briefly describes the work carried out during the course of Sean Goebel's PhD, the reasons for those actions, and the ongoing efforts that are building upon those accomplishments. Finally, it provides a road map to the four papers reproduced in Chapters 2-5.

1.1 Adaptive Optics

Although an optical/infrared ground-based 8-m-class telescope collects far more light than a hobby-level 30 cm backyard telescope, it is unable to resolve greater detail in the object being observed. This is because the resolutions of both telescopes are limited by atmospheric turbulence, not diffraction from the telescope pupil. At even the best astronomical sites in the world, such as Mauna Kea, atmospheric turbulence prevents the resolving of structures with angular scales smaller than several tenths of an arcsec at visible wavelengths.

Adaptive optics (AO) is a technology which reduces the blurring effects of the atmosphere in order to regain the diffraction limit of the telescope. If the aberrated

wavefronts of light from the object being observed can be measured, it is possible to reflatten them by reflecting the light off a deformable mirror (DM) with the appropriate shape. Measuring the wavefront, calculating the correction that should be placed on the DM, and driving the mirror to this shape before the turbulence substantially changes is a major challenge; adaptive optics was first proposed by Babcock (1953), but due to computational and funding limitations, it was not actually implemented at civilian telescopes until the 1980s (see Table 1 in Beckers (1993) for a summary of these early efforts).

The basic design of an AO system is shown in Figure 1.1. After the light reflects from the deformable mirror, it is split (most commonly using a dichroic mirror which reflects certain wavelengths and is transparent to other wavelengths) and sent on different paths to the wavefront sensor and the science camera. The "science camera" is most commonly a focal-plane imager or spectrograph. The wavefront sensor consists of optical elements and a detector to receive the light from them. A real-time computer then converts the images from the detector to voltages applied to the DM. Several optical setups have been used for wavefront sensing; in decreasing order of prevalence, the most common setups used in adaptive optics are Shack-Hartmann sensors (Shack et al. 1971; Allen et al. 1988), curvature sensors (Roddier 1988), and pyramid sensors (Ragazzoni 1996; Esposito et al. 2000).

Shack-Hartmann sensors use an array of microlenses to divide the pupil into subapertures and create a spot corresponding to each. A perfect wavefront would cause the spots to have the same spacing as the microlenses; spots produced by aberrated wavefronts shift according to the local slope of the wavefront at each microlens. By measuring the shift of the spots from their unaberrated positions, the wavefront can be reconstructed. Shack-Hartmann wavefront sensors have a large linear response range, so they are well-suited for sensing highly aberrated wavefronts. However, the spot size is determined by the diffraction limit of each subaperture instead of the significantly smaller telescope aperture diffraction limit, so Shack-Hartmanns do not make the optimal use of the availble light. Curvature wavefront sensors also use microlenses, but instead of looking at the shifts of spots caused by aberrations, they measure changes in spot intensity in front of and behind the focal plane.

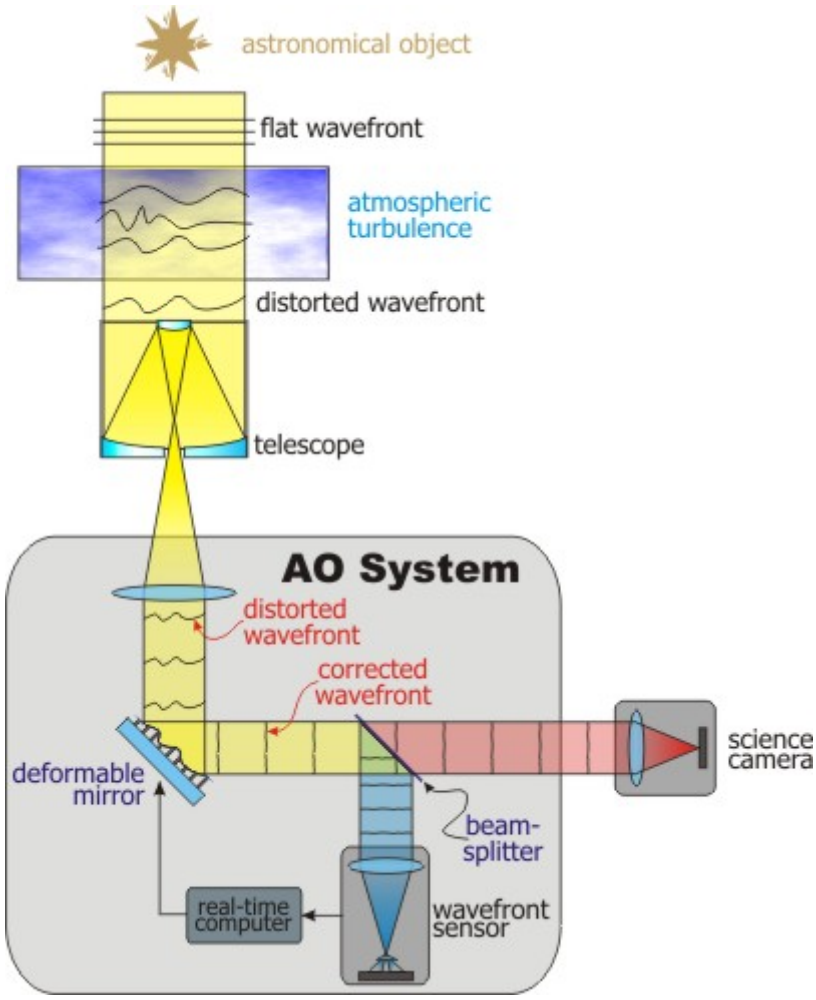

Figure 1.1 Schematic diagram of an adaptive optics system. Because astronomical objects are far away, their spherical wavefronts are effectively planar when they reach the Earth. The Earth's atmosphere distorts the wavefronts, thereby aberrating images of the object. A deformable mirror whose updates are calculated by a real-time computer's analysis of wavefront sensor data can significantly (though never perfectly) correct the wavefront. In this diagram, the wavefront sensor uses blue light and the science camera uses the red light; this is the typical setup. However, some astronomical objects (such as late-type stars or stars embedded in dust) have little optical emission. For these sorts of objects, wavefront sensing at near-infrared wavelengths would be ideal. SAPHIRA detectors are a technology that enables this. This figure is reproduced with permission from http://slittlefair.staff.shef.ac.uk/teaching/phy217/lectures/telescopes/L10.

Finally, pyramid wavefront sensors are discussed at length in this dissertation. Pyramid wavefront sensors focus the point spread function (PSF) onto the tip of a pyramid-shaped prism[1]. With the addition of refocusing optics, this produces four pupil images. Aberrations can be measured from the relative illuminations of the four pupil images; a perfect PSF would produce identical pupil images. Because these images are defined by the diffraction limit of the entire telescope pupil (instead of individual subapertures), pyramid sensors have the potential to be more sensitive than Shack-Hartmann sensors. However, pyramid sensors have a narrow range of wavefront error amplitude over which their response is linear, so they are best-suited for use in woofer-tweeter AO setups in which preliminary wavefront corrections have already been made. The range of linear response can be extended by modulating the PSF around the tip of the pyramid, but this reduces its sensitivity (Esposito & Riccardi 2001).

In addition to the optical elements, the second component of an effective wavefront sensor is a sensitive and high-speed detector. Because AO systems have update rates in the range of $\sim$ 100 Hz to $\sim$ 2 kHz, the detector needs to produce images at least this quickly. Because astronomical targets tend to be dim[2] and the frame rates necessary for adaptive optics wavefront sensing are high, relatively low signal levels are available per exposure. For this reason, detectors for wavefront sensing should have low read noise and high quantum efficiency. The detector should also have a low latency between the production of photoelectrons by incoming photons and the production of a digital signal from them, but in most cases this is not a problem.

Wavefront sensing has traditionally be done at visible wavelengths with CCD detectors, or in recent years, electron-multiplying CCDs (EMCCDs). These have high speed and quantum efficiency, and in the case of EMCCDs, can detect individual photons. Other AO instruments, such as AO188 at Subaru Telescope (Minowa et al. 2010), have used large numbers of single-pixel photodiodes. These are fast and highly sensitive, but tend to be

[1]Two rooftop prisms placed tip to tip with perpendicular orientations can also be used.

[2]If they were bright, someone else would have already observed them when the technology was less mature.

cumbersome and expensive. In both situations, the wavefront sensing is done at optical wavelengths, and the science instrument uses longer wavelengths. Wavefront sensing at optical and carrying out the science observations at near-infrared (NIR) or infrared (IR) is the most common setup for two reasons. First, the amplitude (in meters) of wavefront errors is approximately constant with wavelength, and the reduction in image quality due to aberrations scales as the wavefront error divided by the wavelength. Therefore, at longer wavelengths, a given amount of wavefront error results in a smaller impact on image quality. Because it is desirable to have as good of image quality as possible, one is motivated to place the science instrument at longer wavelengths. Second, until the research described in this dissertation was carried out, there have not existed high sensitivity, low noise, high speed, reasonable cost detector arrays sensitive to NIR wavelengths.

However, there are compelling reasons to wavefront sense at NIR wavelengths. Many targets have more emission at NIR wavelengths than at optical wavelengths, so better wavefront sensing (and therefore AO corrections) are possible if the wavefront sensing detector is sensitive to these wavelengths. Such targets include late-type stars or stars obscured by dust. If one is trying to directly image extrasolar planets in the habitable zones of their host stars, the lowest contrast and therefore most feasible targets are planets around M dwarfs (Guyon et al. 2012), which are extremely red stars and have low optical emission. Second, NIR wavefront sensing extends the performance of natural guide star AO to redder targets and expands the sky coverage available for laser guide star AO (Wizinowich et al. 2016). Finally, characterization of young stars and the dusty disks around them is an exciting and emerging area of research (e.g. Chapter 5). The optical light from the youngest of these systems is attenuated by the dust, but wavefront sensing at longer wavelengths could be possible.

1.2 The SAPHIRA Detector

The Selex Avalanche Photodiode for HgCdTe InfraRed Array (SAPHIRA) detector is the first high speed, low noise, reasonable cost array sensitive to NIR wavelengths. Therefore, it provides the potential for wavefront sensing at longer wavelengths than are possible for EMCCDs. SAPHIRA is a 320×256 pixel mercury cadmium telluride (HgCdTe) array with a 24 μm pitch and is manufactured by Leonardo (formerly SELEX). The detector is pictured in Figure 1.2.

The pixels of SAPHIRA are linear mode avalanche photodiodes (APDs), and the basic principle of their operation is illustrated in Figure 1.3. Photons shorter than 0.8 μm are unable to penetrate the CdTe substrate on the surface of the detector (a cross-section cutaway of the detector is illustrated in Figure 1.4). Photons with wavelengths of $0.8 - 2.5$ μm are absorbed in the absorption layer. Their photoelectrons diffuse to the junction and then are accelerated in the multiplication region by the bias voltage and collisionally set off avalanches of electrons. The number of avalanches that occur depends on the bias voltage applied across the multiplication region. At 1.5 V bias, there are no avalanches and SAPHIRA operates like a traditional HgCdTe array. At bias voltages of ~ 20 V, nearly 1000 electrons are produced by each detected photon. Unlike Geiger mode APDs, which need to be reset after each photon arrival (Renker 2006), SAPHIRA's output is linear with the number of incoming photons (within the detector's $\sim 10^5$ e^- dynamic range). Therefore, unlike Geiger mode APDs, there is no dead time between photon arrivals, and the detector is useful in high-flux regimes. Also, the avalanches in Geiger mode APD arrays typically emit significant amounts of glow, which effectively causes high dark current in pixels adjacent to the one experiencing the avalanche.

The avalanche process in SAPHIRA is effectively single-carrier because the holes have far lower mobility than the electrons. In other words, the electrons set off additional avalanches during their path across the multiplication region, but the holes do not cause additional avalanches. For this reason, the excess noise factor F is very near 1. F is the ratio of the

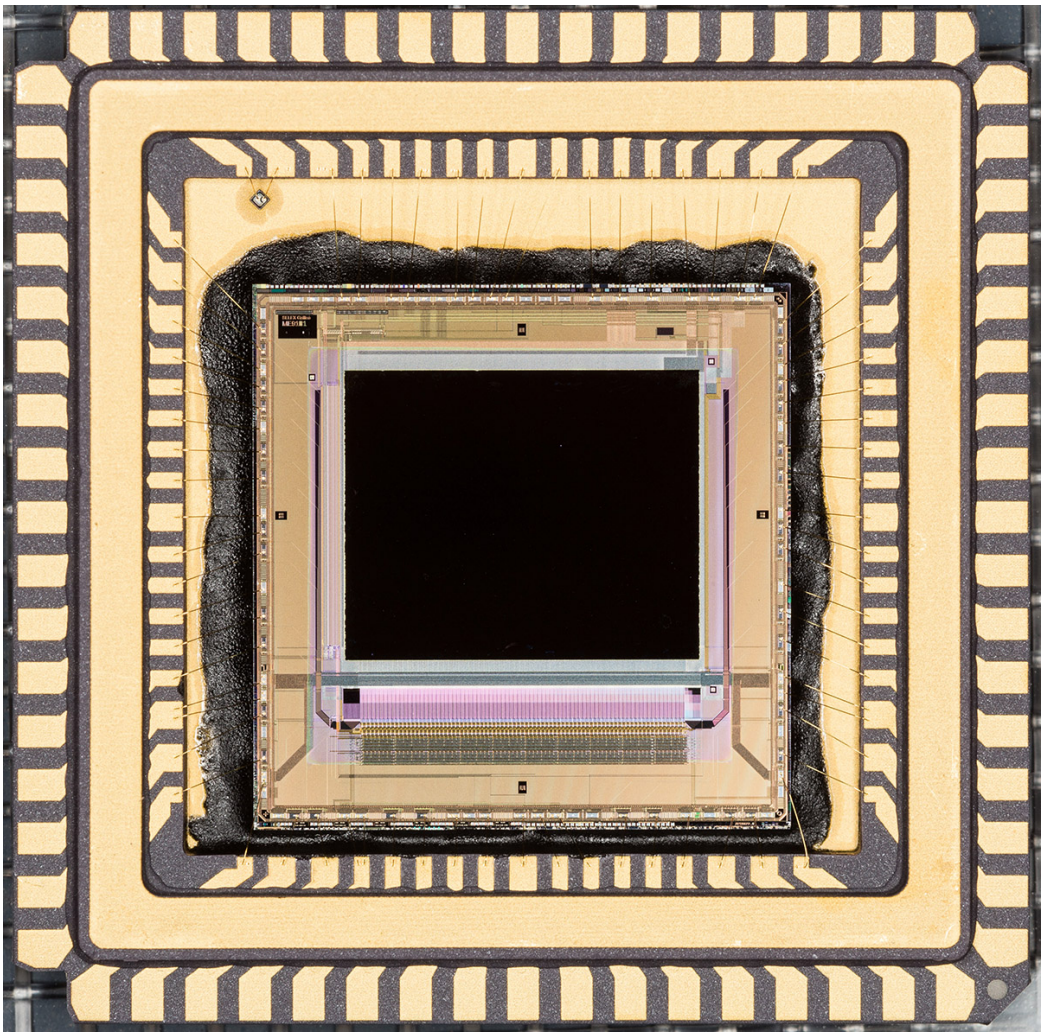

Figure 1.2 The SAPHIRA detector. The black area in the center is the HgCdTe material. Surrounding it is the read out integrated circuit (ROIC), which applies the voltages to pixels and reads and resets them. The ROIC is epoxied (black foamy material) to the leadless chip carrier (LCC) and the appropriate connections are wire bonded. The entire package in the image measures 24 mm per side.

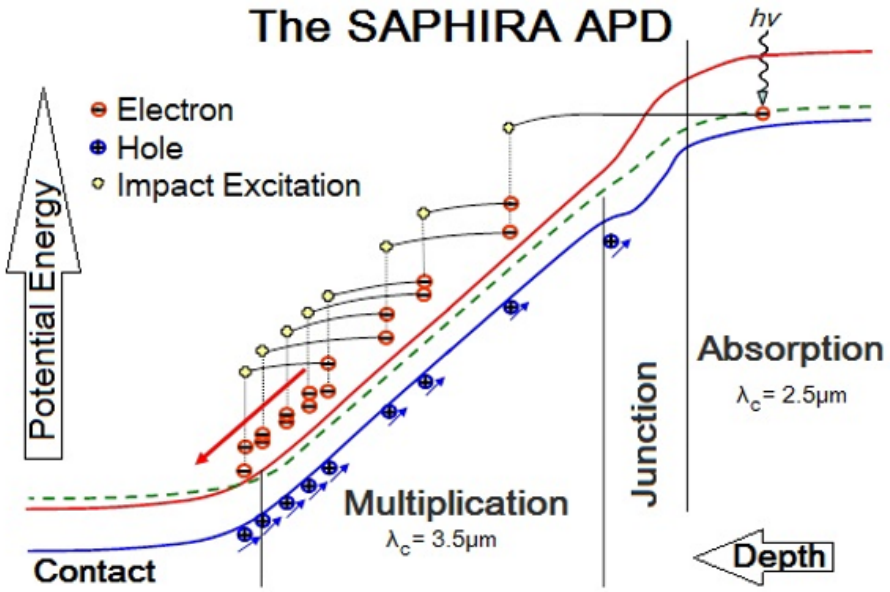

Figure 1.3 Photons deposit photoelectrons in the top right of the diagram. These diffuse to the junction and are accelerated into the multiplication region. There they are accelerated by the bias voltage and can set off avalanches of electrons. Depending on the bias voltage applied, one photoelectron can ionize up to several hundred additional electrons. These gather at the contact with the ROIC, where their total charge is read. In HgCdTe, the holes created in the avalanche process have far lower mobility than the electrons, so the avalanche process is effectively single carrier, making it extremely low noise. Since the read noise is determined by the ROIC and readout electronics, it is independent of the avalanche process. By multiplying the signal of an incoming photon and keeping the read noise fixed, it is possible to obtain the equivalent of sub-electron read noise. Photons with wavelengths of $0.8 - 2.5$ μm are absorbed in the absorption region (far right of diagram) and therefore cross the full multiplication region. However, in some cases photons with wavelengths of $2.5 - 3.5$ μm can be absorbed in the multiplication region and cause a gain-dependent and spurious signal, so it is important to use a cold filter that blocks this wavelength range of photons. This figure is courtesy of Leonardo.

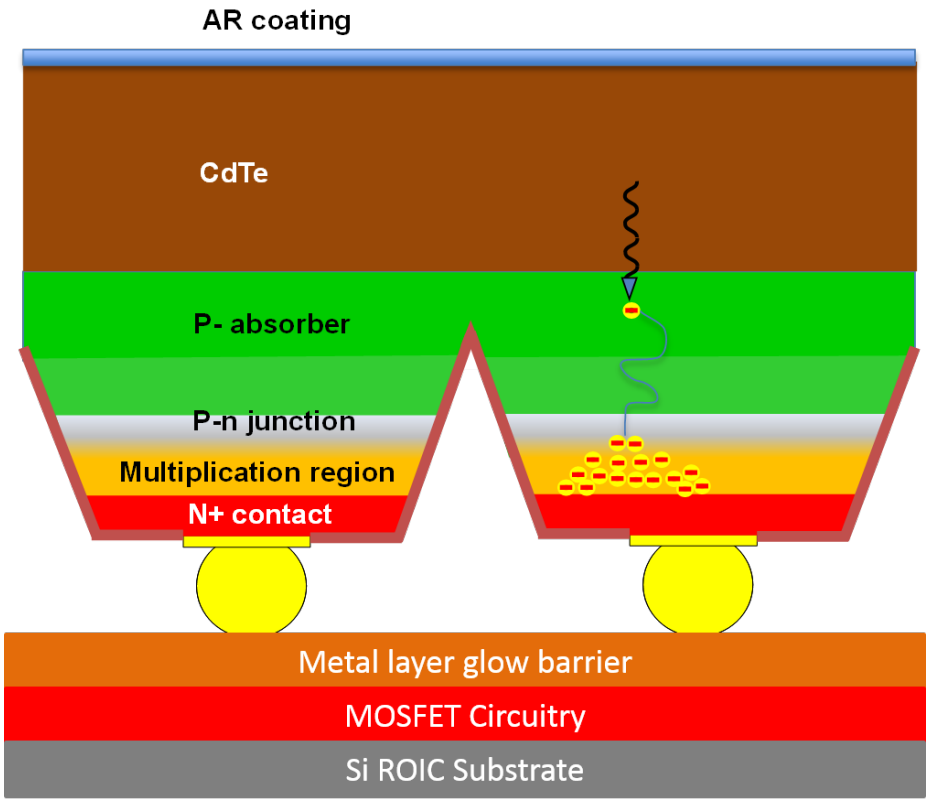

Figure 1.4 A cutaway diagram of the structure of two SAPHIRA pixels. The CdTe layer defines the 0.8 μm wavelength cutoff of SAPHIRA. The yellow dots are the indium bump bonds by which the HgCdTe structure is hybridized to the ROIC. The mesa structure (inverted pyramid shape) of the pixels is designed to prevent photoelectrons from diffusing into neighboring pixels, since there is no field in the absorption layer. It also prevents photons with wavelengths of ~ 2.5 μm from reflecting out of the pixels after entering. This figure is courtesy of Leonardo.

signal to noise of photoelectrons (before avalanche multiplication) to the signal to noise of avalanche-multiplied electrons. An ideal APD would have $F = 1$, and it has been measured to be in the range of $1 - 1.3$ (Finger et al. 2016) for SAPHIRA. On the other hand, both the holes and electrons contribute to the avalanche process in Si APDs, so they have a much larger excess noise factor than is the case for SAPHIRA.

Because the avalanche multiplication is essentially noise free and occurs prior to the reading of charge in the ROIC and digitization of the signal in the readout electronics, it does not affect the read noise. The avalanche multiplication increases the signal but has no impact on the read noise. Therefore, one can divide the read noise by the avalanche gain in order to obtain the equivalent noise without the avalanche gain; gain-corrected read noises below 1 e^- are easily achievable (Finger et al. 2016). This sub-electron read noise and the low excess noise factor F makes SAPHIRA well-suited for photon-counting operation, which previously has only been achieved at ~ 1 μm wavelengths using Geiger mode APDs and photomultiplier tubes. Both of these technologies have limited applications because they need to be reset after each photon arrival and therefore cannot accommodate high flux levels. The photon-counting capability of SAPHIRA was demonstrated by Atkinson et al. (2018).

The quantum efficiency, which is the percent of incoming photons of a given wavelength that are detected, averages $60 - 80\%$ over $0.8 - 2.5$ μm and therefore is competitive with other detectors (Finger et al. 2016). As stated previously, photons The dark current of SAPHIRA detectors is at least as good as the best other HgCdTe devices. Atkinson et al. (2017) measured the dark current as a function of temperature and detector version and provided an in-depth analysis of this. In short, the gain-corrected dark current for bias voltages of $2.5 - 8$ V is about $0.02 - 0.03$ $e^-s^{-1}pix^{-1}$ at 62.5 K for Mk. 3, 13, 14, and 19 detectors. However, this is primarily due to the ROIC glow, not intrinsic dark current in the HgCdTe material. They placed a 2σ upper bound on an intrinsic dark current of 0.0015 $e^-s^{-1}pix^{-1}$ at 62.5 K, and a similar value was reported by Hall et al. (2018). This makes SAPHIRA a highly promising detector for low-background observations, but that

capability has not been explored yet. The dark current is not a major consideration for AO applications because the individual exposures are on the order of a millisecond, so even a 1000 e^-/s/pix dark current would only produce about an electron per pixel per exposure. This is negligible compared to the signal level.

1.3 Lab Testing and Deployments of SAPHIRA

A wide variety of work with SAPHIRAs not explicitly described in the following chapters was carried out during the course of this dissertation. First, we tested tested many generations of SAPHIRA detectors. Leonardo iterated the design of the detectors by varying parameters such as the bandgap structure, doping, and anneal time. Particularly notable are the Mk. 3 and 13/14 detectors; the mark number refers to the generation number of metal organic vapour phase epitaxy (MOVPE) used to produce the detector structure. Higher numbers were later designs. The Mk. 3 detectors were the first science-grade SAPHIRAs and were delivered in late 2013; Sean joined Donald Hall's group in mid 2014. Mk. 13 and 14 detectors (these were very similar designs) were delivered in 2015 and presently remain the detectors of choice for wavefront sensing due to their excellent cosmetics and consistent behavior. A list of the SAPHIRA detectors tested by UH is given in Table 1.1 of the dissertation of Atkinson (2018). During the course of the iterations with Leonardo, the short wavelength cutoff of SAPHIRA was extended from 1.4 μm to 0.8 μm, the incidence of hot pixels was reduced, the persistence was reduced (this was noticed in a Mk. 3 array and not in any later ones), the readout integrated circuit (ROIC) glow was reduced, and the dark current was reduced. This process is ongoing; Leonardo continues to refine and improve their detector designs.

Second, we assisted with the commissioning of three SAPHIRA ROICs. The initial SAPHIRA detectors came with ME911 ROICs, which only permitted global resets. Therefore, we could only do sample up the ramp (conceptually similar to Fowler sampling) reads. This is ideal for low flux observations because the detector is read many times between each reset and the reads can be combined to minimize read noise, but it is poorly

suited for fast observations such as those needed for wavefront sensing. The first detectors with ME1000 ROICs were delivered in late 2015. This ROIC was developed by ESO and permitted line-by-line resets, which enabled new readout modes better suited for wavefront sensing applications. These modes are discussed in detail in Chapter 2. A gate was unintentionally left floating in the ME911 and ME1000 ROICs, and this caused a large amount of ROIC glow. This was noticed after the first ME1000s had been produced. The glow inhibited the performance of SAPHIRA for low-background observations and prevented measurement of its intrinsic dark current. The ME1001 ROIC was functionally identical to the ME1000, but it fixed the floating gate issue and re-stacked the metal layers above the glowing output amplifiers. This greatly reduced the glow seen by the pixels.

Third, we introduced, tested, and refined new readout electronics for operating the SAPHIRA detectors. For most lab testing and the early observatory deployments, SAPHIRA was operated using a Gen. III ARC Leach Controller (Leach & Low 2000). However, this had a fixed 265 kHz clocking rate, which enabled a $\sim$ 100 Hz frame rate for full frame SAPHIRA reads. This was inadequate for some of our SAPHIRA usages, and the SAPHIRA was designed for clocking speeds of up to 10 MHz. Additionally, the Leach controller was not compatible with line-by-line resets and therefore could not be used for read modes other than sample-up-the-ramp. Due to these limitations, the IFA developed a new, field programmable gate array (FPGA)-based readout controller affectionately called the Pizza Box. It featured clocking speeds of up to 2 MHz, supported all the SAPHIRA read modes, and utilized a USB 3.0 interface instead of the Leach controller's proprietary PCI card interface. Developing and testing the Pizza Box was a several-year effort, but they are now used with SAPHIRA detectors at SCExAO at Subaru, the Keck Planet Imager at Keck Observatory, and ROBO-AO at the Kitt Peak 1.5-m telescope, and operate a HAWAII-2RG array at the CryoNIRSP instrument at the Daniel K. Inouye Solar Telescope on Maui. The Pizza Box is also increasingly used for laboratory detector testing in Hilo, and other groups have expressed interest in deploying them.

Fourth, we solved noise problems that occurred during observatory deployments. SAPHIRA deployments prior to spring 2018 to Subaru and Keck were plagued by noise many times greater than that experienced in the lab at Hilo. This is largely because they had poor grounding (the volcanic earth of Mauna Kea is an especially poor conductor), high magnetic fields, and copious amounts of radio frequency emissions from nearby instruments. The output amplifiers of SAPHIRA struggled to drive signals stably over the $\sim$ 1 m of cables to the readout electronics, resulting in ringing and noise pickup in the cables. We collaborated with Australia National University to adapt cryogenic preamplifiers they had developed to amplify the detector's signals prior to exiting the camera. These reduced the read noise in the laboratory by nearly half and caused the noise at SCExAO to finally match that of Hilo. This effort is described in Chapter 3.

Fifth, and perhaps most importantly, we demonstrated the detectors on-sky. SAPHIRAs are fundamentally designed for astronomical work, so this was particularly fulfilling. Atkinson et al. (2014) performed the first-ever on-sky deployment of SAPHIRA at the NASA Infrared Telescope Facility, where it was used for lucky imaging. Sean Goebel dedicated most of his time to the SAPHIRA deployment at the Subaru Coronagraphic Extreme Adaptive Optics (SCExAO) instrument at Subaru Telescope (the system at that deployment is pictured in Figure 1.5). The IFA also deployed a SAPHIRA system to the ROBO-AO instrument at Palomar and then later at Kitt Peak, where it was used for tip/tilt tracking (Salama et al. 2016; Baranec et al. 2015; Jensen-Clem et al. 2018) and produced its first science publication (Han et al. 2017). We also performed a brief deployment to the Keck II telescope in preparation for a deployment in the Keck Planet Imager upgrade to NIRC2.

Sixth, we demonstrated new technologies and techniques. We performed the first-ever demonstration of pyramid wavefront sensing at NIR wavelengths (Lozi et al., in preparation). We measured speckle evolution with three orders of magnitude higher temporal resolution than previously had been done at NIR wavelengths and developed a new method to quantify speckle lifetimes (Chapter 4). We demonstrated the usefulness

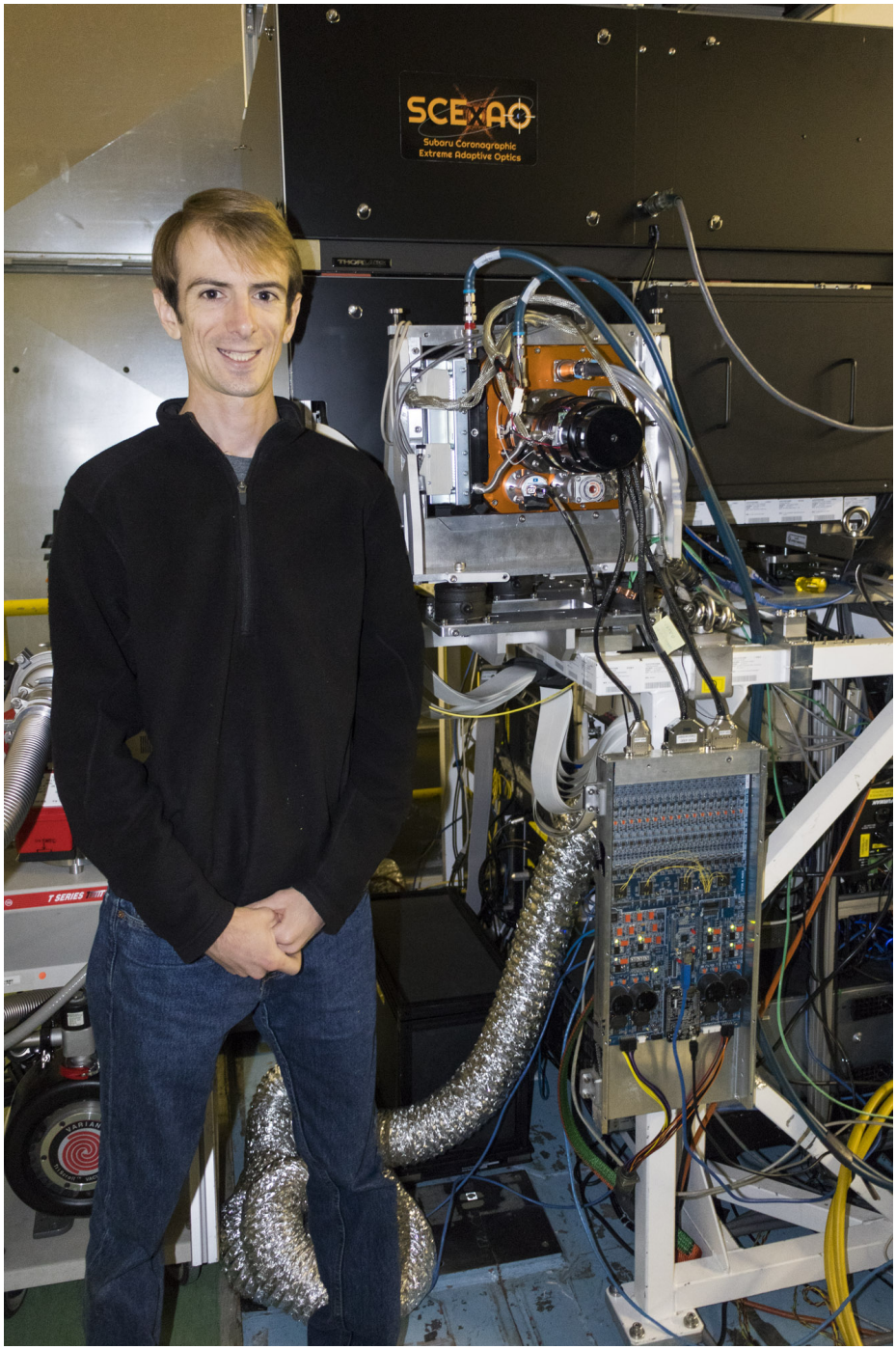

Figure 1.5 The author with the SAPHIRA system at the SCExAO instrument at Subaru Telescope. The SAPHIRA is housed inside the orange Sterling-cooled cryostat (SCC), and it is read by the FPGA-based "Pizza Box" readout electronics below it. Normally the Pizza Box is covered for protection.

of SAPHIRA for focal-plane wavefront sensing by connecting it to the speckle nulling loop originally developed by Martinache et al. (2014). SAPHIRA provided high frame rate images during the testing of a new vector apodizing phase plate coronagraph developed by Otten et al. (2017). Finally, as previously stated, we commissioned the Pizza Box readout electronics and ANU cryogenic preamplifiers.

1.4 Future Work Building upon Our Foundation

Our efforts described in Section 1.3 and the following chapters laid the foundation for future work utilizing the new capabilities of SAPHIRA detectors. Due to our demonstrations of SAPHIRA's ability to perform focal plane and pyramid wavefront sensing and our characterization of its speed and noise performance, Keck has chosen to use the detector in the Keck Planet Imager upgrade to NIRC2 (Mawet et al. 2016). The instrument is currently undergoing lab testing in Hilo and will be deployed to Mauna Kea in fall 2018 (Mawet et al. 2018).

There are two parallel efforts to develop new SAPHIRA formats. Due to its extremely low dark current, the detector offers great promise for low-background imaging. The NASA ROSES ARPA has funded the development of a 1024×1024@15 μm pixel SAPHIRA array and new ROIC to accommodate it (Hall et al. 2016, 2018). This array will incorporate reference pixels for improved common-mode noise reduction. Reference pixels have proven extremely useful for reducing noise in HAWAII devices (Rauscher et al. 2011), but have not been present on SAPHIRA detectors tested so far. The first of these larger format SAPHIRA devices will be delivered to the IFA in late 2018. These will have 16 outputs (half that of the current, smaller SAPHIRAs) in order to make them three-side close buttable. These detectors prioritize low noise and dark current at the expense of speed. Second, a consortium of ESO, Max Planck Institute, and Herzberg (Canada) is pursuing the development of a 512×512@24 μm pixel SAPHIRA detector with 64 outputs (Ian Baker, private communication). This detector is intended for high speed operation, and

the ordering of the channels will be optimized for pyramid wavefront sensing. The 320×256 pixel SAPHIRAs are well-sized for wavefront sensing on current 8-10-m-class telescopes, but the 512×512 size is ideal for the upcoming 30-m-class telescopes.

A number of instruments currently in development have proposed to employ SAPHIRA detectors. The Magdalena Ridge Observatory Interferometer in New Mexico has proposed to replace their PICNIC detector with a SAPHIRA for fringe tracking because SAPHIRA's improved sensitivity reduces the opto-mechanical requirements of the instrument (Ligon et al. 2018). The Giant Magellan Telescope will use a SAPHIRA in its Acquisition, Guiding, and Wavefront Sensing instrument in order to phase the mirrors to 50 nm accuracy (Kopon et al. 2018). A commercially-available C-RED ONE SAPHIRA camera (Greffe et al. 2016), produced by First Light Imaging, has been purchased for the CHARA array at Mt. Wilson, CA. This will be used in a K-band interferometer which combines the beams from six telescopes for high-resolution imaging of disks around young stars (Lanthermann et al. 2018). The ESO Extremely Large Telescope will use at least one SAPHIRA for low- and high-order wavefront sensing with natural guide stars in the inFraRED cAmera (FREDA) module[3] (Downing et al. 2018). These instruments have published in the SPIE proceedings their intent to use SAPHIRA detectors; there likely are additional proposals.

1.5 From Lab Testing to Science: a Road Map to the Chapters Ahead

The ensuing chapters are ordered such that their topics cross the spectrum from engineering to science. Chapter 2 provides an overview of the SAPHIRA detector and discusses a variety of considerations that must be taken into account when the detector is employed for wavefront sensing. Chapter 3 describes efforts to reduce the noise and increase the clocking speeds in SAPHIRA arrays. These characteristics were particularly limiting at the SCExAO instrument. Chapter 4 describes measurements of speckle temporal evolution in extreme AO

[3]This dissertation grants FREDA the award for the most forced acronym contained within its pages.

images and their implications for observations. Chapter 5 contains characterization of the morphology of the HIP 79977 debris disk that was made possible by the extreme adaptive optics corrections of SCExAO. These four chapters also appear as journal publications. Lastly, Appendix A links to an online database of the codes used to produce the results contained in this dissertation and contains brief descriptions of them.

References

Allen, J. G., Jankevics, A., Wormell, D., & Schmutz, L. 1988, in Society of Photo-Optical Instrumentation Engineers (SPIE) Conference Series, Vol. 739, 124–128

Atkinson, D. 2018, ArXiv e-prints

Atkinson, D., Hall, D., Baranec, C., Baker, I., Jacobson, S., & Riddle, R. 2014, in Proceedings of the SPIE, Volume 9154, id. 915419 12 pp. (2014)., Vol. 9154, 915419

Atkinson, D., Hall, D., Jacobson, S., & Baker, I. M. 2018, AJ, 155, 220

Atkinson, D. E., Hall, D. N. B., Jacobson, S. M., & Baker, I. M. 2017, AJ, 154, 265

Babcock, H. W. 1953, Publications of the Astronomical Society of the Pacific, 65, 229

Baranec, C., Atkinson, D., Riddle, R., Hall, D., Jacobson, S., Law, N. M., & Chun, M. 2015, ApJ, 809, 70

Beckers, J. M. 1993, Annual Review of Astronomy and Astrophysics, 31, 13

Downing, M., Casali, M., Marchetti, E., Mehrgan, L., Amico, P., Reyes, J., Brinkmann, M., Conzelmann, R., Geimer, C., Molina-Conde, I., Stegmeier, J., & Todorovic, M. 2018, in Proc. SPIE 10703-69, Adaptive Optics Systems VI (to be published)

Esposito, S., Feeney, O., & Riccardi, A. 2000, in Adaptive Optical Systems Technology, Vol. 4007, 416–422

Esposito, S. & Riccardi, A. 2001, A&A, 369, L9

Finger, G., Baker, I., Alvarez, D., Dupuy, C., Ives, D., Meyer, M., Mehrgan, L., Stegmeier, J., & Weller, H. J. 2016, in Proc. SPIE, Vol. 9909, Adaptive Optics Systems V, 990912

Greffe, T., Feautrier, P., Gach, J.-L., Stadler, E., Clop, F., Lemarchand, S., Boutolleau, D., & Baker, I. 2016, in Proc. SPIE, Vol. 9907, Optical and Infrared Interferometry and Imaging V, 99072E

Guyon, O., Martinache, F., Cady, E. J., Belikov, R., Balasubramanian, K., Wilson, D., Clergeon, C. S., & Mateen, M. 2012, in Adaptive Optics Systems III, Vol. 8447, 84471X

Hall, D. N. B., Baker, I., & Finger, G. 2016, in High Energy, Optical, and Infrared Detectors for Astronomy VII, Vol. 9915, 99150O

Hall, D. N. B., Baker, I. M., Isgar, V., Jacobson, S. M., & Weller, H. 2018, in Proc. SPIE 10709-62, High Energy, Optical, and Infrared Detectors for Astronomy VIII (to be published)

Han, E., Muirhead, P. S., Swift, J. J., Baranec, C., Law, N. M., Riddle, R., Atkinson, D., Mace, G. N., & DeFelippis, D. 2017, AJ, 154, 100

Jensen-Clem, R., Duev, D. A., Riddle, R., Salama, M., Baranec, C., Law, N. M., Kulkarni, S. R., & Ramprakash, A. N. 2018, AJ, 155, 32

Kopon, D. A., McLeod, B. A., Bouchez, A. H., Catropa, D., van Dam, M. A., D'Arco, J., Kansky, J., McCracken, K., McMuldroch, S., Podgorski, W., Close, L. M., Males, J. R., & Morzinsk, K. M. 2018, in Proc. SPIE 10703-34, Adaptive Optics Systems VI (to be published)

Lanthermann, C., Le Bouquin, J.-B., Anugu, N., Monnier, J., & Kraus, S. 2018, in Proc. SPIE 10709-41, High Energy, Optical, and Infrared Detectors for Astronomy VIII (to be published)

Leach, R. W. & Low, F. J. 2000, in Proc. SPIE Vol. 4008, p. 337-343, Optical and IR Telescope Instrumentation and Detectors, Masanori Iye; Alan F. Moorwood; Eds., Vol. 4008, 337–343

Ligon, E. R., Salcido, C. D., Buscher, D. F., Creech-Eakman, M., Haniff, C. A., Santoro, F. G., Jurgenson, C. A., McCracken, T. M., Schmidt, L. M., & Young, J. S. 2018, in Proc. SPIE 10701-61, Optical and Infrared Interferometry and Imaging VI (to be published)

Martinache, F., Guyon, O., Jovanovic, N., Clergeon, C., Singh, G., Kudo, T., Currie, T., Thalmann, C., McElwain, M., & Tamura, M. 2014, Publications of the Astronomical Society of the Pacific, 126, 565

Mawet, D., Bond, C. Z., Delorme, J.-R., Wang, J., Jovanovic, N., Cetre, S., Chun, M. R., Echeverri, D., Hall, D. N. B., Lilley, S. J., Wallace, J. K., & Wizinowich, P. L. 2018, in Proc. SPIE 10703-6, Adaptive Optics Systems VI (to be published)

Mawet, D., Wizinowich, P., Dekany, R., Chun, M., Hall, D., Cetre, S., Guyon, O., Wallace, J. K., Bowler, B., Liu, M., Ruane, G., Serabyn, E., Bartos, R., Wang, J., Vasisht, G., Fitzgerald, M., Skemer, A., Ireland, M., Fucik, J., Fortney, J., Crossfield, I., Hu, R., & Benneke, B. 2016, in Adaptive Optics Systems V, Vol. 9909, 99090D

Minowa, Y., Hayano, Y., Oya, S., Watanabe, M., Hattori, M., Guyon, O., Egner, S., Saito, Y., Ito, M., Takami, H., Garrel, V., Colley, S., Golota, T., & Iye, M. 2010, in Society of Photo-Optical Instrumentation Engineers (SPIE) Conference Series, Vol. 7736, Society of Photo-Optical Instrumentation Engineers (SPIE) Conference Series, 3

Otten, G. P. P. L., Snik, F., Kenworthy, M. A., Keller, C. U., Males, J. R., Morzinski, K. M., Close, L. M., Codona, J. L., Hinz, P. M., Hornburg, K. J., Brickson, L. L., & Escuti, M. J. 2017, ApJ, 834, 175

Ragazzoni, R. 1996, Journal of Modern Optics, 43, 289

Rauscher, B. J., Arendt, R. G., Fixen, D. J., Lander, M., Lindler, D., Loose, M., Moseley, S. H., Wilson, D. V., & Xenophontos, C. 2011, in Society of Photo-Optical Instrumentation Engineers (SPIE) Conference Series, Vol. 8155, 81550C

Renker, D. 2006, Nuclear Instruments and Methods in Physics Research A, 567, 48

Roddier, F. 1988, Appl. Opt., 27, 1223

Salama, M., Baranec, C., Jensen-Clem, R., Riddle, R., Duev, D., Kulkarni, S., & Law, N. M. 2016, in Proceedings of the SPIE, Volume 9909, id. 99091A 15 pp. (2016)., Vol. 9909, 99091A

Shack, R. V., Rancourt, J. D., & Morrow, H. 1971, Appl. Opt., 10, 257

Wizinowich, P., Chun, M., Mawet, D., Agapito, G., Dekany, R., Esposito, S., Fusco, T., Guyon, O., Hall, D., Plantet, C., & Rigaut, F. 2016, in Proc. SPIE, Vol. 9909, Adaptive Optics Systems V, 990915

Chapter 2

Overview of the SAPHIRA Detector for AO Applications

Note: this chapter originally appeared as Goebel et al. (2018), with co-authors Donald N.B. Hall, Olivier Guyon, Eric Warmbier, and Shane M. Jacobson.

Abstract

We discuss some of the unique details of the operation and behavior of Leonardo SAPHIRA detectors, particularly in relation to their usage for adaptive optics wavefront sensing. SAPHIRA detectors are 320×256@24 μm pixel HgCdTe linear avalanche photodiode arrays and are sensitive to 0.8-2.5 μm light. SAPHIRA arrays permit global or line-by-line resets, of the entire detector or just subarrays of it, and the order in which pixels are reset and read enable several readout schemes. We discuss three readout modes, the benefits, drawbacks, and noise sources of each, and the observational modes for which each is optimal. We describe the ability of the detector to read subarrays for increased frame rates, and finally clarify the differences between the avalanche gain (which is user-adjustable) and the charge gain (which is not).

2.1 Introduction

Due to their ability to detect individual photons with both high temporal and spatial resolutions, electron-multiplying CCDs (EMCCDs) have greatly improved the sensitivity limits of adaptive optics (AO) systems. However, EMCCDs are sensitive to optical wavelengths, and in most AO implementations, the science instrument operates at near-infrared wavelengths. This wavelength sensitivity difference between the wavefront sensor and science instrument occurs for two reasons. First, the path length differences introduced by atmospheric turbulence are approximately independent of wavelength, so the aberrations as a fraction of phase are reduced at longer wavelengths. Therefore, better image quality is obtained at longer wavelengths, and so the science instruments are designed to take advantage of this. Second, until now there have not existed high frame rate, low noise, reasonable cost infrared detector arrays, so it was not feasible to do high-order wavefront sensing at near-infrared wavelengths. The Selex Avalanche Photodiode for HgCdTe InfraRed Array (SAPHIRA) detector is the first such technology that enables this.

Operating the wavefront sensor at near-infrared wavelengths provides several benefits (Wizinowich et al. 2016). It has the potential to expand the sky coverage available for natural guide star sensing because it enables the observation of targets that have minimal emission at optical wavelengths, such as late-type stars or obscured objects. In particular, there is significant interest in observing nearby M dwarfs because they have favorable contrasts for directly imaging reflected-light extrasolar planets located in their habitable zones. Second, if both the science module and wavefront sensor are sensitive to similar wavelengths, they can share a greater fraction of optical elements inside the instrument and thereby minimize noncommon path errors. For these reasons, SAPHIRA detectors enable exciting new AO observing modes.

SAPHIRA arrays are well-suited for wavefront sensing because they provide two advantages over other infrared devices. First, they have a user-adjustable avalanche gain. This is discussed at length in Section 2.5, but in short, it amplifies the signal from photons

but not read noise sources. At high gains, the signal of an individual photon is greater than the read noise. If the noise is divided by the avalanche gain, it can be equivalent to $< 1e^-$. The second advantage of SAPHIRA is that all outputs are still used when reading subarrays, so greatly increased frame rates can be achieved by reading less than the full detector (Section 2.3). This is in contrast to (for example) Teledyne HAWAII detectors, in which each output reads a contiguous stripe of the detector and only a single output is used when in sub-array mode.

SAPHIRA detectors are 320×256 pixel mercury cadmium telluride arrays and have a 24 μm pixel pitch (Baker et al. 2016). They are manufactured by Leonardo (formerly called Selex) and have 32 outputs. The absorption layer (where photons are intended to be absorbed) has 0.8-2.5 μm sensitivity and is transparent at longer wavelengths. These longer wavelengths must be filtered out to avoid spurious signal from photons absorbed in the multiplication layer. The multiplication layer, which is where the avalanche multiplications occur, lies below the absorption layer and has sensitivity to 3.5 μm (Finger et al. 2016). Because SAPHIRAs are a developmental program, they are assigned mark numbers which refer to the generation of metalorganic vapour phase epitaxy (MOVPE) layer architecture; higher numbers are newer designs. Mk. 3 SAPHIRA arrays were the first science-grade ones and were delivered in 2013. The Mk. 13 and 14 arrays (which are indistinguishable for the purposes of wavefront sensing) were delivered in 2015 and (as of the time of writing) remain the best arrays for telescope deployments due to their uniform cosmetic qualities. Later generations of arrays have improved in some areas (e.g. dark current) but had problems in other areas (e.g. dead pixels or operational reliability). There are plans to produce larger format SAPHIRA arrays for low-background imaging and high-order wavefront sensing on thirty-meter-class telescopes (Hall et al. 2016b). SAPHIRA devices produced until late 2015 utilized ME911 read out integrated circuits (ROICs), which only permitted global resets and therefore were limited to up-the-ramp readout mode (Section 2.2.1). The ME1000 ROIC enabled row-by-row resets, which made possible read-reset-read and read-reset modes

(Sections 2.2.2 and 2.2.3). The ME1001 ROIC is functionally identical to the ME1000 ROIC, but it features reduced glow during operation.

While the operation of the SAPHIRA APD array is very similar to that of conventional HgCdTe arrays such as the Teledyne HAWAII series (Beletic et al. 2008) and the Raytheon Virgo (Starr et al. 2016), there are some important differences. The conventional arrays are normally operated at a bias of a few hundred mV, occasionally up to a volt, and the full bias voltage between the substrate and the node is within the dynamic range of the readout circuit. After reset, the array discharges to the substrate voltage. The depletion is modest and varies with bias voltage, and that results in a highly bias-dependent diode capacitance. In contrast, the SAPHIRA typically operated at bias voltages of $2.5 - 18$ V, way beyond the dynamic range of the readout circuit, and the node voltage is referenced to ground in the ROIC. At these bias voltages the photodiode is largely or completely depleted of electrical charge, and the response is highly linear over the dynamic range. As a result of the depletion, there is no settling of charge due to the change in electric field when the bias voltage is changed. In conventional detectors or when SAPHIRA is operated at very low bias voltage, the detector needs to be allowed to settle after changing the bias voltage.

SAPHIRA arrays are beginning to enter widespread deployments. The University of Hawaii Institute for Astronomy has extensively tested the detectors in the lab and at telescopes. Over the last several years, we have continuously deployed a SAPHIRA system to the SCExAO extreme AO instrument at Subaru Telescope, where it is primarily used for focal-plane wavefront sensing (Goebel et al. 2016). It has also been deployed short-term to the NASA Infrared Telescope Facility (IRTF) (Atkinson et al. 2014), where it obtained diffraction-limited images of binary star systems using the lucky imaging(Fried 1978) technique. Also, a SAPHIRA system is currently being integrated into the Keck II AO system in order to enable near-infrared pyramid wavefront sensing (Mawet et al. 2016). SAPHIRA is being used for fast NIR imaging on the Robo-AO instrument, which was initially deployed to the 1.5 m telescope at Palomar (Baranec et al. 2015) and then later to the 2.1 m telescope at Kitt Peak (Jensen-Clem et al. 2018). While at Robo-AO,

SAPHIRA produced its first science publication (Han et al. 2017). ESO has also been evaluating SAPHIRA arrays (Finger et al. 2012), and they are deployed to the Very Large Telescope's GRAVITY instrument for wavefront sensing at the individual telescopes and fringe tracking at the combined focus (Mehrgan et al. 2016). Lastly, First Light Imaging has developed a commercial system called C-RED One that combines the SAPHIRA detector, camera and associated cooling, and readout electronics (Greffe et al. 2016).

In this paper, we report on the operation modes and intricacies of behavior of SAPHIRAs. Unless stated otherwise, the data presented below were collected at a temperature of 85 K and at unity avalanche gain (i.e. a bias voltage of 2.5 V) with Mark 13 and 14 arrays on ME1000 ROICs.

2.2 Readout Modes

The readout modes available on SAPHIRA detectors differ according to when and the number of times that pixels are read between resets. We have operated the SAPHIRA in three different readout schemes: 1) sampling up-the-ramp mode, which utilizes an initial reset of all pixels followed by multiple reads; 2) read-reset-read mode, which reads a row of pixels, resets it, and reads it again before clocking to the next row; and 3) read-reset mode, whereby a row is read and then reset before moving to the next row, and a reference image is subtracted in order to remove the pedestal voltage (sometimes called the fixed-pattern noise or bias). These readout modes are independent of subarray size. In practice, we use read-reset mode for AO-related observations because it provides regular time sampling (unlike sample up-the-ramp mode) and better noise performance and double the frame rate compared to read-reset-read mode. In the following sections, we discuss each readout mode in turn.

2.2.1 Sampling Up-the-ramp Mode

In sampling up-the-ramp (SUTR) mode, the entire array is reset, and then it is non-destructively read a user-specified number of times (Chapman et al. 1990). These reads can be processed in one of two ways. First, the user can fit a line to the "ramp" (flux vs. time) behavior for each pixel. This removes the pedestal voltage (fixed-pattern noise) and reduces the white read noise variance as $1/N$, where N is the number of times the array is read per ramp. A mathematical analysis of SUTR (and the conceptually similar Fowler sampling) is given by Garnett and Forrest (1993) (Garnett & Forrest 1993). Additionally, if a pixel saturates partway through the ramp due to high flux or a cosmic ray strike, the reads in which the pixel is saturated can be excluded from the fit. When SUTR data are reduced by line-fitting, one "science" frame is produced for each ramp. This is well-suited for low-background observations in which read noise dominates and the exposures are long, but it is poorly suited for instances where fast analysis of the images is required (such as AO wavefront sensing).

The second way to reduce SUTR data is to subtract subsequent reads. If being used for AO wavefront sensing, this enables more frequent updates to the correction. By subtracting temporally adjacent frames, one removes the pedestal voltage and kTC (reset level) noise because it is present in both images, leaving only the flux that accumulated in the pixel between those two exposures and the read noise. However, this mode causes three challenges. First, it requires that the dynamic range be rationed across the ramp (if there are N reads per ramp, then no individual read can utilize more than $1/N$ of the dynamic range, or else the final reads of the pixel will contain no new flux). Second, there is irregular time sampling because it wouldn't make sense to subtract the read immediately before a reset from the one immediately after the reset because this would result in negative flux and kTC noise. This is problematic for applications that require regular temporal sampling. Third, due to the intrinsic nonlinearity of infrared arrays, the responsivity of the detector decreases as the pixels accumulate flux. This causes frame pairs toward the end of the ramp to incorrectly

report less flux than an equally-illuminated pair at the beginning of the ramp. One can compensate for this last effect with a standard linearity correction, however.

Often, the frame read immediately after a reset contains excess noise due to settling effects. In practice, we typically exclude the first frame following each reset from analysis. This exacerbates the irregularity of time sampling in SUTR mode and reduces its duty cycle, particularly when there are few reads between resets.

In both methods of reducing SUTR data, variations in the voltage of a pixel after one reset compared to its voltage after another reset has no effect because it is in all reads of a given ramp. This is called kTC noise because its variance is given by

$$\sigma_{kTC}^2 = k_B T C \tag{2.1}$$

where k_B is the Boltzmann constant, T is temperature, and and C is node capacitance. We typically operate the detector at $T = 85$ K, and $C = 28$ fF for SAPHIRA, so $\sigma_{kTC} \approx 36$ e^-. Unlike read noise, kTC noise is not affected by the pixel read rate. Because SUTR readouts are not affected by kTC noise, they enable the lowest noise of the readout modes discussed here. SUTR readouts are best-suited for low-background, long integrations.

2.2.2 Read-reset-read Mode

In read-reset-read mode, a row is read, reset, and then read again before clocking to the next one. The read immediately following the reset (which contains only the pedestal voltage) is then subtracted from the read preceding the next reset after scanning through the array (which contains the pedestal voltage plus flux). Therefore, there are two reads per science frame. This mode removes the effects of kTC noise.

In practice, read-reset-read mode presents two problems. First, and more importantly, settling effects immediately following the reset lead to spurious flux in the first column blocks read (a column block is a 32-pixel-wide row of pixels. These are read simultaneously.). This problem is illustrated in Figure 2.1. The amplitude of this effect varies from one SAPHIRA

array to another, and we theorize that it can be mitigated by inserting a delay between the reset and first read, though we have not tested this because it would slow the frame rate. In our typical 1 MHz clocking rates, there is only 850 ns between the end of the reset pulse and the sampling of the pixels in the first column block. Second, because there is read noise associated with both reads, these add in quadrature for the science frame. For the $\sim$ 100 kHz clocking rates used for most IR detectors, the read noise is much less than the kTC noise. However, the read noise approximately scales with the square root of the sampling frequency, and for the 1-10 MHz sampling frequencies used for SAPHIRA wavefront sensing, these two noise sources become comparable. Because of the spurious flux and replacement of kTC noise with similar-magnitude read noise, we do not commonly use read-reset-read mode.

2.2.3 Read-reset Mode

If the read noise of one frame is comparable to its kTC noise, then the correlated double sampling of read-reset-read mode (which produces an image free of kTC noise but containing read noise contributed by both frames) is no better than subtracting a reference dark frame that has been produced from averaging together many frames (and therefore contains negligible kTC and read noise) from a single read (which does contain these noise sources). The read noise depends on the sampling rate and specifics of the readout electronics, but during typical usage of SAPHIRA, it is of the same order as the 36 e^- kTC noise calculated from Equation 2.1.

In read-reset mode, the pedestal voltage of the detector is removed by averaging together many unilluminated frames and then subtracting this reference frame from each individual frame. During science operation, these dark frames can be collected before or after the data frames. However, a new reference frame needs to be collected for each bias voltage (the bias voltage controls the avalanche gain), since the pedestal voltage pattern on the detector changes with bias voltage. Read-reset mode is our standard mode for AO observations because its noise is similar or lower than that of read-reset-read mode, it produces a "science"

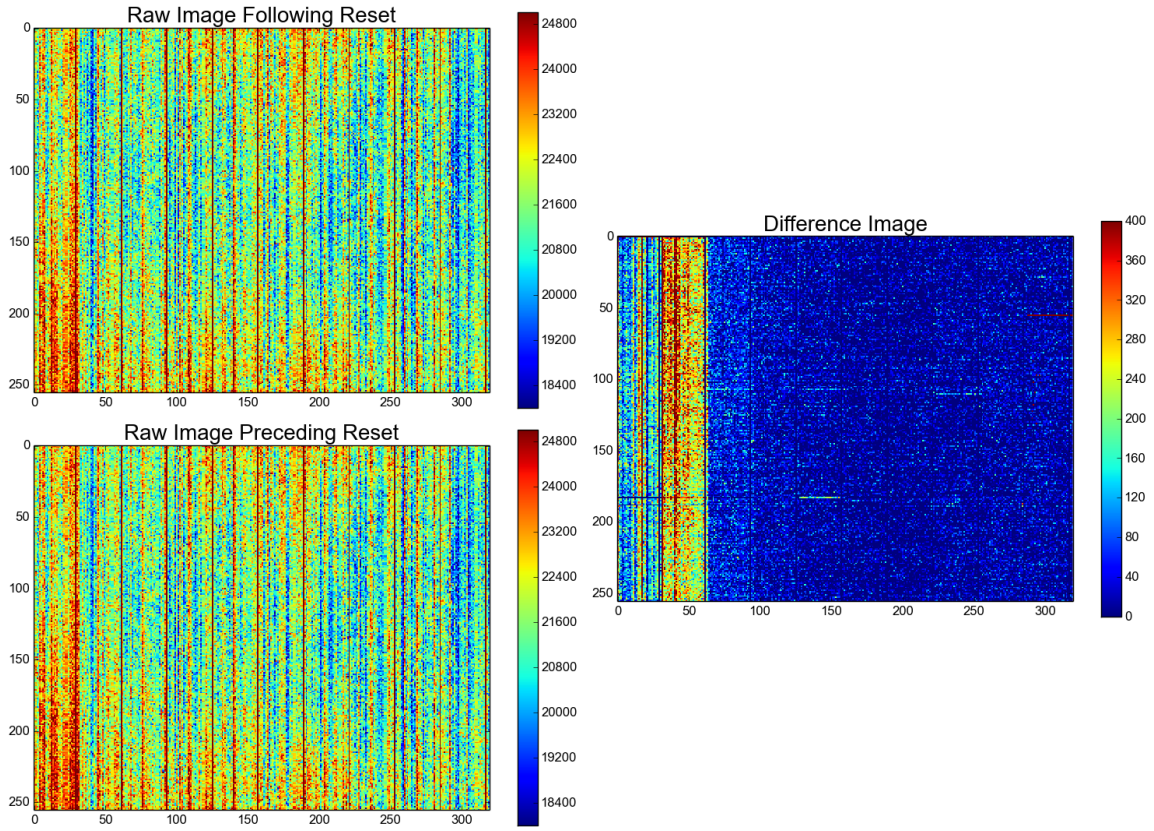

Figure 2.1 On the left are consecutive unilluminated raw frames from SAPHIRA after (top) and before (bottom) the reset in read-reset-read mode. Approximately 2.7 ms has elapsed between the two reads. As is normal for images from infrared arrays, the pedestal noise dominates both images. However, when the before image is subtracted from the after image, not all the noise disappears. An entire row is reset at a time, the detector clocks from left to right, and the column blocks read immediately following the reset have spurious flux. Operating the SAPHIRA with a subarray that excludes these left columns does not solve the problem; the column blocks with spurious flux simply move to the edge of the subarray being read, since they are read immediately following the reset. All images have units of ADUs. We have noticed that this effect is reduced on other SAPHIRA arrays. Because of this post-reset setting problem, we do not typically operate SAPHIRA arrays in read-reset-read mode.

frame for every read, and the temporal sampling is regular. Additionally, read-reset mode does not exhibit the post-reset settling problem (the gradient of spurious flux) of read-reset-read mode. This is because read-reset-read mode has a read immediately following the reset, and the pixels are still settling during this time; on the other hand, in read-reset mode, the pixels have the entire integration time to settle.

2.2.4 Comparison of the Readout Modes

A comparison of the loop update rate and noise sources for each of the readout modes is provided in Table 2.1. In this section, we compare these modes and their associated noise sources.

The SAPHIRA detector can be operated with global resets or line-by-line resets. The user can configure which regions are reset; one can save time by not resetting portions of the array not being read. We typically operate the detector with global resets when sampling up-the-ramp and line-by-line resets in read-reset and read-reset-read mode. However, line-by-line resets can be used in all three modes. ME1000 and ME1001 ROICs support both global and line-by-line resets, whereas ME911 ROICs only support global resets.

Due to the fact that an entire row is reset at once, but then 32 pixels are read in each increment along the row, in read-reset mode, one side of the detector will see less flux. In other words, for pixels on one side of the array, there is a greater interval between the read and reset than for pixels on the opposite side of the array. This effect is worse for a short, fat subarray than for a tall, thin one. For a 320×256 pixel array, the difference in flux from one side to the other is ∼0.3%. For a 320×64 subarray, however, this effect is 1.3%. For most astronomical applications, a standard flat field correction effectively compensates for this effect. This effect is not relevant to sampling up-the-ramp readouts because one is calculating the slope of the flux between reads, and it does not affect read-reset-read images because the read of a given pixel is delayed relative to the reset an equal amount in both frames.

In addition to the post-reset settling effects discussed in Sections 2.2.1 and 2.2.2, we have also observed a smaller amplitude but longer duration thermal settling in the array. When an array begins clocking after sitting idle, the power dissipation in it changes significantly. This causes thermal variations in the array, and it can take hours for these to reach equilibrium. During this time, pixels exhibit slow drifts. We performed a test in which we read out an unilluminated array for several hours in read-reset mode. Every ten minutes, we saved 1000 frames and averaged them to produce an image of the detector's pedestal voltage

Table 2.1 Comparison of noise sources for different SAPHIRA read modes

	Maximum loop update rate	**Noise variance** $\sigma^2_{total} = \sigma^2_{photon} +$	**Comments**
Up the ramp (CDS pairs processed independently)	Every read, with interruption following reset	$2\sigma^2_{RN}$	Dynamic range must be split between the reads in the ramp.
Up the ramp (flux determined by fitting to ramp)	Every ramp	σ^2_{RN}/N_{reads}	Cosmic rays and saturation can be mitigated by excluding those reads from fitting.
Read-reset-read	Every two reads	$2\sigma^2_{RN} + \sigma^2_{spurious}$	The first few column blocks may contain spurious flux.
Read-reset	Every read	$\sigma^2_{RN} + \sigma^2_{settling} + \sigma^2_{kTC}$	Requires reference dark frame.

A comparison of the different readout modes available for the SAPHIRA detector. σ^2_{RN} is the variance in read noise, N_{reads} is the number of reads between resets in a ramp, σ^2_{kTC} is the kTC noise, $\sigma^2_{spurious}$ is the noise associated with post-reset settling in read-reset-read mode, $\sigma^2_{settling}$ is noise due to thermal drifts and is negligible if the data and reference frames are collected near in time to each other or both are collected after at least two hours of detector operation. σ^2_{RN} is assumed to be white. Noise due to radio frequency interference (Section 2.4) is a component of σ^2_{RN}.

with minimal read noise. We then subtracted subsequently collected average frames and computed the standard deviation to see how much the pedestal voltage drifted. The result is shown in Figure 2.2. Again, an approximately two-hour settling timescale was observed. For this reason, it is important to run an "idle sequence" before observations in which no data are saved but the detector clocks as it would during science operations. The SAPHIRA detector should be operated like this for at least two hours prior to observations where temporal stability is required (such as before collecting the reference frames for subsequent read-reset mode observations). It is worth noting that clocking-caused thermal drifts are not unique to SAPHIRA arrays; clocking the same way when idling and observing is key to obtaining good performance from CMOS detectors in general.

This same two-hour timescale for SAPHIRA thermal drifts was also observed in dark current measurements performed by Atkinson et al. (2017). While operating SAPHIRA arrays using up-the-ramp sampling, they noted that it took approximately two hours of continuous clocking before the dark current stabilized. They directly confirmed this thermal time constant during measurements to calibrate the detector temperature offset from the usual temperature monitoring point at the thermal control sensor/heater assembly. This was done using a temperature sensor permanently mounted to the SAPHIRA leadless chip carrier ceramic (this sensor cannot be powered up during science observations because the glow levels are prohibitive). For the temperature offset calibration, the system was allowed to stabilize with the SAPHIRA powered down (except for the temperature sensor) to establish the offset between the two temperature sensors. The SAPHIRA was then powered on and clocked normally. After it stabilized, which took approximately two hours, the on-chip sensor was used to measure the temperature offset.

2.3 Subarray Operation and Calculation of Frame Rate

There are 10 32-channel column blocks across the SAPHIRA, and it can be subarrayed to read integer numbers of column blocks (i.e. the frame size can be adjusted by 32-pixel

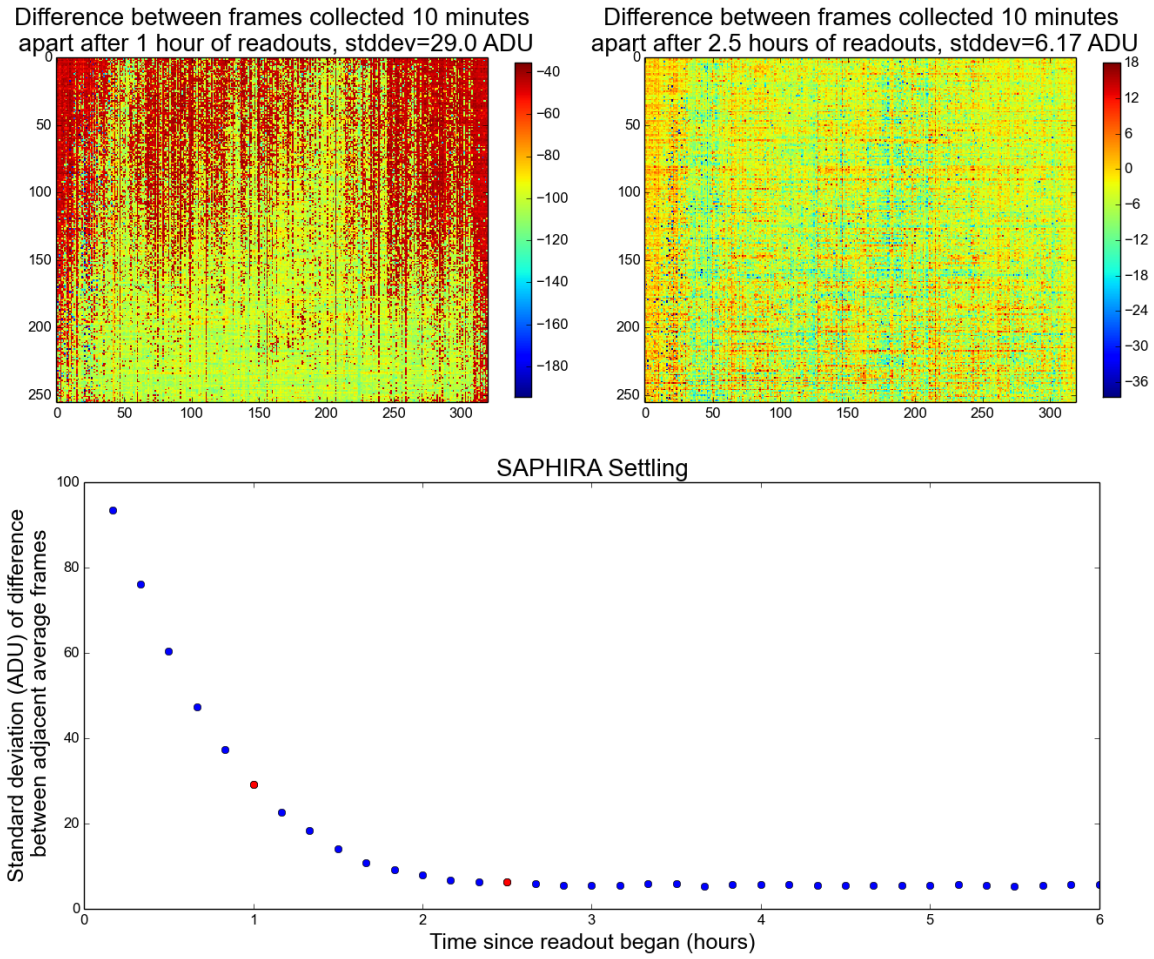

Figure 2.2 While the SAPHIRA continuously streamed images, frames were saved every 10 minutes for several hours. At each interval, 1000 frames were saved and averaged together in order to reduce read noise. Each average frame was then subtracted from the average frames collected 10 minutes earlier and later to see how the pedestal voltage of the detector changed. For approximately the first two hours of image streaming, the pedestal voltage exhibited slow drifts (as shown in the top left figure). However, after about 2-2.5 hours, the detector had largely stabilized (top right). The bottom plot shows how the spatial standard deviation of these difference frames decreases with time. The two example frames shown at the top are identified with red points in the bottom plot. For this reason, it is important to clock the detector for at least two hours before observations that require good stability.

increments in the x direction). On the other hand, the detector will read any number of pixels in the y direction. Multiple subarrays can be supported at once. The 32 outputs on the SAPHIRA read out 32 adjacent pixels in a row at a time. Greatly increased frame rates during subarray readouts are possible because the interleaved nature of the outputs

enables all of them to still be used. To illustrate this, consider the case of a 128×128 pixel subarray. A HAWAII-2RG has 2048 pixels per side and 32 outputs (therefore 64 columns per output), or a HAWAII-4RG has 4096 pixels per side and 64 outputs (so again 64 columns per output). Either HAWAII array would utilize two outputs to read the 128×128 subarray, whereas the SAPHIRA could read it using all 32 outputs. At identical pixel clocking rates, the SAPHIRA could read it 16 times faster.

The SAPHIRA frame rate scales roughly inversely with the number of pixels in the window. This rule is approximate because the array must be reset and there are extra clock cycles at the ends of rows and frames; the full equation for duration of one frame when operating in read-reset mode is given by Equation 2.2.

$$t_{img,rr} = t_{fd} + t_{fc} + n_r(t_{rd}n_{cb} + t_{rst} + t_{prst} + t_{rc} + t_{ra}) \tag{2.2}$$

where $t_{img,rr}$ is the time to collect one image in read-reset mode and the other parameters and their typical values are summarized in Table 2.2. These clock pulses are all necessary for the detector to operate reasonably and cannot be set to 0; the acceptable ranges are specified in the SAPHIRA manual. Read-reset-read mode is similar, but each pixel is read twice, and there is an extra t_{rc} per row.

$$t_{img,rrr} = t_{fd} + t_{fc} + n_r(2t_{rd}n_{cb} + t_{rst} + t_{prst} + 2t_{rc} + t_{ra}) \tag{2.3}$$

For sample up-the-ramp mode, the time to collect a frame (not including the time to reset, since that typically is not done every frame) is

$$t_{img,sutr} = t_{fd} + t_{fc} + n_r(t_{rd}n_{cb} + t_{rc}) \tag{2.4}$$

Naturally, the framerate f is

$$f = t_{img}^{-1} \tag{2.5}$$

The timing values for our current 1 MHz pixel rate are summarized in Table 2.2. These are subject to tuning but can be used as typical values. In line-by-line reset modes, these enable a 1.69 kHz frame rate for a 128×128 pixel subarray or 339 Hz frame rate for 320×256 pixel full frames.

It should be noted that in all readout modes described above, the detector is continuously clocking and reading pixels. This is known as a rolling shutter; different parts of the frame are read at different times. This can be problematic for observations for which the flux is rapidly changing and synchronization is important. For example, in present pyramid wavefront sensors deployed on-sky, the beam is modulated in a circle around the tip of the pyramid in order to increase the linearity of the wavefront sensor's response. This causes each pupil image to be illuminated at a different time. In SCExAO, the beam completes one full modulation per EMCCD image, and the EMCCD has a fast frame transfer which functions as a global shutter, so the detector does not notice the pupils being illuminated at different times. On the other hand, a detector with a rolling shutter might see gradients across the pupil images caused by the modulation, interpret it as an optical aberration, and drive the deformable mirror to a suboptimal shape. The SAPHIRA in the Keck Planet Imager solves this challenge by synchronizing the start of each frame's readout to the modulation so that the part of the frame being read does not include the pupil which is changing in illumination. The time to modulate is slightly greater than the time to read one image, but the dead time between reads is minimized for the reason described in the next paragraph.

The integration times of an image given by Equations 2.2-2.4 depend entirely on the durations of the various clock pulses and number of pixels being read. A user could insert an additional delay in order to increase the detector's integration time. However, unless storage space is limited, this is suboptimal. Instead of inserting a delay to make each exposure longer, the user does better to clock the detector at its maximum rate, increase the avalanche gain to use the entire well depth with each integration (assuming read-reset or read-reset-read mode), and then average images together. This reduces the read noise and

Table 2.2 SAPHIRA clocking timings

Parameter	**Definition**	**Value**	
		Frame size	
		128×128 px	320×256 px
t_{fd}	duration of frame demand clock pulse	310 ns	310 ns
t_{fc}	duration of frame completion clock pulse	410 ns	410 ns
n_r	number of rows being read	128	256
t_{rd}	time that an output spends on each pixel	1 μs	1 μs
n_{cb}	number of 32-pixel column blocks in the image	4	10
t_{rst}	time to reset a row	100 ns	1 μs
t_{prst} (global resets)	post-reset delay	400 ns	400 ns
t_{prst} (line-by-line resets)	post-reset delay	120 ns	120 ns
t_{rc}	duration of row completion clock pulse	210 ns	210 ns
t_{ra}	duration of row advance clock pulse	210 ns	210 ns

A summary of the various times for a full-frame and 128×128 subarray readout of the SAPHIRA. These times can be used in Equations 2.2-2.5 to calculate the expected frame rate. Except for the time to reset the detector, the timings are independent of window size. Except for the post-reset dead time, the timings are independent of reset mode.

therefore improves the signal to noise ratio. This contrasts with a normal (non-avalanche multiplying) detector, wherein reading and resetting the array when very little target flux has accumulated and then coadding the exposures results in the read noises adding in quadrature and therefore a reduced signal-to-noise ratio. (In both normal and avalanche-multiplying detectors, non-destructively reading up the ramp at maximum readout rate until the entire well depth has been used results in optimal signal to noise, assuming that ROIC glow is negligible. For SAPHIRA, one can trade off the ramp length and avalanche gain; the optimal signal-to-noise ratio can be obtained by selecting the avalanche gain that produces the minimum dark current and then using a ramp length that fully utilizes the detector's dynamic range.)

2.4 Radio Frequency Noise and Cryogenic Preamplifiers

Radio frequency interference (RFI) noise is the dominant noise source for SAPHIRA's deployments to Subaru Telescope with the SCExAO instrument, but it is negligible in other environments. In the laboratory, the measured SAPHIRA CDS read noise (9 e^- RMS, Atkinson et al. 2014) at unity avalanche gain and a Generation III Leach Controller (Leach & Low 2000) at a 265 kHz clocking rate is very comparable to the read noise of conventional HAWAII series arrays (Hall et al. 2016a; Fox et al. 2012). The read noise was similar in telescope environments such as the NASA IRTF and Kitt Peak. However when mounted to the SCExAO instrument at the Subaru telescope, the noise is increased by a factor of 4.5, and we have been unable to reduce this through the normal procedures. The SAPHIRA is ground isolated within the cryostat with the analog and digital grounds brought out separately to the controller and then to a "star" ground point. The internal radiation shield and outer vacuum vessel are tied separately to this same star ground to provide concentric Faraday cages. The entire camera system is isolated from the SCExAO bench except through a tie from the star ground to the primary SCExAO ground. SCExAO is characterized by an extremely challenging RFI environment and many of the other

instruments experience higher levels of noise than they did during laboratory testing elsewhere.

RFI shows up as 32-pixel-wide blocks that oscillate in value (Figure 2.3). A power spectrum can reveal some of the sources of RFI. In our current SCExAO deployment, the noise is white except for a 60 Hz spike. In previous deployments, it was dominated by a few discrete frequencies (and therefore could be mostly filtered out from the data). The RFI changes with time, grounding setups, and the arrangement of wires on the outside of the camera. We found that RFI was decreased by increasing the shielding of cables, using twisted-pair cables, eliminating ground loops, and using a "clean" (i.e. with minimal other electronics connected) ground point. RFI behaves as read noise in the noise comparisons of Section 2.2.4.

We are presently testing cryogenic preampliers that were developed at Australia National University. These sit near the detector inside the camera and amplify its electrical signals prior to the wires to the readout electronics. We anticipate that these will greatly reduce the RFI noise. Additionally, our maximum pixel rate until now has been limited to about 1 MHz per output due the ROIC output drivers causing settling issues with our ~ 1 m cable lengths. We expect that the preampliers will enable faster readout rates.

2.5 Avalanche Gain, Charge Gain, and the Excess Noise Factor

In a conventional source-follower HgCdTe array such as the Teledyne HxRG family (Beletic et al. 2008) or the Raytheon Virgo (Starr et al. 2016), there are two gains are of interest: the voltage gain (which has units of μV/ADU) and the charge gain (which has units of e^-/ADU). The charge gain is related to the voltage gain through $Q = CV$ where C is the integrating node capacitance (the sum of the photodiode and ROIC capacitances) and has a typical value of 20 to 40 fF. The voltage gain is a property only of the ROIC. In the previously mentioned infrared detector arrays, the bias voltage is low enough that there

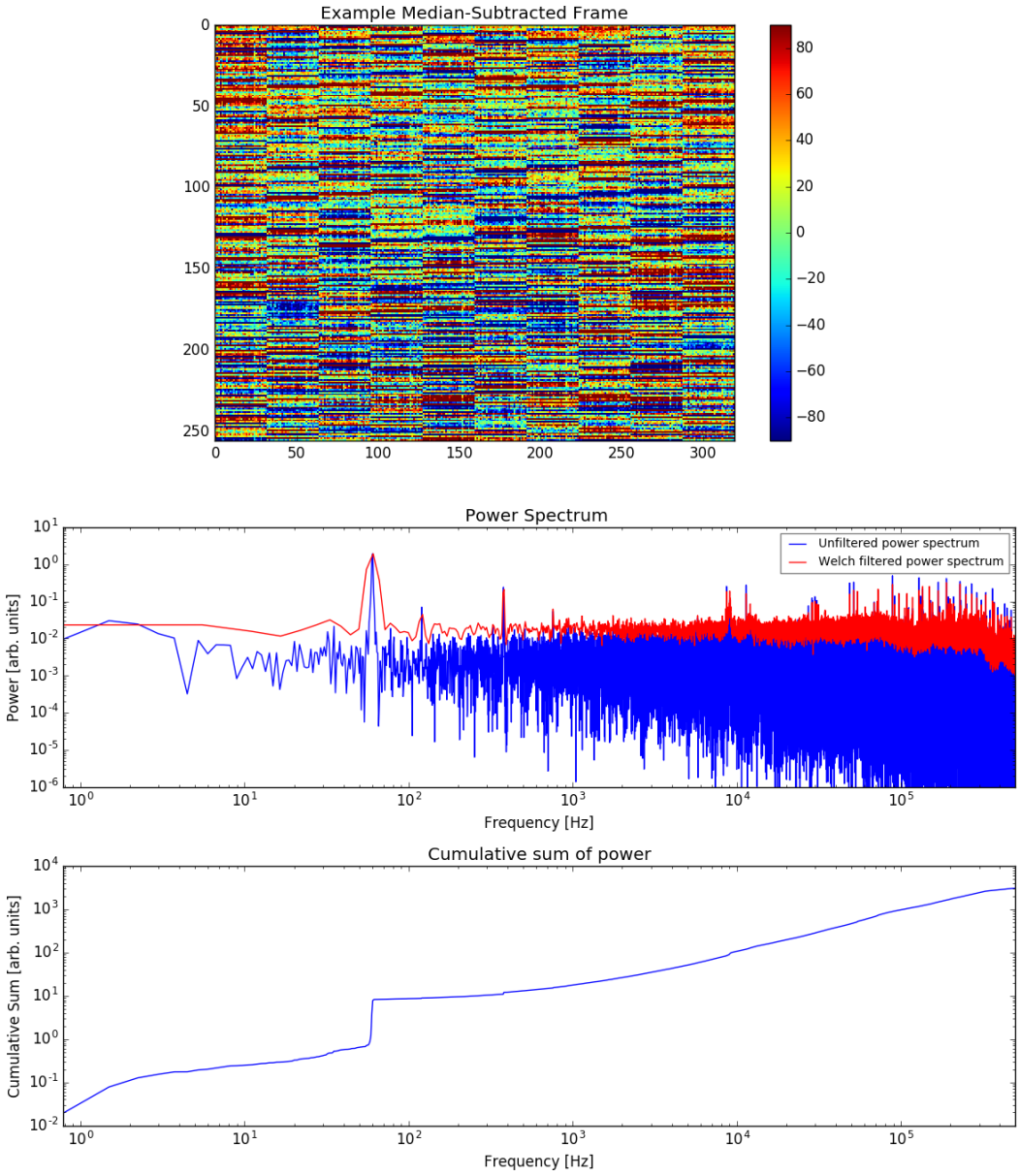

Figure 2.3 Shown at top is a sample single frame (with the pedestal noise subtracted) which exhibits the radio frequency interference of the SCExAO environment. In the middle is a power spectrum calculated from the corresponding full image cube. Apart from a major spike at 60 Hz (likely corresponding to ground contamination from other electronics), the noise is largely white. Plotted over the power spectrum is a Welch-filtered version. The Welch filter (Welch 1967) reduces noise in a power spectrum, but this comes at the expense of spectral resolution. As a result, the lowest frequency bins of the Welch-filtered data are much broader. At the bottom is the cumulative sum of the unfiltered power spectrum.

is minimal change in the photodiode capacitance as the pixel accumulates photons, and this effect can be compensated for with a linearity correction. However, the situation is somewhat more complicated for SAPHIRA. The user adjusts the bias voltage across the detector over a 20 V range in order to set the avalanche gain. At bias voltages too low to produce any avalanche gain ($\lesssim 1$ V), operation is similar to the conventional source-follower arrays. However, as the bias voltage of SAPHIRA increases, avalanche multiplications begin to occur and the diode capacitance, and therefore the charge gain, decreases. Both the avalanche multiplication and the decreasing charge gain should be taken into account when converting between collected photons, electrons, and ADUs for data from SAPHIRA detectors.

During SAPHIRA operation, the input node of each pixel is reset to the selected bias voltage relative to the detector common voltage. After the reset is lifted, photoelectrons discharge the integrating node, and the pixel saturates when the node voltage equals common. The node voltage is read out by a ROIC with a typical gain of 0.8 to 0.9 (for the single source follower design of the ME1000/ME1001) and is further amplified by the controller preamplifier chain before conversion to ADU. The voltage gain of the system (in units of μV/ADU) can be calibrated by varying the reset voltage in known increments and measuring changes in the corresponding digitized signal. The charge gain is normally determined through the signal vs. variance method, although Finger et al. (2005) directly measured a V vs Q relation for an H2RG detector by connecting it to a calibrated large external capacitor and measuring voltage changes in each while pixels were exposed and then reset.

The photodiode capacitance of SAPHIRA increases as the node is discharged, and this causes a flux vs. time plot to depart from linearity as the pixel accumulates flux. Therefore, for photometry applications, it is important to calibrate the linearity of the detector's response for each bias voltage used. Figure 2.4 depicts the photodiode capacitance of a Mark 13 SAPHIRA from 1 V (where the avalanche gain is negligible but the capacitance varies significantly with bias voltage) to 9 V (where the diode is fully depleted so the capacitance

is insensitive to bias, but the avalanche gain is ~ 5). Avalanche gain becomes appreciable at a bias voltage of 2-3 V, and by biasing the detector by up to 20 V, avalanche gains of ~ 600 can be obtained. In all cases, the unit cell source follower still limits dynamic range to a few hundred mV. The avalanche gain is usually measured by varying the bias voltage under constant detector illumination and defining that the flat portion of the response curve (which occurs at 1-2.5 V bias) corresponds to an avalanche gain of 1. From Figure 2.4, it is evident that for avalanche bias voltages $\lesssim 10$ V, the change in capacitance with bias must be included in this avalanche gain calculation.

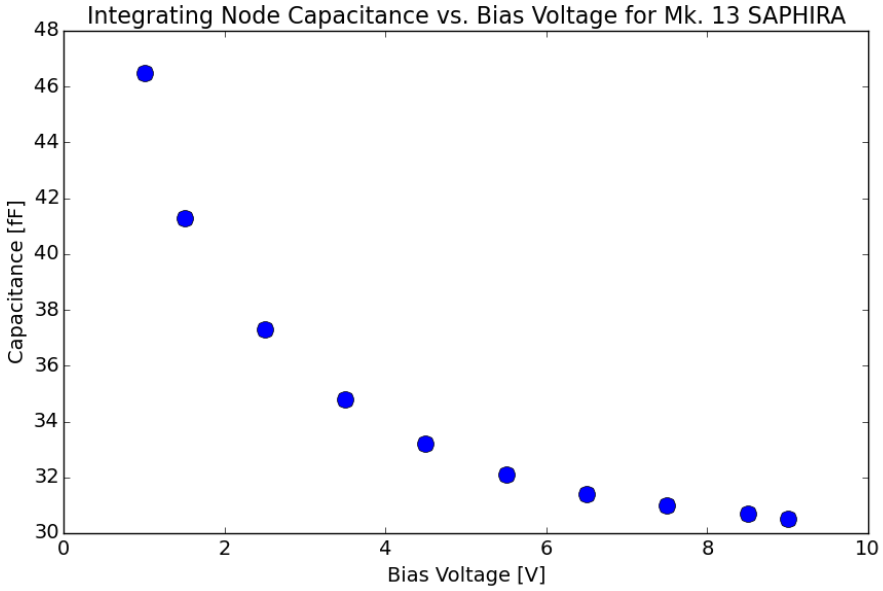

Figure 2.4 The measured integrating node capacitance vs. bias voltage for a Mk. 13 SAPHIRA detector. The data are from Dr. Ian Baker (private communication). 19.9 fF of the integrating node capacitance is due to the silicon readout, and the remainder is the diode. It is important to take into account the increasing capacitance at low bias voltages when measuring avalanche gains.

Read noise and RFI noise are independent of avalanche gain, so one can improve the signal to noise ratio of observations by amplifying the signal of photons with a higher avalanche gain. However, as avalanche gain increases, the dynamic range (in photons) of the detector is reduced because the well depth in electrons remains constant, but more electrons are produced per photon. At sufficiently high bias voltages, tunneling current (a

type of dark current) increases dramatically (Atkinson et al. 2017), can dominate over the read noise, and thereby can degrade the signal to noise ratio of observations (Finger et al. 2016).

The excess noise factor F characterizes noise that occurs during the multiplication process of avalanche photodiodes. F is the ratio of the signal to noise of the photon induced charge to that of the avalanche-multiplied charge (McIntyre 1966); noise-free amplification produces $F = 1$. The advantage of HgCdTe over other semiconductors is that only electrons participate in the avalanche process, and this has the potential for noise-free amplification. Finger et al. (2016) measured an excess noise factor of $F = 1$ at 60 K at all gains and a maximum of $F = 1.3$ at an avalanche gain of 421 at 90 K.

2.6 Conclusions

For most AO-related observations, we operate SAPHIRA in read-reset mode, wherein each row is read before being reset, and the pedestal noise of the detector is removed by subtracting a reference dark frame. This mode enables the maximum usable frame rate and regular time sampling. When a minimum of noise is desired and long periods between detector resets are acceptable, the SAPHIRA can be operated in up-the-ramp mode, wherein there are many reads between resets. The user then fits a line to the flux of each pixel over time, which reduces read noise. If a pixel saturates, one can estimate the correct flux by fitting only to the reads that occurred before the saturation. Read-reset-read mode, wherein a row was read, reset, and read again, and this repeats for the next line, failed to deliver the hoped-for low noise due to a post-reset settling effect that caused spurious flux in the columns read in the first few microseconds after resets. For this reason, we do not commonly use read-reset-read mode.

Because the pixel rate is determined by the readout electronics (and therefore relatively constant) and the outputs are designed to read contiguous 32-pixel blocks, higher frame rates can be achieved by reading $32x \times y$ pixel subarrays, where $1 \leq x \leq 10$, and $1 \leq y \leq 256$. For

example, at a 1 MHz clocking rate in read-reset mode, one can read the full 320×256 pixel frame at a rate of about 339 Hz or a 128×128 subarray at about 1690 Hz. The detector itself is capable of 10 MHz pixel rates, and ESO operates their SAPHIRA arrays at typically 5 MHz rates.

SAPHIRA detectors enable the potential for new observing modes due to their high frame rate, low noise, and infrared sensitivity. We hope that this paper can assist users in utilizing the detectors to their maximum potential.

ACKNOWLEDGMENTS

The authors acknowledge support from NSF award AST 1106391, NASA Roses APRA award NNX 13AC14G, and the JSPS (Grant-in-Aid for Research #23340051 and #26220704). Sean Goebel acknowledges funding support from Subaru Telescope and the Japanese Astrobiology Center.

References

Atkinson, D., Hall, D., Baranec, C., Baker, I., Jacobson, S., & Riddle, R. 2014, in Proc. SPIE, Vol. 9154, High Energy, Optical, and Infrared Detectors for Astronomy VI, 915419

Atkinson, D. E., Hall, D. N. B., Jacobson, S. M., & Baker, I. M. 2017, AJ, 154, 265

Baker, I., Maxey, C., Hipwood, L., & Barnes, K. 2016, in Proceedings of the SPIE, Volume 9915, id. 991505 8 pp. (2016)., Vol. 9915

Baranec, C., Atkinson, D., Riddle, R., Hall, D., Jacobson, S., Law, N. M., & Chun, M. 2015, ApJ, 809, 70

Beletic, J. W., Blank, R., Gulbransen, D., Lee, D., Loose, M., Piquette, E. C., Sprafke, T., Tennant, W. E., Zandian, M., & Zino, J. 2008, in High Energy, Optical, and Infrared Detectors for Astronomy III, Vol. 7021, 70210H

Chapman, R., Beard, S., Mountain, M., Pettie, D., & Pickup, A. 1990, in Proc. SPIE, Vol. 1235, Instrumentation in Astronomy VII, ed. D. L. Crawford, 34–42

Finger, G., Baker, I., Alvarez, D., Dupuy, C., Ives, D., Meyer, M., Mehrgan, L., Stegmeier, J., & Weller, H. J. 2016, in Proc. SPIE, Vol. 9909, Adaptive Optics Systems V, 990912

Finger, G., Baker, I., Alvarez, D., Ives, D., Mehrgan, L., Meyer, M., Stegmeier, J., Thorne, P., & Weller, H. J. 2012, in High Energy, Optical, and Infrared Detectors for Astronomy V. Proceedings of the SPIE, Volume 8453, article id. 84530T, 16 pp. (2012)., Vol. 8453

Finger, G., Beletic, J. W., Dorn, R., Meyer, M., Mehrgan, L., Moorwood, A. F. M., & Stegmeier, J. 2005, Experimental Astronomy, 19, 135

Fox, O. D., Kutyrev, A. S., Rapchun, D. A., Klein, C. R., Butler, N. R., Bloom, J., de Diego, J. A., Farah, A., Gehrels, N. A., Georgiev, L., González, J. J., Lee, W. H., Loose, M., Lotkin, G., Moseley, S. H., Prochaska, J. X., Ramirez-Ruiz, E., Richer, M. G., Robinson, F. D., Román-Zúñiga, C., Samuel, M. V., Sparr, L. M., & Watson, A. M. 2012, in High Energy, Optical, and Infrared Detectors for Astronomy V. Proceedings of the SPIE, Volume 8453, article id. 84531O, 10 pp. (2012)., Vol. 8453

Fried, D. L. 1978, Journal of the Optical Society of America (1917-1983), 68, 1651

Garnett, J. D. & Forrest, W. J. 1993, in Proc. SPIE, Vol. 1946, Infrared Detectors and Instrumentation, ed. A. M. Fowler, 395–404

Goebel, S. B., Guyon, O., Hall, D. N. B., Jovanovic, N., & Atkinson, D. E. 2016, in Proc. SPIE, Vol. 9909, Adaptive Optics Systems V, 990918

Goebel, S. B., Hall, D. N. B., Guyon, O., Warmbier, E., & Jacobson, S. M. 2018, Journal of Astronomical Telescopes, Instruments, and Systems, 4, 1

Greffe, T., Feautrier, P., Gach, J.-L., Stadler, E., Clop, F., Lemarchand, S., Boutolleau, D., & Baker, I. 2016, in Proc. SPIE, Vol. 9907, Optical and Infrared Interferometry and Imaging V, 99072E

Hall, D. N. B., Atkinson, D., Blank, R., Farris, M., Goebel, S. B., Hodapp, K. W., Jacobson, S. M., Loose, M., & Zandian, M. 2016a, in Proceedings of the SPIE, Volume 9915, id. 99150W 10 pp. (2016)., Vol. 9915

Hall, D. N. B., Baker, I., & Finger, G. 2016b, in Proceedings of the SPIE, Volume 9915, id. 99150O 7 pp. (2016)., Vol. 9915

Han, E., Muirhead, P. S., Swift, J. J., Baranec, C., Law, N. M., Riddle, R., Atkinson, D., Mace, G. N., & DeFelippis, D. 2017, AJ, 154, 100

Jensen-Clem, R., Duev, D. A., Riddle, R., Salama, M., Baranec, C., Law, N. M., Kulkarni, S. R., & Ramprakash, A. N. 2018, AJ, 155, 32

Leach, R. W. & Low, F. J. 2000, in Proc. SPIE Vol. 4008, p. 337-343, Optical and IR Telescope Instrumentation and Detectors, Masanori Iye; Alan F. Moorwood; Eds., Vol. 4008, 337–343

Mawet, D., Wizinowich, P., Dekany, R., Chun, M., Hall, D., Cetre, S., Guyon, O., Wallace, J. K., Bowler, B., Liu, M., Ruane, G., Serabyn, E., Bartos, R., Wang, J., Vasisht, G., Fitzgerald, M., Skemer, A., Ireland, M., Fucik, J., Fortney, J., Crossfield, I., Hu, R., & Benneke, B. 2016, in Adaptive Optics Systems V, Vol. 9909, 99090D

McIntyre, R. J. 1966, IEEE Transactions on Electron Devices, 13, 164

Mehrgan, L. H., Finger, G., Eisenhauer, F., & Panduro, J. 2016, in Proceedings of the SPIE, Volume 9907, id. 99072F 11 pp. (2016)., Vol. 9907

Starr, B., Mears, L., Fulk, C., Getty, J., Beuville, E., Boe, R., Tracy, C., Corrales, E., Kilcoyne, S., Vampola, J., Drab, J., Peralta, R., & Doyle, C. 2016, in Proc. SPIE, Vol. 9915, High Energy, Optical, and Infrared Detectors for Astronomy VII, 99152X

Welch, P. D. 1967, IEEE Trans. Audio and Electroacoust., Volume AU-15, p. 70-73, 15, 70

Wizinowich, P., Chun, M., Mawet, D., Agapito, G., Dekany, R., Esposito, S., Fusco, T., Guyon, O., Hall, D., Plantet, C., & Rigaut, F. 2016, in Proc. SPIE, Vol. 9909, Adaptive Optics Systems V, 990915

Chapter 3

Commissioning of cryogenic preamplifiers for SAPHIRA detectors

Note: This chapter originally was submitted to the "High Energy, Optical, and Infrared Detectors for Astronomy VIII" 2018 SPIE proceedings with co-authors Donald N.B. Hall, Shane M. Jacobson, Annino Vaccarella, Rob Sharp, Michael Ellis, and Izabella Pastrana. It will be published as Goebel et al. (2018).

Abstract

SAPHIRA detectors, which are HgCdTe linear avalanche photodiode arrays manufactured by Leonardo, enable high frame rate, high sensitivity, low noise, and low dark current imaging at near-infrared wavelengths. During all University of Hawaii Institute for Astronomy lab testing and observatory deployments of SAPHIRA detectors, there was approximately one meter of cables between the arrays and the readout controllers. The output drivers of the detectors struggled to stably send signals over this length to the readout controllers. As a result, voltage oscillations caused excess noise that prevented us from clocking much faster than 1 MHz. Additionally, during some deployments, such as at the SCExAO instrument at Subaru Telescope, radio-frequency interference from the telescope environment produced noise many times greater than what we experienced in the lab. In order to address these problems, collaborators at the Australia National University developed a cryogenic preamplifier system that holds the detector and buffers the signals

from its outputs. During lab testing at 1 MHz clocking speeds, the preamplifiers reduced the read noise by 45% relative to data collected using the previous JK Henriksen detector mount. Additionally, the preamplifiers enabled us to increase the clocking frequency to 2 MHz, effectively doubling the frame rate to 760 Hz for a full (320×256 pixel) frame or 3.3 kHz for a 128×128 pixel subarray. Finally, the preamplifiers reduced the noise observed in the SCExAO environment by 65% (to essentially the same value observed in the lab) and eliminated the 32-pixel raised bars characteristic of radio-frequency interference that we previous observed there.

3.1 Introduction

The SAPHIRA detector is a 320×256@24 μm pixel mercury cadmium telluride (HgCdTe) array produced by Leonardo (formerly Selex) with 0.8−2.5 μm sensitivity(Baker et al. 2016). SAPHIRA is a linear avalanche photodiode (L-APD), meaning that it has a multiplication region over which the avalanche gain multiplies the photon signal. At ∼2 V bias, SAPHIRA operates as a traditional HgCdTe array with no avalanche multiplication. The bias voltage can be increased to ∼20 V, where the photon signal is multiplied by a factor of several hundred (Atkinson et al. 2016). The read noise is unaffected by the avalanche gain, so at moderate to high bias voltages, the gain-corrected read noise is sub-electron (Finger et al. 2016). Equivalently, the signal of an individual photon exceeds the read noise; this is called photon counting (Atkinson et al. 2018). Unlike Geiger-mode APDs (Renker 2006), SAPHIRA does not need to be reset after each photon arrival. SAPHIRA has 32 outputs and is optimized for high frame rates. The outputs are interleaved (the 32 outputs read 32 adjacent columns), so all are still used when the detector is operated in subwindow mode. Therefore, the frame rate increases approximately as the inverse of the number of pixels read (Goebel et al. 2018).

The low noise, high sensitivity, and high frame rate makes SAPHIRA well-suited for wavefront sensing for adaptive optics (AO). Presently most wavefront sensing is done

at optical wavelengths with CCDs, and the science instruments behind AO systems most commonly observe at near-infrared (NIR) wavelengths. Wavefront sensing at NIR wavelengths is of particular interest because it would reduce chromatic aberrations caused by wavelength differences between the science instrument and wavefront sensor, and it would enable observations of targets with low optical emission but high NIR emission such as M dwarfs (Wizinowich et al. 2016). SAPHIRA also features a very low dark current (Atkinson et al. (2017) measured an upper limit of the dark current at 62.5 K of 0.0014 e^{-} s^{-1} pix^{-1}), which offers promise for low-background imaging, but this application is presently limited by the relatively small format of the detector. However, a 1K×1K@15 μm pixel SAPHIRA is currently in development (Hall et al. 2016).

Much of this paper focuses on the SAPHIRA deployment to the Subaru Coronagraphic Extreme Adaptive Optics (SCExAO) instrument at Subaru Telescope. SCExAO, as the name implies, provides extreme adaptive optics corrections using a 2000-element deformable mirror (typically operated at 2 kHz) and is optimized for coronagraphic observations of extrasolar planets and debris disks (Jovanovic et al. 2015). SCExAO constantly undergoes changes and serves as a testbed for new technologies, such as SAPHIRA, the MKIDs energy-resolving superconducting detector (Szypryt et al. 2017), phase-induced amplitude apodization (PIAA) coronagraphs (Martinache et al. 2012), and a photonic spectrograph fed by a single-mode fiber (Jovanovic et al. 2017). At SCExAO, SAPHIRA has been used for speckle lifetime measurements (Goebel et al. 2016) and as a demonstrator for near-infrared pyramid wavefront sensing.

SAPHIRA detectors have been deployed to a number of other facilities. In part because of the capabilities SAPHIRA demonstrated at SCExAO, it is in the process of being deployed in the Keck Planet Imager (Mawet et al. 2016), where it will be used behind pyramid optics for wavefront sensing. SAPHIRA arrays have also been used for lucky imaging at the NASA Infrared Telescope Facility (Atkinson et al. 2014) and tip/tilt tracking at the Robo-AO instrument at Kitt Peak (Salama et al. 2016; Baranec et al. 2015; Jensen-Clem et al. 2018), where it produced its first science publication (Han et al. 2017). Several

SAPHIRA detectors are deployed at the Very Large Telescope's GRAVITY instrument for wavefront sensing and fringe tracking (Finger et al. 2016). Additionally, First Light Imaging has marketed a commercial camera with readout electronics based around the SAPHIRA detector called the C-RED One (Greffe et al. 2016).

3.2 SAPHIRA without Preamplifiers

In all SAPHIRA deployments except at the GRAVITY instrument, the signals from the detector's read out integrated circuit (ROIC) were not amplified prior to being digitized by the readout electronics. Institute for Astronomy SAPHIRA arrays were operated using Gen III Leach controllers (Leach & Low 2000) clocking at 265 kHz or Pizza Box controllers developed there which clocked at 1 MHz. For these setups, there was about 1 m of cabling between the camera and the electronics. A 1 MHz clocking frequency enabled a full-frame (320×256 pixel) readout rate of 380 frames per second or a 128×128 pixel subarray read rate of 1.68 kHz (Goebel et al. 2018).

The detector itself is designed for up to 10 MHz clocking, but we encountered problems when we attempted to clock detector significantly faster than 1 MHz. If we attempted to do this, "ringing in the cables" became a problem.[1] Essentially, the cables were high impedance and reflections occurred at the ends, causing the voltage seen by the readout electronics to oscillate. This effect manifested itself in images as high noise, and the noise became catastrophically limiting if we tried to clock the detector much faster than 1 MHz.

Second, we encountered extremely high noise when we deployed the SAPHIRA camera to observatories. This was the worst at the SCExAO instrument at Subaru Telescope, where we encountered read noises in excess of 300 e^-. For comparison, with the same setup, we measured to 9 e^- in the lab in Hilo (Atkinson et al. 2014). At SCExAO and other observatories, rapidly changing voltage offsets were introduced during the digitization

[1]The C-RED One is able to clock faster than 1 MHz without a preamplifier because the cables between the detector and readout electronics are shorter and lower impedance than ours.

of pixel values. Because 32 adjacent pixels are read at the same time, this appears as horizontal 32-pixel bars in images and is illustrated in the top panel of Figure 3.1.

The SAPHIRA camera is electrically isolated from the SCExAO bench. The camera is supposed to act as a Faraday shield for the detector, though it is imperfect because the detector is located close to the entrance window and thus not surrounded by metal on all sides. Early SCExAO deployments used a Gen III Leach controller, which had seven cards plugged into a black plane board and therefore was susceptible to excess noise caused by imperfect grounding. We were able to reduce but not eliminate the noise by eliminating ground loops, covering the open side of the Leach controller in foil, and wrapping foil around the unshielded cables from it to the camera. However, even after this, the noise was still a factor of $\sim$ 10 higher than lab values. Much of the noise power appeared at discrete frequencies, so we were able to partially mitigate it after observations by digitally Fourier filtering the images.

We further reduced the noise when we switched to a Pizza Box controller (which has a single ground plane), began using cables with a grounded shield around them, and grounded the camera and readout to Subaru's "clean" instrument-only ground instead of the standard building ground. However, the noise was at best still a factor of $\sim$ 3 higher than that of the lab. Figure 3.2 shows the typical setup of the SAPHIRA system on the SCExAO instrument. By taking into account the amount of time the readout spent on each pixel, ends of rows, and ends of frames, we stitched together frames and produced power spectra of the noise with frequency coverage from 1 Hz to 500 kHz (Figure 3.1 middle and bottom panels). After performing the grounding and shielding steps described above, the noise was relatively white except for a spike at 60 Hz.

SAPHIRA is not the only instrument at Subaru to experience excess noise; the CHARIS integral field spectrograph and HiCIAO imager also had this problem, and others likely did as well. Subaru has a large number of instruments in relatively tight proximity to each other, there are high magnetic fields in the facility, and the ground beneath the building is

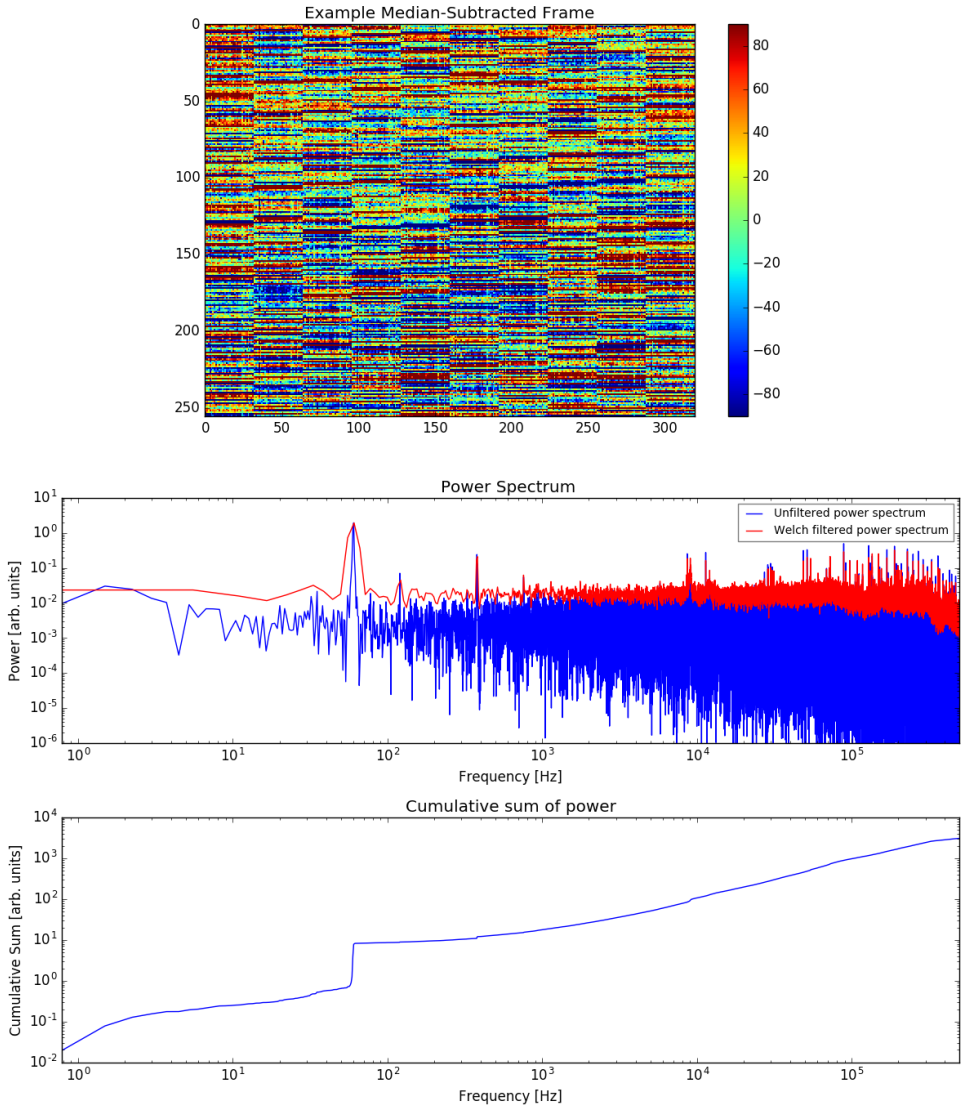

Figure 3.1 The top panel shows an unilluminated SAPHIRA image which exhibits radio frequency noise. This was collected at SCExAO using a Pizza Box controller. Many images were averaged together to produce a map of the detector's fixed-pattern noise (pedestal voltage) and then subtracted from this frame in order to remove the structure that otherwise would dominate. The second panel shows the power spectrum of the noise produced by carefully taking into account how the readout temporally sampled the array in order to string together many images and sample over large temporal baselines. The red line is the power spectrum after Welch filtering (Welch 1967); this reduces noise but also decreases the temporal resolution. Finally, the bottom panel shows the cumulative sum of the power spectrum; it is dominated by a single spike at 60 Hz. This figure reproduced from Goebel et al. (2018).

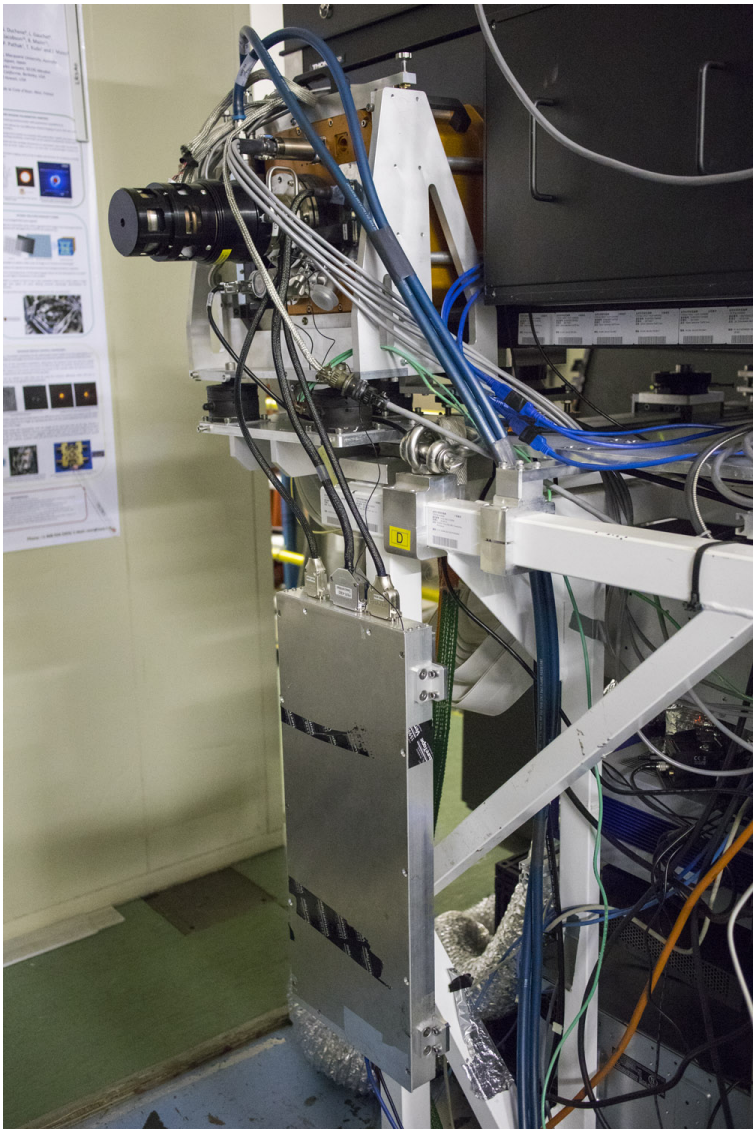

Figure 3.2 Shown here is the SAPHIRA camera (orange) at the SCExAO instrument. The Pizza Box readout electronics is the rectangular box below it. The camera and Pizza Box are electrically isolated from the frame.

volcanic and inherently a poor conductor. Additionally, when we tested SAPHIRA at Keck Observatory, the noise was double that of Hilo.

3.3 The ANU Preamplifier

In order to reduce the radio frequency noise that appeared during telescope deployments and avoid the ringing in the cables that limited our maximum clocking frequency, we concluded that we needed to amplify the detector's signal prior to the cables to the readout electronics. To achieve this, we collaborated with Australia National University (ANU), which developed a cryogenic preamplifier for SAPHIRA. We tested it at IFA Hilo at cryogenic temperatures and then deployed it to SCExAO at Subaru Telescope. The ANU preamplifier replaced the JK Henriksen detector mount that we previously used.

The ANU preamplifier consists of two boards connected by a flex cable: the APD carrier, which holds the detector and replaces the JK Henriksen mount, and a second board which actually carries the preamplifiers. The APD carrier board is shown in Figure 3.3 and measures approximately 63×71 mm. The preamplifier board measures approximately 64×70 mm. These two boards are collectively referred to as the ANU preamplifier throughout this paper. The preamplier requires a $3 - 5.5$ V power supply and draws ∼0.14 A at 4.00 V. The boards use Hirose connectors, but in future revisions, these may be replaced with AirBorn connectors for improved connective reliability. We have tested it successfully at temperatures as low as 58 K, but we have not made a concerted effort to find its minimum operating temperature.

The ANU preamplifier passes through the clocking pulses to the detector without affecting them. It provides filtering to the bias supplies on the underside of the carrier board as close as possible to the detector (except for Bias_ILIMIT, IMPIX1_OR, and IMPIX2_OR, which are disconnected). The filtering is placed on the underside of the board to mitigate the risk of glow from warm components being seen by the detector. The preamplifier buffers the output signals from the ROIC to clean them and enable longer cable runs to the readout

circuitry. Previously, the output amplifiers of the ROIC struggled to drive signals over our meter-long cables, and the preamplifier eases that. The ANU preamplifier was designed to have a gain of unity so that users would not need to adjust the dynamic range of the readout's analog-to-digital converters.

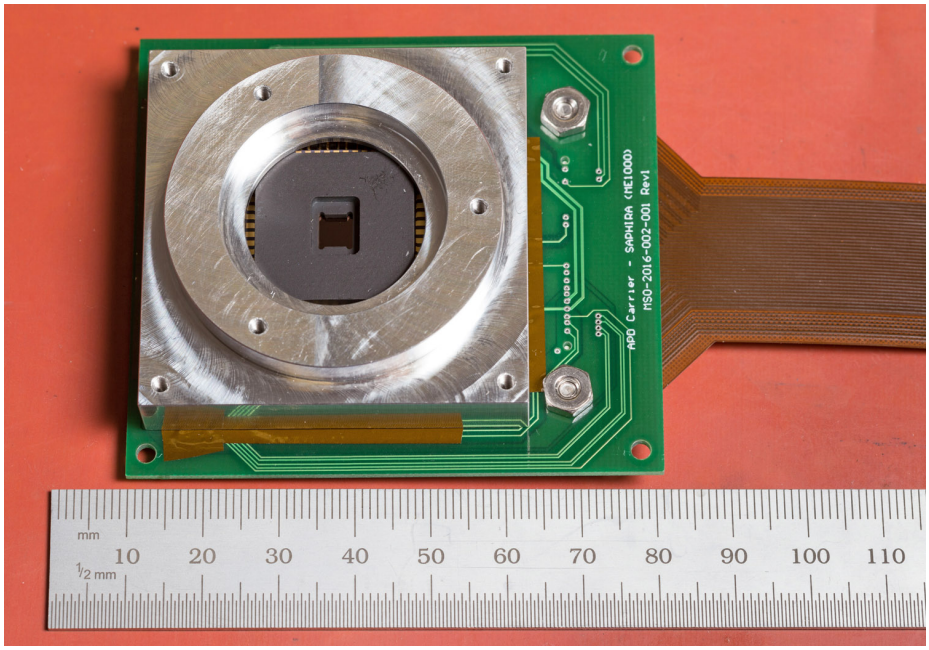

Figure 3.3 Pictured here is the APD carrier board. A ruler provides scale. A shaped mask covers the edges of the detector in order to provide image structure during illuminated tests and reduce ROIC glow during dark tests. The flex cable exiting the right side of the image connects to the similarly-sized board that holds the actual preamplifying circuitry.

3.4 Lab Testing

After performing preliminary functionality tests with the cryogenic preamplifier in the lab at IFA Hilo, we looked at its impact on read noise. We collected frames using a Rev. 4 Pizza Box controller in low gain mode and clocking at 1 MHz, and an unilluminated Mk. 15 SAPHIRA array on a ME1001 ROIC at 60 K. The detector had a 1.5 V bias (i.e. no avalanche gain) and was operated in sample up the ramp readout mode. We subtracted adjacent frames (i.e. $F_{N+1} - F_N, F_{N+3} - F_{N+2}, \cdots$, where F_N is the Nth frame in the

ramp) in order to remove the pedestal noise. We then dropped the first 70 frames after each detector reset and computed the standard deviation of the remaining correlated double sample (CDS) pairs with no masking of bad pixels. We observed 4.593 analog-to-digital units (ADU) of noise when using the ANU preamplifier and 7.459 ADU when using the traditional JK Henriksen detector mount. To convert these numbers to physical units and compensate for any gain in the preamplifier, we measured the volt gain in order to find the conversion from ADU to volts. We varied the pixel reset voltage (PRV) in 10 mV increments and measured the average ADU (DC offset) of the unilluminated detector. The result is plotted in Figure 3.4. We measured a gain of 23.73 μV/ADU using the JK Henriksen mount and 21.36 μV/ADU using the preamplifier. Therefore the cryogenic preamplifier attenuated the signal from the detector by a factor of $21.36/23.73 = 0.900$ at a temperature of 60 K. Putting all this together, the noise was 177 μV with the JK Henriksen mount and 98.1 μV with the preamplifier. In other words, in this experiment the preamplifier reduced the read noise by 45%. We did not have a charge gain measurement for this detector, and it has a significantly different architecture than detectors that we have measured charge gains for, so we cannot accurately convert this read noise to units of electrons.

Second, we looked at whether the cryogenic preamplifiers enabled higher clocking frequencies and thereby faster frame rates. The Pizza Box was originally intended for 2 MHz clocking speeds, but we encountered very high levels of noise at this speed, so in all SAPHIRA Pizza Box deployments, the detector was clocked at 1 MHz. At 2 MHz sampling frequencies, the voltage from each pixel had inadequate time to settle, and this manifested itself in images as high read noise. Figure 3.5 shows an oscilloscope trace of the voltage from a pixel with and without the preamplifiers. The preamplifiers cause a high voltage oscillation when the readout initially clocks onto a pixel, but this decays in $\sim$300 ns, and the voltage of the pixel is more stable than it was at that same point in time without the preamplifier. This is why the read noise was reduced in the 1 MHz clocking speeds described above. We successfully clocked the detector at 2 MHz with the preamplifier; however, we encountered computer input/output limitations due to the increased data rate and therefore

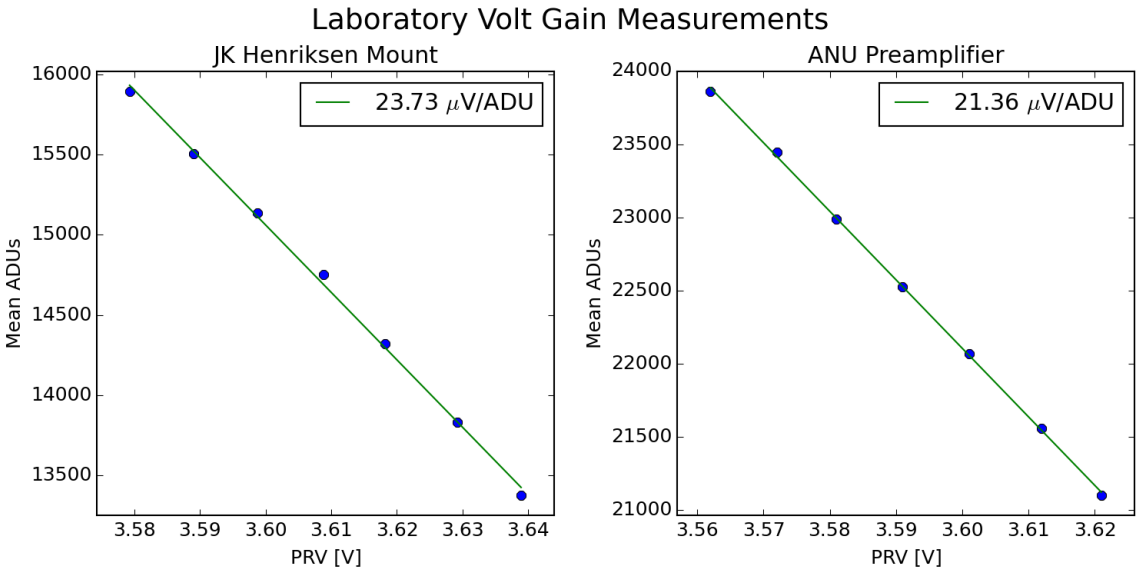

Figure 3.4 Shown here are our volt gain measurements for the lab characterization of the ANU preamplifier. We varied the pixel reset voltage (PRV) in 10 mV increments and measured the average ADU value of the unilluminated array. Several thousand frames were averaged for each data point.

could not reliably make a noise measurement. Once the necessary fixes are implemented, we anticipate operation at 2 MHz during future AO deployments.

3.5 SCExAO Deployment

Next, we modified our GL Scientific Sterling-cooled cryostat to accommodate the cryogenic preamplifier and deployed the camera system to SCExAO. Because of the high noise we experienced in that environment, we were particularly interested in the preamplifier's performance there. This system used a Mk. 14 SAPHIRA detector on a ME1000 ROIC. Following the procedure described in Section 3.4, in order to convert from ADUs to volts, we performed a volt gain measurement before and after the installation of the preamplifier; this is shown in Figure 3.6. In this case, the ratio of the volt gain with the JK Henriksen mount to the gain with the preamplifier is 0.98. This contrasts with the 0.90 ratio observed

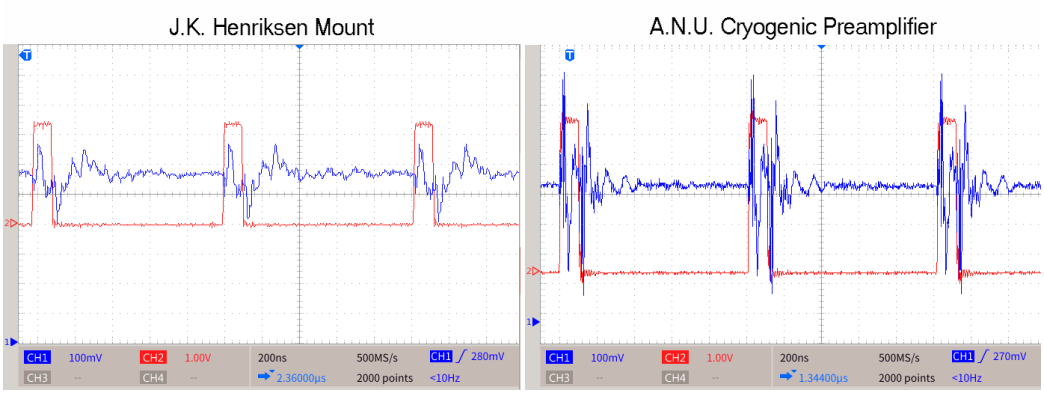

Figure 3.5 Plotted above are the pixel clock pulse (red) and the pixel output voltage (blue) with and without the cryogenic preamplifier. In both setups, the clocking frequency is 1 MHz (i.e. the interval between clock pulses is 1 μs). The voltage of a pixel oscillates after the readout clocks onto it, and we insert a delay between clocking onto a pixel and sampling it in order to permit its voltage to settle. A faster settling enables a higher clocking speed at a given noise level. The preamplified detector has a higher initial amplitude of oscillations, but these oscillations decay faster, and the voltage is more stable after $\sim$300 ns. Additionally, in the near future we will add additional filtering in order to reduce the voltage oscillation further. The vertical and horizontal scalings of both plots are the same; the clocking voltage has a smaller amplitude in the left plot because it was sampled at a different location on the Pizza Box.

in our laboratory testing. This suggests that the preamplifier has a temperature dependent gain, since the laboratory testing was at 65 K and the SCExAO testing was at 85 K.

To measure the noise, we operated the detector in read-reset mode at 1 MHz clocking speed and collected large cubes of frames in order to allow the detector to settle. For a discussion of various readout modes and the noise sources of each, see Goebel et al. (2018). Once the detector was stable, we selected 500 subsequent frames and then subtracted the time average of these from each frame in order to remove its pedestal voltage. We then computed the standard deviation of each frame and took the median of these standard deviations. Using this method, we saw a noise of 126 ADU with the JK Henriksen mount and 45 ADU with the preamplifiers. Taking into account the volt gains derived in Figure 3.6, this is 657 μV and 230 μV, respectively, corresponding to a 65% reduction in noise! These numbers are not directly comparable to those reported in Section 3.4 because in that case the detector was operated in sample up the ramp readout mode. However, data collected in

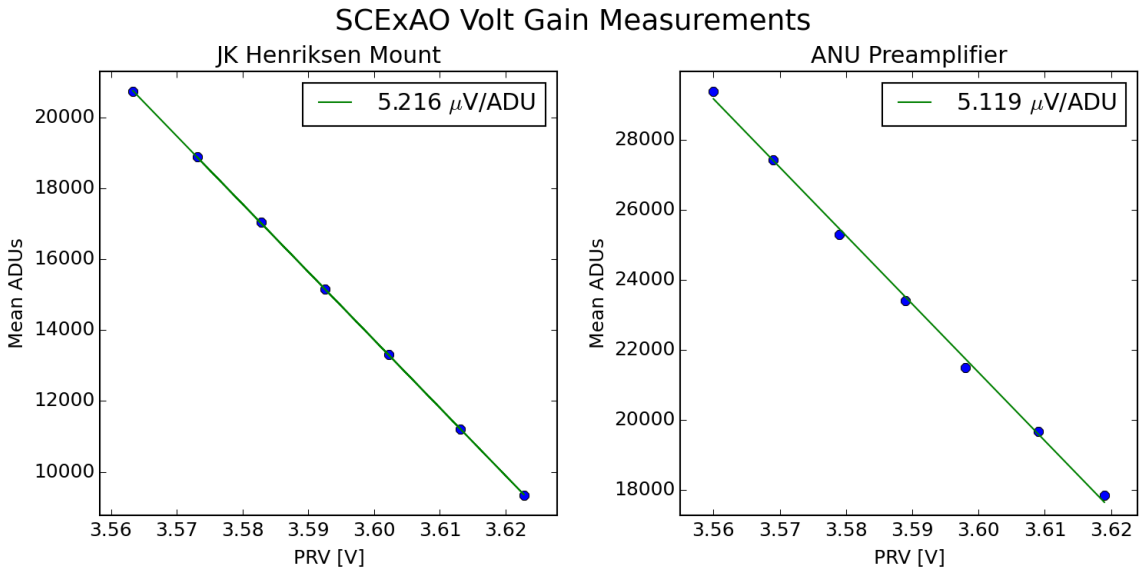

Figure 3.6 Shown here are our volt gain measurements for the SCExAO deployment of the ANU preamplifier. We varied the pixel reset voltage (PRV) in 10 mV increments and measured the average ADU value of the unilluminated array. Several hundred frames were averaged for each data point. The gains are a factor of ∼4 different from that of Figure 3.4 because the Pizza Box operated in low gain mode in the lab and high gain mode for this test.

the lab with the same readout mode, Pizza Box settings, and reduction method as reported in this section had 211 μV standard deviation of noise. The difference between the two can be accounted for by the reduction in kTC noise due to the lower operating temperature in Hilo. Pastrana et al. (in preparation) measured an avalanche-corrected charge gain for this laboratory Mk. 13 SAPHIRA at the same (2.8 V) bias voltage of 1.2 e^-/ADU. If we assume that the Mk. 14 detector deployed to SCExAO has the same charge gain (a reasonable but not exact assumption), this corresponds to a noise standard deviation of 55 e^-. However, because the detector was operated in read-reset mode instead of correlated double sample mode, this noise number includes both kTC noise (which is most of it) and also the read noise (a comparatively small fraction). As stated before, the avalanche gain multiplies the photon signal but has no impact on the read and kTC noise, so an avalanche gain above 55 would enable the equivalent of sub-electron noise.

The noise in the images at SCExAO with the preamplifiers appeared white and did not exhibit the 32-pixel-wide raised bars characteristic of the previous radio frequency interference (Figure 3.1). Additionally, we tested various grounding setups at SCExAO and wrapped the flex cable from the camera to the Pizza Box in foil (it was previously not shielded), and there was very little change in this noise. This contrasts sharply with the previous situation at SCExAO, where every minor change in grounding made a large impact on the noise. A comparison of image quality before and after installation of the preamplifier is shown in Figure 3.7.

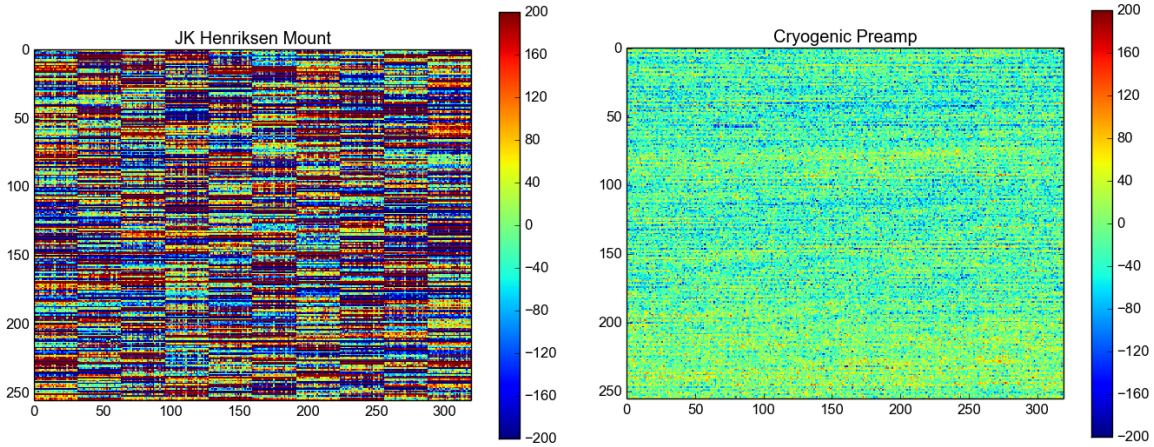

Figure 3.7 Illustrated are single images collected at SCExAO using SAPHIRA in read-reset mode with the JK Henriksen detector mount (left) and the ANU preamplifier (right). The images have identical processing and scaling in units of ADUs. In both cases, a mean frame was subtracted in order to remove the pedestal voltage pattern from the detector.

3.6 Conclusions

We tested cryogenic preamplifiers that were developed at ANU for SAPHIRA detectors. In lab testing, they reduced read noise at 1 MHz clocking by 45% and enabled us to increase the clocking frequency of SAPHIRA from 1 to 2 MHz. A 2 MHz frequency enables a full frame (320×256 pixels) to be read at a rate of approximately 760 Hz or a 128×128 pixel subarray to be read at 3.3 kHz. When deployed to SCExAO, where we struggled for years to minimize

excess noise caused by radio-frequency interference, the cryogenic preamplifiers reduced noise by 65%, thereby enabling essentially the same noise performance we measured in the lab. This improvement greatly enhances the sensitivity of SAPHIRA arrays and enables higher frame rate and/or higher signal-to-noise observations during future deployments.

ACKNOWLEDGMENTS

The authors acknowledge support from NSF award AST 1106391, NASA Roses APRA award NNX 13AC14G, and the JSPS (Grant-in-Aid for Research #23340051 and #26220704). Sean Goebel acknowledges funding support from Subaru Telescope and the Japanese Astrobiology Center.

References

Atkinson, D., Hall, D., Baranec, C., Baker, I., Jacobson, S., & Riddle, R. 2014, in Proceedings of the SPIE, Volume 9154, id. 915419 12 pp. (2014)., Vol. 9154, 915419

Atkinson, D., Hall, D., Jacobson, S., & Baker, I. M. 2018, AJ, 155, 220

Atkinson, D. E., Hall, D. N. B., Baker, I. M., Goebel, S. B., Jacobson, S. M., Lockhart, C., & Warmbier, E. A. 2016, in High Energy, Optical, and Infrared Detectors for Astronomy VII, Vol. 9915, 99150N

Atkinson, D. E., Hall, D. N. B., Jacobson, S. M., & Baker, I. M. 2017, AJ, 154, 265

Baker, I., Maxey, C., Hipwood, L., & Barnes, K. 2016, in Proceedings of the SPIE, Volume 9915, id. 991505 8 pp. (2016)., Vol. 9915, 991505

Baranec, C., Atkinson, D., Riddle, R., Hall, D., Jacobson, S., Law, N. M., & Chun, M. 2015, ApJ, 809, 70

Finger, G., Baker, I., Alvarez, D., Dupuy, C., Ives, D., Meyer, M., Mehrgan, L., Stegmeier, J., & Weller, H. J. 2016, in Proc. SPIE, Vol. 9909, Adaptive Optics Systems V, 990912

Goebel, S. B., Guyon, O., Hall, D. N. B., Jovanovic, N., & Atkinson, D. E. 2016, in Proc. SPIE, Vol. 9909, Adaptive Optics Systems V, 990918

Goebel, S. B., Hall, D. N. B., Guyon, O., Warmbier, E., & Jacobson, S. M. 2018, Journal of Astronomical Telescopes, Instruments, and Systems, 4, 1

Goebel, S. B., Hall, D. N. B., Jacobson, S. M., Vaccarella, A., Sharp, R., & Ellis, M. 2018, in Proc. SPIE 10709-27, High Energy, Optical, and Infrared Detectors for Astronomy VIII (to be published)

Greffe, T., Feautrier, P., Gach, J.-L., Stadler, E., Clop, F., Lemarchand, S., Boutolleau, D., & Baker, I. 2016, in Proceedings of the SPIE, Volume 9907, id. 99072E 9 pp. (2016)., Vol. 9907, 99072E

Hall, D. N. B., Baker, I., & Finger, G. 2016, in Proceedings of the SPIE, Volume 9915, id. 99150O 7 pp. (2016)., Vol. 9915, 99150O

Han, E., Muirhead, P. S., Swift, J. J., Baranec, C., Law, N. M., Riddle, R., Atkinson, D., Mace, G. N., & DeFelippis, D. 2017, AJ, 154, 100

Jensen-Clem, R., Duev, D. A., Riddle, R., Salama, M., Baranec, C., Law, N. M., Kulkarni, S. R., & Ramprakash, A. N. 2018, AJ, 155, 32

Jovanovic, N., Martinache, F., Guyon, O., Clergeon, C., Singh, G., Kudo, T., Garrel, V., Newman, K., Doughty, D., Lozi, J., Males, J., Minowa, Y., Hayano, Y., Takato, N., Morino, J., Kuhn, J., Serabyn, E., Norris, B., Tuthill, P., Schworer, G., Stewart, P., Close, L., Huby, E., Perrin, G., Lacour, S., Gauchet, L., Vievard, S., Murakami, N., Oshiyama, F., Baba, N., Matsuo, T., Nishikawa, J., Tamura, M., Lai, O., Marchis, F., Duchene, G., Kotani, T., & Woillez, J. 2015, Publications of the Astronomical Society of the Pacific, 127, 890

Jovanovic, N., Schwab, C., Guyon, O., Lozi, J., Cvetojevic, N., Martinache, F., Leon-Saval, S., Norris, B., Gross, S., Doughty, D., Currie, T., & Takato, N. 2017, A&A, 604, A122

Leach, R. W. & Low, F. J. 2000, in Proc. SPIE Vol. 4008, p. 337-343, Optical and IR Telescope Instrumentation and Detectors, Masanori Iye; Alan F. Moorwood; Eds., Vol. 4008, 337–343

Martinache, F., Guyon, O., Clergeon, C., & Blain, C. 2012, Publications of the Astronomical Society of the Pacific, 124, 1288

Mawet, D., Wizinowich, P., Dekany, R., Chun, M., Hall, D., Cetre, S., Guyon, O., Wallace, J. K., Bowler, B., Liu, M., Ruane, G., Serabyn, E., Bartos, R., Wang, J., Vasisht, G., Fitzgerald, M., Skemer, A., Ireland, M., Fucik, J., Fortney, J., Crossfield, I., Hu, R., & Benneke, B. 2016, in Proceedings of the SPIE, Volume 9909, id. 99090D 7 pp. (2016)., Vol. 9909, 99090D

Renker, D. 2006, Nuclear Instruments and Methods in Physics Research A, 567, 48

Salama, M., Baranec, C., Jensen-Clem, R., Riddle, R., Duev, D., Kulkarni, S., & Law, N. M. 2016, in Proceedings of the SPIE, Volume 9909, id. 99091A 15 pp. (2016)., Vol. 9909, 99091A

Szypryt, P., Meeker, S. R., Coiffard, G., Fruitwala, N., Bumble, B., Ulbricht, G., Walter, A. B., Daal, M., Bockstiegel, C., Collura, G., Zobrist, N., Lipartito, I., & Mazin, B. A. 2017, Optics Express, 25, 25894

Welch, P. D. 1967, IEEE Trans. Audio and Electroacoust., Volume AU-15, p. 70-73, 15, 70

Wizinowich, P., Chun, M., Mawet, D., Agapito, G., Dekany, R., Esposito, S., Fusco, T., Guyon, O., Hall, D., Plantet, C., & Rigaut, F. 2016, in Proc. SPIE, Vol. 9909, Adaptive Optics Systems V, 990915

Chapter 4

Measurements of Speckle Lifetimes in Near-Infrared Extreme Adaptive Optics Images for Optimizing Focal Plane Wavefront Control

Note: this chapter has been submitted to PASP and is currently under review. Co-authors include Olivier Guyon, Donald N.B. Hall, Nemanja Jovanovic, Julien Lozi, and Frantz Martinache. A formal reference and DOI for this paper is not yet available.

Abstract

Although extreme adaptive optics (ExAO) systems can greatly reduce the effects of atmospheric turbulence and deliver diffraction-limited images, our ability to observe faint objects such as extrasolar planets or debris disks at small angular separations is greatly limited by the presence of a speckle halo caused by imperfect wavefront corrections. These speckles change with a variety of timescales, from milliseconds to many hours, and various techniques have been developed to mitigate them during observations and during data reduction. Detection limits improve with increased speckle reduction, so an understanding of how speckles evolve (particularly at near-infrared wavelengths, which is where most adaptive optics science instruments operate) is of distinct interest. We used a SAPHIRA detector behind Subaru Telescope's SCExAO instrument to collect H-band images of the ExAO-corrected PSF at a frame rate of 1.68 kHz. We analyzed these images using

two techniques to measure the timescales over which the speckles evolved. In the first technique, we analyzed the images in a manner applicable to predicting performance of real-time speckle nulling loops. We repeated this analysis using data from several nights to account for varying weather and AO conditions. In our second analysis, which follows the techniques employed by Milli et al. (2016) but using data with three orders of magnitude better temporal resolution, we identified a new regime of speckle behavior that occurs at timescales of milliseconds and is clearly due to atmospheric (not instrumental) effects. We also observed an exponential decay in the Pearson's correlation coefficients (which we employed to quantify the change in speckles) on timescales of seconds and a linear decay on timescales of minutes, which is in agreement with the behavior observed by Milli et al. For both of our analyses, we also collected similar datasets using SCExAO's internal light source to separate atmospheric effects from instrumental effects.

4.1 Introduction

Extreme adaptive optics (ExAO) images consist of a point spread function (PSF) and a surrounding halo of speckles. The PSF's size is determined by the diffraction limit of the telescope and the wavelength of observations, and the speckle halo has an angular size corresponding to that of the natural atmospheric seeing. The speckle halo is composed of speckles with intensities up to a few 10^{-3} times the intensity of the PSF core. Speckle causes include diffraction within the optical train and imperfect AO corrections due to time lag between wavefront sensing and correction, non-common path aberrations introduced between the wavefront sensor and science camera, and imperfect wavefront measurements due to noise. These speckles evolve on a variety of timescales, from hours (diffraction from the telescope spiders, for example) to millisecond (the deformable mirror's imperfect corrections for atmospheric turbulence) (Macintosh et al. 2005).

These speckles reduce the ability to detect faint features near a star such as extrasolar planets or debris disks, and their effect is orders of magnitude higher than photon noise.

Racine et al. (1999) showed that the limiting brightness for detection is proportional to $(1 - S)/S$ where S is the Strehl ratio, which emphasizes the need for ExAO instruments producing high-Strehl corrections. The Strehl ratio is the comparison of the peak intensity of the measured PSF to the intensity of a PSF diffracted by the telescope pupil but otherwise unaberrated (Strehl 1902). The Strehl ratio will never be 100% for ground-based astronomical observations, so there will always be speckles, and several techniques have been developed to differentiate between them and actual structure in the science target. These include angular differential imaging (Marois et al. 2006) (which takes advantage of the rotation of the sky relative to an alt/az telescope) and spectral differential imaging (Smith 1987) (which utilizes the fact that the speckle halo expands with increasing wavelengths, but features in the target do not). However, because these techniques are implemented after the data have been collected, they do not remove the shot noise caused by the speckles. Additionally, because they are typically applied to long exposures, they have no effect on quickly-changing speckles. These techniques have been applied to obtain contrasts on the order of 10^{-6} at several tenths of an arcsecond from the PSF core. However, Earth-like planets in the habitable zones of M dwarfs have contrasts on the order of 10^{-7} to 10^{-8} (Guyon et al. 2012), and an Earth-like planet around a Sun-like star has a contrast of 10^{-10}, so better speckle reduction strategies need to be implemented if such planets are to be detected.

Various techniques have been proposed for real-time speckle nulling loops (e.g. Bordé & Traub 2006; Give'on et al. 2007; Sauvage et al. 2012; Guyon 2004; Baudoz et al. 2006; Serabyn et al. 2011). These provide two advantages over post facto speckle mitigation techniques such as those discussed above. First, they are able to reduce some of the dynamic speckles in addition to the static ones. However, the temporal bandwidths of the speckle nulling loops that have been implemented on-sky have been relatively slow (Martinache et al. 2014), and these loops did nothing for speckles with lifetimes shorter than several seconds. A loop's temporal bandwidth determines to what extent the short-lived speckles can be reduced. The second advantage of real-time speckle nulling loops is that, because

they utilize interference principles to null the speckles, they remove the speckles' shot noise as well.

The lifetimes of speckles determine a given technique's ability to mitigate them, so several attempts have been made to define and measure speckle lifetimes. Vernin et al. (1991) was interested in speckle interferometry (a high-resolution technique that predates adaptive optics) and performed early speckle lifetime measurements. Macintosh et al. (2005) simulated speckle lifetimes in coronagraphic and noncoronagraphic data, and Stangalini et al. (2017) measured speckle lifetimes in AO-corrected visible-wavelength images using techniques more commonly applied to solar photospheric characterization. Milli et al. (2016) quantified the temporal changes in speckles by calculating Pearson's correlation coefficients (Pearson 1895) for frames separated by varying amounts of time. This analysis was most similar to ours; we describe their methods and results in Section 4.4.1. In this paper, we describe an experiment which utilizes high frame rate SAPHIRA speckle observations to identify the timescales over which speckles change and predict the contrast improvement that could be enabled by a real-time speckle nulling loop.

4.2 Experimental Setup and Observations

The Subaru Coronagraphic Extreme Adaptive Optics instrument (Jovanovic et al. 2015b) (SCExAO) is an instrument at Subaru Telescope atop Maunakea in Hawaii. It utilizes a pyramid wavefront sensor and 2000-element deformable mirror (DM) updating at typically 2 kHz. AO188 (Minowa et al. 2010), Subaru's facility AO system, provides preliminary corrections, and then SCExAO provides high-order corrections in order to achieve Strehls of 80-90% at H band (e.g. Kühn et al. 2018). SCExAO is designed to observe high-contrast objects such as extrasolar planets, brown dwarfs, and debris disks (Jovanovic et al. 2013, 2016). Numerous different modules can utilize SCExAO's corrected beam. Visible light is sent to the VAMPIRES (Norris et al. 2015) and FIRST (Huby et al. 2012) aperture-masking interferometers. Infrared light can be directed to the CHARIS integral field

spectrograph (Groff et al. 2017), First Light Imaging C-RED 2 internal science camera (Gach et al. 2018), or the SAPHIRA camera.

SAPHIRA (Baker et al. 2016) is a 320×256@24 μm pixel HgCdTe linear avalanche photodiode detector manufactured by Leonardo. It has low dark current (Atkinson et al. 2017) and noise and an adjustable gain, and it is optimized for high frame rates (up to 10 MHz per channel clocking frequencies). At bias voltages of $\sim$ 18 V, SAPHIRA detectors have a multiplication gain of several hundred (Atkinson et al. 2016). Because this gain multiplies the signal but not the read noise, SAPHIRA has the potential for photon-counting performance (Atkinson et al. 2018; Finger et al. 2016). SAPHIRA detectors can be read using 1, 4, 8, 16, or 32 outputs. Regardless of whether it is a full frame or subarray being read, the outputs read adjacent pixels. Therefore, unlike HAWAII detectors, all outputs are used even when reading a subarray, and therefore the frame rate scales approximately inversely with the number of pixels being read (Goebel et al. 2018). We operated the SAPHIRA using a controller developed at the University of Hawaii Institute for Astronomy affectionately called the "Pizza Box" due to its shape.

During SCExAO engineering nights on UTC May 31, August 13, August 15, and September 11, 2017, we recorded SAPHIRA images of unresolved stars. These observations are summarized in Table 4.1. No coronagraph was used. The detector was subwindowed to 128 × 128 pixels (approximately a 1 arcsecond square) in order to achieve a frame rate of 1.68 kHz. During the first three nights, the PSF core was saturated by a factor of $\sim$ 10 in order to obtain a better signal to noise ratio (SNR) for the speckles; this data were used in the analysis of Section 4.3.2. On the night of September 11, most of the dynamic range of the detector was used, but the PSF core was not saturated; this data were used for the analysis of Section 4.4.2. On all nights, the SAPHIRA detector was operated in "read-reset" mode, wherein each line was read once and then reset. This enabled a maximum effective frame rate, optimal duty cycle, and full use of the dynamic range per image (Goebel et al. 2018). We later collected dark/bias frames and subtracted these in order to remove the detector's pedestal pixel-by-pixel offset pattern. In our previous speckle

Table 4.1. A summary of observations.

UTC Date	Target	Seeing at 0.5 μm (arcsec)	Wind Speed (m/s)	Strehl Ratio
May 31, 2017	Vega	0.9	0	92% measured
August 13, 2017	Altair	0.35	0	70% estimated
August 15, 2017	β And	Unreported	5	90% measured
September 11, 2017	63 Cet	0.35	1	90% estimated

Note. — The Strehl ratios were calculated from individual sub-millsecond exposures at H band, so they do not include the blurring effects of tip and tilt. The seeing measurements were produced by the Canada France Hawaii Telescope (CFHT) MASS/DIMM monitor, and the wind speeds are those recorded by the CFHT weather station. This is located approximately 750 m from Subaru Telescope.

lifetime measurements (Goebel et al. 2016), we operated the detector in up-the-ramp mode (multiple reads followed by a reset) and then subtracted adjacent reads. This resulted in irregular time sampling and much poorer SNR due to having to split the flux over multiple reads. Additionally, in the previous observations, we used the PSF core to align the images in post-processing, so we did not saturate it during observations. We have since developed other techniques as described below for tip/tilt correction in post-processing. For these reasons, our more recent observations are much higher quality than the older ones.

The May and August nights produced the data used in the analysis presented in Section 4.3.2. On those nights, datasets were collected with SCExAO+AO188 (extreme adaptive optics) corrections, AO188 corrections only, and with no adaptive optics. In each regime, approximately one minute of data was collected with each of a 10 nm bandpass filter centered at 1550 nm, a 50 nm bandpass filter centered at 1550 nm, and a full H filter (about 260 nm bandpass). The narrower bandpass filters enabled better resolving of the speckles because they reduced the speckles' chromatic elongation. The three bandpasses in each of the three AO regimes produced nine datasets per night. In order to align images and

provide a flux calibration, we applied an astrometric grid (Jovanovic et al. 2015a) during observations. In short, sine waves in orthogonal directions with frequencies optimized to the DM actuator pitch were applied to the DM. This generated an artificial speckle in each corner of the detector. By alternating the phase of the sine waves between 0 and π on timescales shorter than individual SAPHIRA exposures, the astrometric speckles became effectively incoherent with the speckle halo [1]. This avoided coherent interference between the electric fields of the artificial and natural speckles that could distort the position and lifetime measurements. These astrometric speckles were 5.1×10^{-3} times the brightness of the PSF core for the May 31 observations and 2.6×10^{-3} the brightness of the PSF core during the August observations. We used these astrometric speckles to 1) align the images in order to remove tip/tilt, and 2) photometrically calibrate the speckle brightnesses.

The data from September 11 were used for the analysis presented in Section 4.4.2. We were interested in longer-term speckle evolution, so we collected seven minutes of ExAO-corrected PSF data. We again used the 50 nm bandwidth filter centered at 1550 nm; this bandwidth provided a good balance between throughput and chromatic speckle elongation. We did not use the astrometric speckle grid on this night; we aligned the images during processing by cross-correlating the speckle patterns from one image to the next.

SCExAO has an internal broadband light source and optics which simulate the telescope pupil (Jovanovic et al. 2015b). This produces a nearly-static PSF whose temporal evolution is solely due to instrumental effects. We observed this light source using the same camera settings as were used on-sky and then reduced the data using the same techniques as were employed for the on-sky observations. This enabled us to separate instrumental effects from actual atmospheric behavior. However, because this light source is internal to SCExAO, we were not able to probe the behavior of the telescope, image rotator, atmospheric dispersion corrector, or AO188 apart from the on-sky observations.

[1] The speckle phase was modulated with a frequency four times SAPHIRA's average frame rate. It was not perfectly synchronized to the exposures, so some very small residual coherence remained. However, this effect did not matter because the region used for speckle lifetime calculations did not include the astrometric speckles.

4.3 Speckle Lifetime Measurements for Real-Time Speckle Nulling

4.3.1 The Benefits and Techniques of Real-Time Speckle Nulling

Unlike speckles subtracted away during post-observation image processing, speckles interferometrically destroyed during observations do not leave behind photon noise. Because a speckle is fundamentally scattered starlight, it is possible to apply equal-amplitude but out-of-phase starlight on top of it and thereby destructively interfere it away. On the other hand, light from a substellar companion is not coherent with the starlight, so it cannot be destructively nulled away.

A number of techniques have been proposed to differentiate between speckles caused by scattered starlight and substellar companions and then mitigate the speckles. The pioneering work in real-time speckle nulling algorithms and conceptually most straightforward method was proposed by Bordé & Traub (2006). The focal plane, which is where the science detector is located, shows the Fourier transform of the pupil plane, which is where the deformable mirror is located. A sine wave on the DM generates delta functions (PSFs) on the science detector. This is shown in Figure 4.1. The amplitude, phase, orientation, and frequency of the sine wave on the DM determines the brightness, phase, location, and spacing of the artificial speckles on the science detector. Therefore, one can generate an artificial speckle in the same location as an existing speckle, scan through phase space to find the opposite complex amplitude, and thereby null it away. The upside of this technique is that it is robust and does not require a detailed system model. The primary downside is that several phase measurements need to be made before a speckle can be nulled, so it is not as fast as other algorithms. Martinache et al. (2014) implemented this speckle nulling algorithm on SCExAO. In practice, it worked well on the SCExAO internal light source for quasi-static speckles, but because the camera used operated at $\sim$ 170 Hz and was noisy, and the loop required many phase measurements per iteration, it was not fast enough to affect the dynamic speckles when tested on-sky.

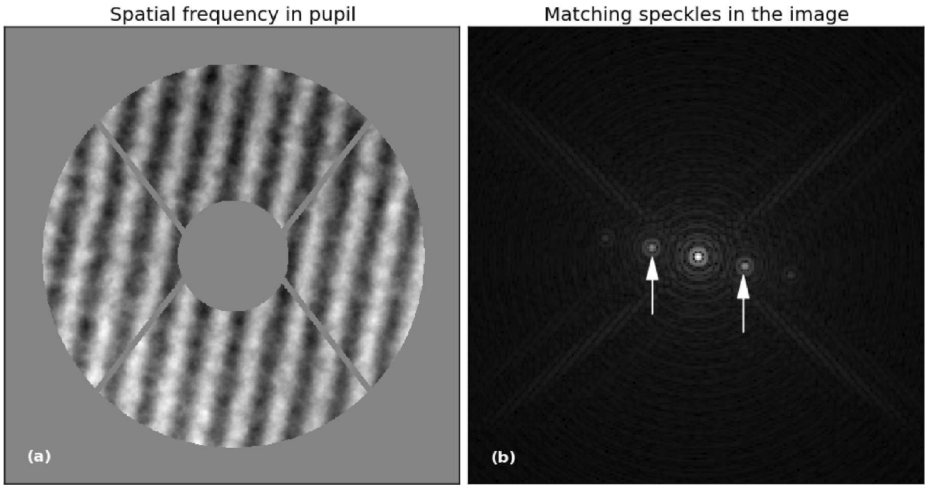

Figure 4.1 On the left is a map of deformable mirror displacement, and on the right are the resulting speckles produced in the focal plane. By varying the orientation, frequency, amplitude, and phase of the sine wave on the DM, one varies the location, spacing, brightness, and phase of the artificial speckles, respectively. Multiple sine waves can be applied in order to produce multiple speckles. Figure reproduced from Martinache et al. (2014).

A more complex but potentially faster speckle nulling method known as "electric field conjugation" was proposed by Give'on et al. (2007). This method places small displacements on the deformable mirror to derive the electric field and thereby phase of speckles. It has produced the deepest contrasts (on the order of 10^{-9}) in highly stable high contrast imaging laboratories, but it requires a detailed system model and high signal to noise because the actuator pokes are quite small. The theory of this technique forms the basis of several other proposed speckle nulling ideas. Other techniques for real-time speckle discrimination include coronagraphic focal plane wavefront estimator for exoplanet imaging (COFFEE) (Sauvage et al. 2012), the self-coherent camera (Baudoz et al. 2006), the phase-shifting interferometer (Serabyn et al. 2011; Bottom et al. 2017), synchronous interferometric speckle subtraction (Guyon 2004), and linear dark field control (Miller et al. 2017). However, apart from the implementation by Martinache et al. (2014) of the technique of Bordé & Traub (2006), none of these methods have been used for speckle nulling on-sky. This is primarily because they are optomechanically complex, require a higher degree of PSF stability than can be achieved on-sky, require very high Strehl ratios, or require deformable

mirror perturbations that would be detrimental to science observations. Jovanovic et al. (2018) provides an informative review of these techniques.

Regardless of the particular algorithm, our speckle lifetime measurements are critical to quantify closed loop speckle nulling performance. As loop bandwidth increases, shorter-lived speckles can be destroyed, and therefore the focal-plane contrast and detection limits improve. An understanding of the rates at which speckles change is important because it influences the feasibility of implementing the loops described above and gives the bandwidth necessary to reach a given performance level.

4.3.2 Our Observations and their Interpretation

Our goal is to measure how speckles evolve as a function of time and brightness. We quantified this using a new technique described below. The single largest detriment to image quality at SCExAO is tip/tilt caused by vibrations from the telescope and instrument (Lozi et al. 2016), which causes translation of the speckles instead of evolution, so it needed to be mitigated. Therefore, we began by aligning all the images. The results of the image alignment are shown in Figure 4.2. We located the artificial astrometric speckles and aligned images using those, and as a check also cross-correlated each image against the next to detect shifts. Both techniques registered images to ~ 0.01 pixel accuracy and produced similar results.

Second, we selected all pixels within a radius of $4\lambda/D < r < 10\lambda/D$ of the PSF core. Given that the observed intensity I of a speckle is the square of the modulus of complex amplitude $\mathbf{A}$,

$$I = |\mathbf{A}|^2 \,, \tag{4.1}$$

it follows that

$$\frac{dI}{dt} = 2\mathbf{A}\frac{d\mathbf{A}}{dt} \,. \tag{4.2}$$

$\mathbf{A}$ is a random variable with a characteristic evolutionary timescale (temporal derivative). This is due to linearity between $\mathbf{A}$ and turbulence in the pupil, which to first degree, over

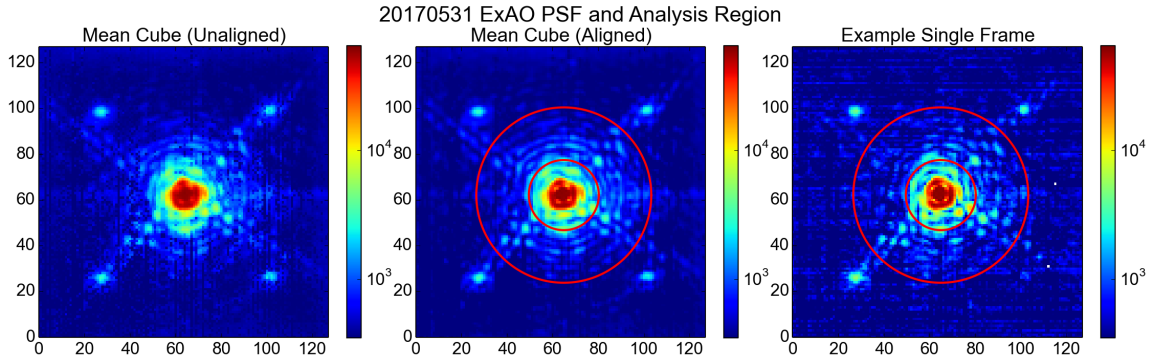

Figure 4.2 Shown are three sample logarithmically scaled ExAO-corrected PSFs from the May 31, 2017 dataset. The four bright speckles in the corners are the artificial astrometric speckles we created for image registration and photometry (the PSF core couldn't be used because it was saturated). Overplotted on the second and third images are circles indicating $r = 4\lambda/D$ and $r = 10\lambda/D$ (the region within which we analyzed speckle lifetimes). The left image shows the result of coadding 10,000 frames (6 s of data), and the middle one shows the same coaddition after the images were aligned. Due to the alignment, the middle image exhibits many more airy rings and better-defined speckles than the left one. The right image is a sample individual frame. One astrometric speckle appears to be missing due to a combination of a rolling shutter effect and the astrometric speckle modulation.

short timescales, has a linear temporal evolution (fixed derivative). Therefore, $d\mathbf{A}/dt$ is static over short timescales, and brighter (larger I) speckles will change more quickly than dimmer ones. Because of this, we sorted the pixels into four brightness bins (we selected the 20-30 percentile brightness pixels, 40-50 percentile, etc.). For each selection of pixels, we subtracted those pixels from the same pixels time t later. This formed a difference image. Finally, we calculated the standard deviation of these difference images in order to measure how the pixels changed in brightness over that time interval. If a pixel did not change in brightness, this quantity would be 0. We divided the standard deviation by the peak brightness of the PSF core so that it had units of contrast. We repeated this process for each image compared to $1 - 260$ frames after it, and then averaged all the measurements at a given temporal separation to improve the signal to noise. We plotted this quantity against time for each brightness bin in Figures 4.3 (extreme AO, AO188 only, and no AO on the night of May 31, 2017) and 4.4 (extreme AO on August 13 and 15, 2017).

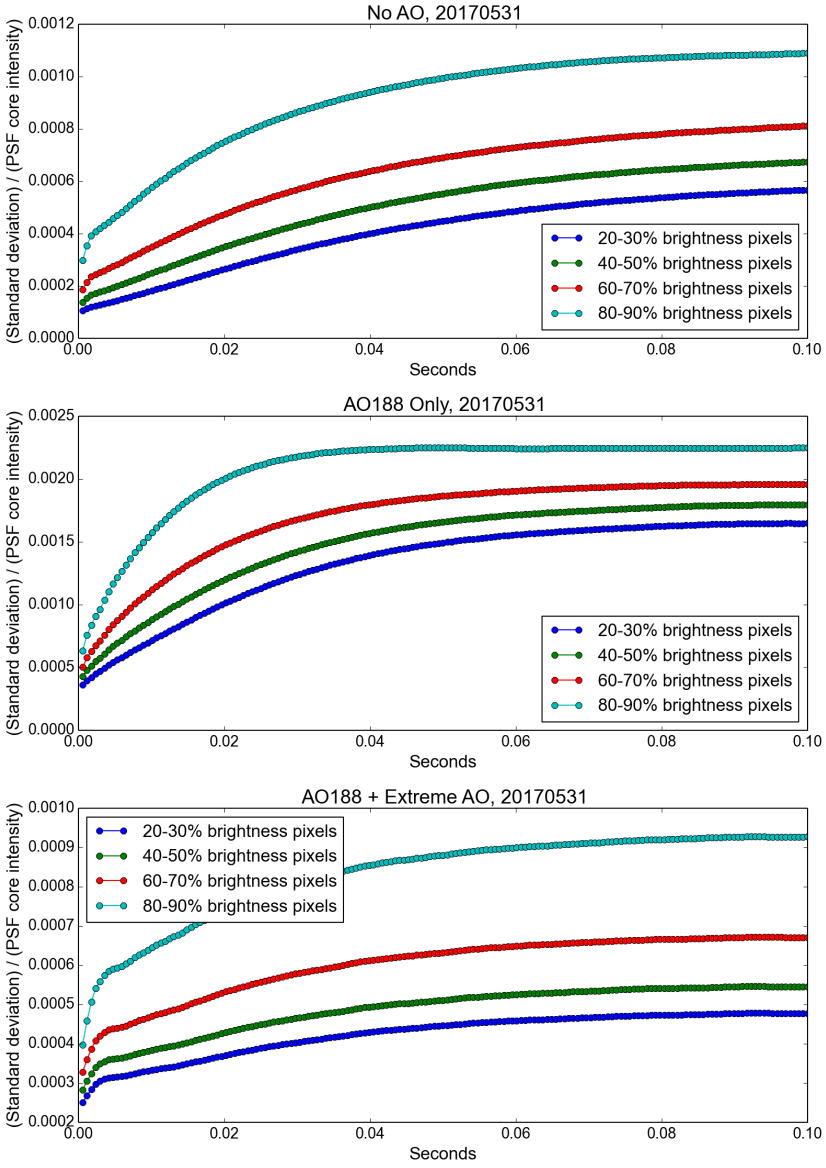

Figure 4.3 Shown here are the speckle evolution plots for four different brightness bins and the three different AO regimes (no AO, AO188 only, and AO188+ExAO) on the night of May 31, 2017. AO188 corrections reduced the standard deviation in speckle brightness relative to having no AO, and ExAO again reduced it relative to AO188. We divided the calculated standard deviations by the PSF core brightness in order to express them in units of contrast. It should be noted that the non-AO images were nowhere near diffraction-limited, so dividing the standard deviations by the peak brightness of the image resulted in misleadingly optimistic contrasts. The plots approach asymptotic values at large temporal separations because the speckles have entirely changed. As predicted by Equation 4.2, the brighter speckles change more rapidly than the dimmer ones.

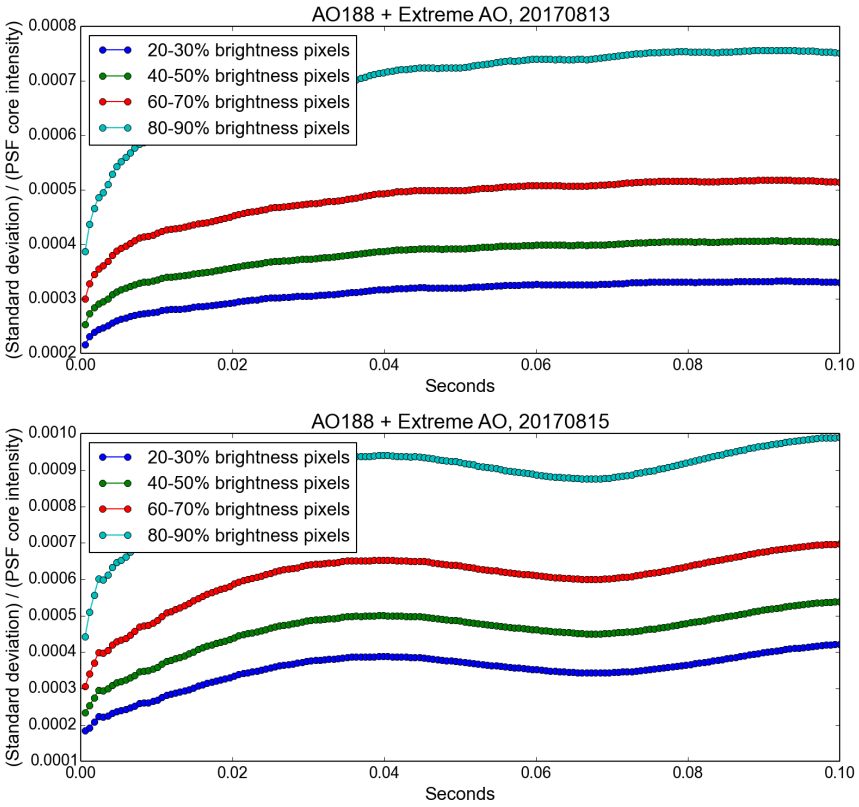

Figure 4.4 These two plots are equivalent to the bottom plot in Figure 4.3, but were produced using the extreme AO data collected on August 13 (top) and 15 (bottom), 2017. The seeing and AO tuning were significantly different in each of the three nights. The minor oscillation of the August 15 plot is likely due to a vibration that was not completely removed by our image alignment. We divided the calculated standard deviations by the PSF core brightness in order to express them in units of contrast.

To understand whether the behavior of the standard deviations illustrated in Figures 4.3 and Figures 4.4 was in fact due to speckle behavior or merely instrumental effects, we observed the SCExAO internal light source. There were no moving components in this setup. As is illustrated in Figure 4.5, indeed that speckle behavior is entirely static over the timescales examined. Second, we ran unilluminated frames through the above analysis pipeline in order to see how noise affected the plot's behavior. Again, the standard deviations were static in time. This means that the behavior in Figures 4.3 and Figures 4.4 was indeed caused by the temporal evolution of the on-sky speckles.

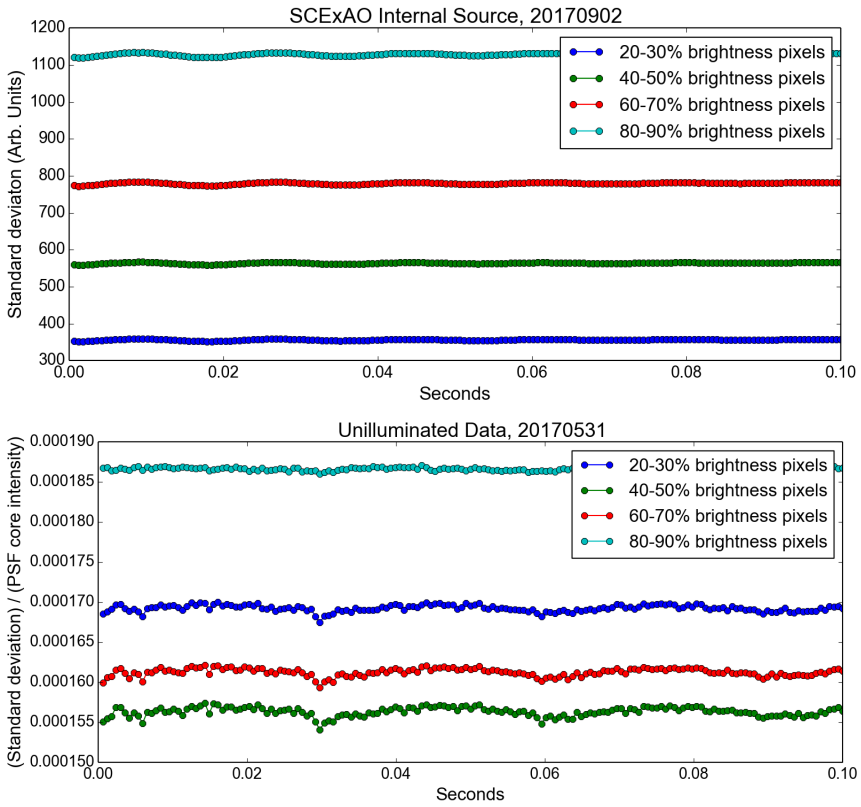

Figure 4.5 In order to understand whether the behavior illustrated in Figures 4.3 and 4.4 was due to intrinsic atmospheric speckle evolution, we computed the standard deviations using images of the SCExAO internal light source and also dark frames collected immediately following the May 31 on-sky observations. The internal PSF data are reassuringly flat with time, indicating that the speckle evolution of the previous plots is not due to instrumental effects. A photometric calibration was not available for this data, so it is expressed in arbitrary brightness units. In the lower plot, the noise data are also flat with time. This has been scaled by the PSF brightness from the ExAO images collected a short time earlier in order to express it in units of contrast. The order of the relative brightnesses in this second plot is different from the other plots. This is most likely due to the behavior of pixels on the tails of the responsivity distribution; well-behaved pixels have the lowest standard deviations when unilluminated, and "bad" pixels are more prone to wandering and therefore higher standard deviations.

In all cases, the brighter speckles change in brightness more rapidly than the dimmer ones. This confirms the behavior we expected from Equation 4.2. The implication of this is that once a dark hole is present in an image, it is easier for a speckle nulling loop to keep it dark. Because a dimmer speckle changes more slowly, more speckle nulling loop iterations can be carried out before it changes. Therefore, the performance of a real-time speckle nulling loop will be highly affected by the Strehl ratio and/or presence of a coronagraph that creates dark holes in the image.

On sufficiently short timescales, the complex amplitude can be approximated as behaving linearly with time, i.e.

$$\mathbf{A}(t) \approx at + a_0 + bti + b_0 i \tag{4.3}$$

where a and b are the rates at which the real and imaginary parts of $\mathbf{A}$ change, respectively, and a_0 and b_0 are their initial values. Inserting this into Equation 4.1 and computing the measured intensity as a function of time $I(t)$ produces

$$I(t) = (a^2 + b^2)t^2 + (2aa_0 + 2bb_0)t + (a_0^2 + b_0^2)\ . \tag{4.4}$$

Therefore, the measured intensity of a speckle is a quadratic function of time, and its behavior depends on the complex amplitude's initial value and temporal rate of change. The standard deviation of pixel intensity, which is what we plotted in Figures 4.3-4.5, behaves the same way. For example, if a speckle is entirely static, then $a = b = 0$, and $I(t) = a_0^2 + b_0^2$, and this produces a flat line in the plot with a y-intercept which depends on the brightness the speckle. This exact case is illustrated in the top panel of Figure 4.5. On the other hand, the other simple case occurs when the speckles are changing (i.e. $a \neq 0$ and $b \neq 0$) but start from zero intensity ($a_0 = b_0 = 0$). In this case, the plot would exhibit an upward parabola centered at the origin. We approach this limit (but do not reach it) in the on-sky observations by selecting increasingly dim speckles (i.e. $a_0 \to 0$ and $b_0 \to 0$) for analysis.

Depending on the temporal sampling of the data, the initial brightness of the speckles, and the rates at which they change, this upward parabolic behavior may not be obvious in real-world measurements. The first few data points in the May 31 ExAO plot appear linear, the first few points in the August 13 plot appear downwardly parabolic, and only in the August 15 plot are the first few points plausibly upwardly parabolic. It is possible that our data are not fast enough to recover this predicted effect, and it would become apparent in data with even faster temporal sampling. Additionally, the behavior described above assumes that the complex amplitude at a pixel changes linearly with time, and it certainly departs from this after a few milliseconds. Indeed, at sufficiently long timescales, the speckles have entirely changed from their initial state, causing the measured standard deviations to plateau. This is why our plots approach asymptotic standard deviations at increasing time.

If the behavior described by Equation 4.4 was evident in the images, one could predict the performance of real-time speckle nulling loops from it. Since it is unclear whether our data reveal the predicted behavior, we will not do that, but we will explain how it could be done. If our analysis described above could be carried out at even higher temporal sampling or in an extremely high Strehl case, and the upward parabolic behavior revealed itself, one could fit a second-order polynomial to it. Solving this quadratic equation would provide the contrast that could be achieved at a given speckle nulling loop bandwidth. The y-intercept in this fit would correspond to the read and photon noise (i.e. the noise that would be present if it was possible to image repeatedly with zero time between the images and with zero speckle evolution). A real-time speckle nulling loop would zero the linear and constant terms with each update by forcing $a_0 = b_0 = 0$. In this case, $I(t) \propto t^2$. Therefore, the achievable contrast would increase with the square of the speckle nulling loop bandwidth (where bandwidth is $1/t$). This result emphasizes the major impact that speckle nulling loops will have on detection limits.

4.4 A different approach: extending the analysis of Milli et al.

4.4.1 Milli et al.'s Technique and Results

Milli et al. (2016) employed a different technique for measuring the timescales over which speckles evolve. Their observations were comparable to ours, so we analyzed our comparatively higher frame rate data using their methods. They collected H-band images at a frame rate of 1.6 Hz of coronagraphic PSF images from the SPHERE ExAO instrument. They then quantified the change in speckles over the 52 minutes of their on-sky observations by computing Pearson's correlation coefficient (Pearson 1895) for pairs of images. Pearson's correlation coefficient $\rho(t_i, t_j)$ between two frames collected at times t_i and t_j can be defined as follows:

$$\rho(t_i, t_j) = \frac{\sum_{x \in S} [I(x, t_i) - \overline{I_{t_i}}][I(x, t_j) - \overline{I_{t_j}}]}{\sigma_{t_i} \sigma_{t_j} N_{\text{pix}}} \tag{4.5}$$

where the sum occurs over all pixels in the region S, I is the instantaneous intensity at a given pixel with position x, $\overline{I}$ is the instantaneous average intensity over the region, σ is the spatial standard deviation over the region, and N_{pix} is the number of pixels in the region. The normalization is chosen so that $\rho = 1$ when $t_i = t_j$ (equivalently, if the speckles did not change at all between images at t_i and t_j, $\rho = 1$). Milli et al. (2016) provided a derivation in their Appendix C demonstrating that this quantity is directly related to the contrast obtained after subtracting one image of the pair from the other. The signal to noise of ρ for a single pair of frames is typically quite poor, so they improved it by averaging the values of ρ computed for many frame pairs separated by equal amounts of time.

After completing their on-sky observations, Milli et al. (2016) observed the instrument's internal light source and repeated the analysis in order to separate atmospheric effects from instrumental effects. In both cases, they observed two primary temporal regimes of speckle decorrelation. Over the first few seconds of their observations, the speckles decorrelated rapidly with an exponential decay. They fitted the first 30 seconds of their measurements

with the equation

$$\rho(t) = \Lambda e^{-t/\tau} + \rho_0 \tag{4.6}$$

and found best-fitting values of $\tau = 3.5$ s, $\Lambda = 0.059$, and $\rho_0 = 0.713$ for their on-sky observations. They initially posited that these speckles were primarily residuals of uncorrected atmospheric turbulence, but were surprised when then data collected using the internal light source exhibited the same behavior (in that case, they found $\tau = 6.3$ s). They performed additional tests but were not able to identify the fundamental cause of this behavior, and in the end concluded that it was "real [and] related to an internal effect in the instrument independent of the atmospheric conditions or the telescope."

For images separated by greater than a minute, they observed a second regime of speckle change. They observed a linear decorrelation with time, and this was again present in both the on-sky data and also their internal lamp data. They suggested that this change in speckles must be caused by mechanical changes in the instrument (in particular the motion of the image derotator and thermal expansion effects). When they disabled the image rotator, this linear decorrelation of speckles became flat with time, i.e. the speckles were not measurably changing. In summary, they observed two regimes of speckle decorrelation, and these had different timescales for the on-sky and off-sky observations, but both were fundamentally caused by instrumental and not atmospheric effects.

4.4.2 Analysis of Our Data Using this Technique

Our data also consisted of H-band images of an ExAO-corrected PSF, but it had three orders of magnitude higher temporal resolution, enabling us to probe far shorter timescales. Additionally, since SCExAO is an entirely different instrument from SPHERE, we hoped our data might shed light on Milli et al. (2016)'s instrumental effects.

Our data had some important differences, however. First, the SPHERE data were collected behind a Lyot coronagraph, whereas our data were noncoronagraphic. Second, their data were full H-band, whereas our images used a 50 nm passband filter centered at

1550 nm, which reduced the chromatic elongation of speckles and thereby enabled them to be better resolved. Finally, while their data were collected over 52 minutes, our data were 7 minutes in length, so we could not examine as long as timescales. We also recorded two 20 minute datasets of the SCExAO internal light source in order to differentiate between instrumental and atmospheric effects.

We then calculated Pearson's correlation coefficients according to Equation 4.5 using the annular region centered on the PSF and defined by radial separations $3\lambda/D < r < 10\lambda/D$. Comparing each of the 630 thousand frames for the on-sky data and 1.99 million frames for the internal source data with each of the other frames in that dataset would have been computationally prohibitive. Therefore, we compared each frame against $1, 2, 3, \ldots, 200, 208, 216, \ldots, 8400, 10080, 11760, \ldots, 604800$ frames later. This enabled us to have maximum signal to noise at each calculated temporal separation, but we sacrificed temporal resolution at higher separations. In other words, we wanted the best time resolution at the shortest possible intervals, but settled for one Pearson's correlation coefficient data point every second at a time intervals greater than six seconds. This simplification reduced the computational load by 99.9%. Even after this, we calculated 852 million correlation coefficients for the on-sky data and 6.04 billion for the internal source data. The data points at a given temporal separation were then averaged to improve signal-to-noise. Because there are fewer frame pairs separated by large amounts of time, signal-to-noise decreased at larger separations. The on-sky dataset was seven minutes long, and we calculated correlation coefficients for data points up to six minutes apart in order to still have reasonable signal to noise at the larger separations. The computation of the Pearson correlation coefficients for each plot took several CPU-days. Figures 4.6 and 4.7 show the results for the on-sky and internal light source data, respectively.

We observed three timescales of speckle evolution in the on-sky data. First, and most interestingly, our high frame rate data revealed an effect that Milli et al. (2016) did not observe. Frames separated by $\lesssim 2$ ms are highly correlated in the on-sky data. After this time, the exponential decay behavior described in the next paragraph dominates. The

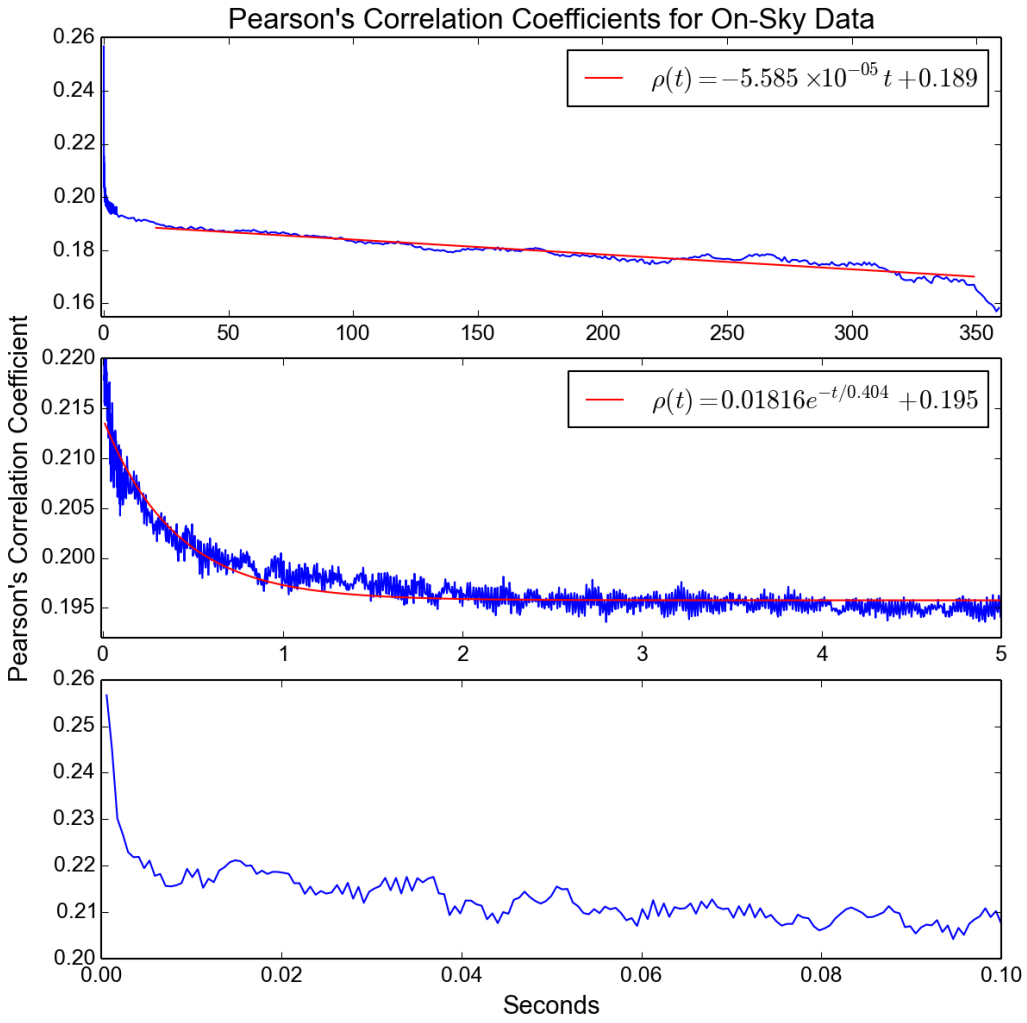

Figure 4.6 Plotted above are the Pearson's correlation coefficients calculated from seven minutes of SCExAO on-sky data. The same data are shown for three different timescales. Linear and exponential decays have been fitted to the data points between 20 and 350 s (top plot) and 0.1 and 5 s (middle plot), respectively. The coefficients of the fits are labeled. Unlike the plots of Section 4.3.2, less change in the speckles results in a higher value on the Y axis.

minimal change in data points separated $\lesssim 2$ ms is not present in the internal source data, implying that this is an actual atmospheric effect. This timescale is similar to the SCExAO loop bandwidth (2 kHz update rate and a $\sim 15\%$ gain), so it is most likely explained by the changes to the deformable mirror shape. Over timescales of > 2 ms, atmospheric speckles become de-correlated because they are corrected by the ExAO loop. Temporal correlations

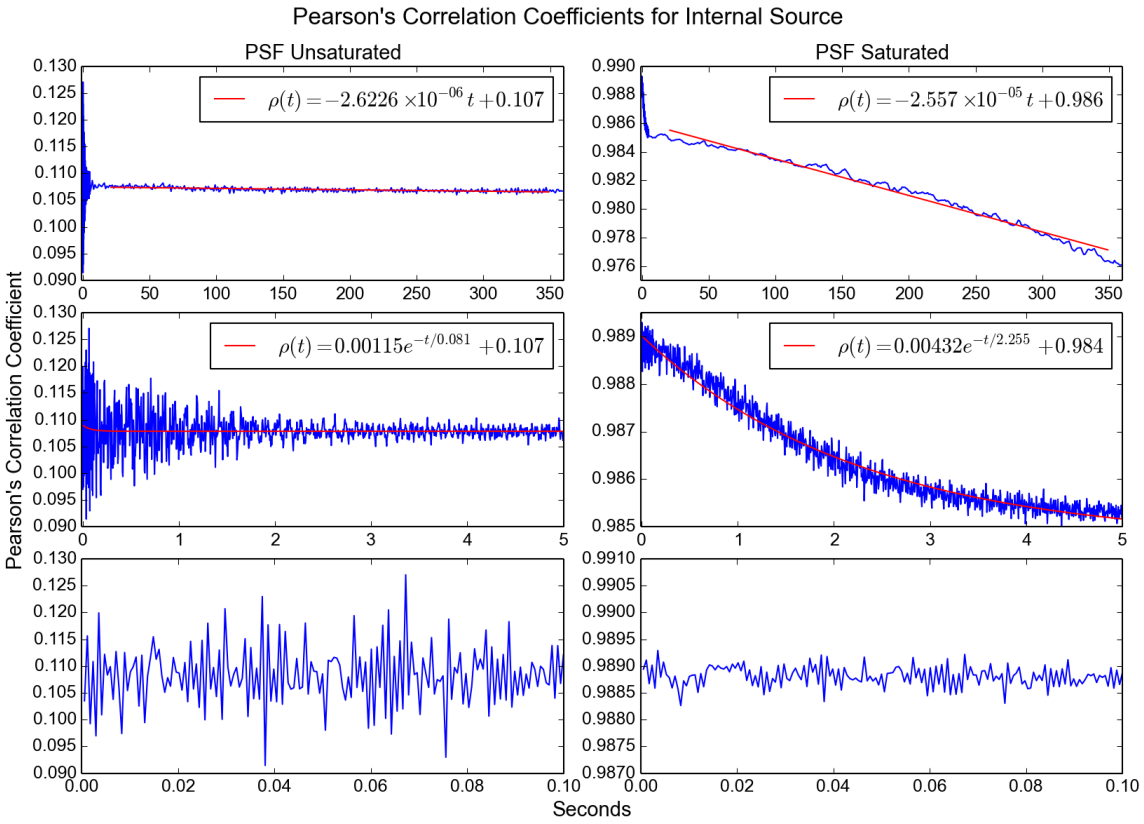

Figure 4.7 Plotted above are the Pearson's correlation coefficients calculated from two twenty-minute observations of the SCExAO internal light source. In the left plots, the PSF core was not saturated, mirroring our on-sky observations. However, because the PSF was nearly unaberrated, very few speckles were detectable, and no speckle evolution was measured. The dispersion in the correlation coefficients in these left plots is primarily caused by vibrations that were not perfectly removed by the image alignment process. On the right, the PSF has been saturated by a factor of 100, thereby improving the SNR of the speckles. In this case, timescales of speckle evolution are revealed. In each dataset, the correlation coefficients are shown for three different timescales. Linear and exponential decays have been fitted to the data points between 20 and 350 s (top plots) and 0.1 and 5 s (middle plots). The coefficients of the fits are labeled. Note that the high correlation between frames separated by $\lesssim 2$ ms of Figure 4.6 is not present in this data, indicating that it is an atmospheric and not instrumental effect.

that naturally exist at > 2 ms in the atmospheric speckles are erased or greatly attenuated by the ExAO correction; so there is a reduction in speckles with timescales of > 2 ms.

We recorded two 20-minute datasets using the SCExAO internal source. The first internal source dataset had an unsaturated PSF core, mirroring our September 11, 2017 on-

sky observations. However, because this was very nearly 100% Strehl (the slight degradation from 100% Strehl was due to imperfections in the optical elements of the instrument), very few speckles rose above the read noise of the detector. As a result, the calculation of the Pearson's correlation coefficients revealed no real speckle evolution (Figure 4.7 left plots). This mirrors the findings of Milli et al. (2016), who saw no speckle evolution when they froze the operation of SPHERE's optical elements. In order to improve signal-to-noise in the speckles, we then saturated the PSF core by a factor of 100 in the second internal source dataset (Figure 4.7 right side). In this case, we observed two timescales of decorrelation as described in the following paragraphs. Although the PSF core of the on-sky data was unsaturated, we could measure speckle evolution there because the Strehl was lower ($\sim$90% instead of $\sim$100%) and therefore the speckles were brighter.

We observed a second timescale on the order of minutes over which the speckles linearly decorrelated in both the on-sky data and the saturated internal source data. We fitted a first-order polynomial to data points between 20 and 350 seconds and found that the speckles decorrelated by 56 parts per million (PPM) on-sky and 26 PPM on the saturated internal source over this period. For comparison, Milli et al. (2016) measured 25 PPM and 9 PPM for these two timescales, respectively, but their fit was performed over a different range of times. Because this decorrelation is present in both the on-sky and internal source observations, it is fundamentally caused by an instrumental effect. Unlike Milli et al. (2016), we did not use the image derotator; we had no moving components between the light source and our detector. This decorrelation must therefore be due to thermal expansions in the mechanics of SCExAO. This data depart from this linear decorrelation between 300 and 360 seconds in the on-sky data, but we think this is due to small number statistics (there are fewer frame pairs with 6 minute separations than, for example, 1 minute separations) than any intrinsic speckle behavior. The internal source data did not exhibit this effect.

The third timescale we observed was an exponential decay in the Pearson's correlation coefficients over the first few seconds for both the saturated internal source and the on-sky data. Milli et al. (2016) also observed this behavior, but in our case it occurred much more

quickly. We fitted the points between 0.01 and 5 seconds with Equation 4.6 and found best-fitting parameters of $\tau = 0.40$ s for the on-sky data and $\tau = 2.3$ s for the saturated internal source. Our measured values for Λ and ρ_0 are provided on the plots, but these have fewer physical implications because they are influenced by the flux level on the detector, as demonstrated by Figure 4.7. In contrast, Milli et al. (2016) found exponential decay terms of $\tau = 3.5$ s and $\tau = 6.3$ s for their on-sky and internal light source data, respectively, when fitted to timescales between 1 and 30 seconds[2]. We observed a much more rapid decay than them, but the exponential decay behavior was present in both observations. Milli et al. (2016) were unable to explain the cause of this effect.

Whereas the analysis presented in Section 4.3.2 had applications to real-time speckle nulling, the results presented here are primarily applicable to speckle reduction during post processing. If the exposure times of individual images in an observing sequence are shorter than the timescales on which speckles evolve, then post-processing techniques such as KLIP (Soummer et al. 2012) and LOCI (Lafrenière et al. 2007) will be better able to subtract the speckles. For this reason, it is advantageous to use short exposures while conducting observations for which the speckle halo is relevant (this must be balanced against the read noise of the detector, emphasizing the need for low-noise detectors such as SAPHIRA or electron-multiplying CCDs). Although it is preferable to have the speckles as dim as possible, since these have minimal photon noise, it is also ideal for the speckles that still exist to evolve as slowly as possible, because this enables them to be mitigated during data reduction. This emphasizes the need to have the instrument maximally mechanically and thermally stable. Indeed, SPHERE has more thorough environmental/thermal stabilization than SCExAO, which likely explains why the speckle decorrelations measured in this section occur more rapidly than those of Milli et al. (2016).

[2]We performed the fits over a different range of times than Milli et al. (2016) because in the case of the linear decay, we simply didn't have long enough time coverage, and in the case of the exponential decay, the fit would have been poor if we fitted to the same 1-30 s range as them.

4.5 Conclusions

We collected H-band images of the speckle halo surrounding the SCExAO PSF at a framerate of 1.68 kHz. We then analyzed the data in order to see how speckles evolved as a function of time and brightness. We performed two analyses: we used a new technique to quantify speckle lifetimes with implications to real-time speckle-nulling loops, and we performed a second analysis with more general applications following the standard techniques in the literature. Our data used in the second analysis had three orders of magnitude higher temporal resolution than that used for previously published studies, and we identified a new timescale of speckle decorrelation. We observed that speckles were relatively static for timescales of $\lesssim 2$ ms in on-sky data, and we suggest that this timescale corresponds to the bandwidth of the ExAO loop. For timescales on the order of seconds and minutes, we observe similar behavior to that identified by Milli et al. (2016), namely an exponential decay over the first several seconds, followed by a linear decay over minutes. Mirroring the results of Milli et al. (2016), these two trends were present in both the on-sky and internal source observations. They noted that the linear decorrelation over minutes went away when the image rotator was stopped, but we observed this effect even without an image rotator.

An understanding of the timescales over which speckles evolve can inform the development and deployment of speckle mitigation techniques. A higher bandwidth speckle nulling loop can destroy a greater fraction of speckles and thereby enable the detection of higher-contrast substellar companions. For about 300 nearby M dwarfs, the angular separation of an Earth-like planet in the habitable zone at maximum orbital elongation would be at least 1 λ/D in the NIR for a 30-m-class telescope (Guyon et al. 2012), and the contrasts of these targets are in the range of $10^{-7} - 10^{-8}$. Although current techniques struggle to produce processed contrasts better than 10^{-6} at much larger angular separations, ELTs and the implementation of improved speckle reduction techniques, both during observations and during data processing, will enable observation of these targets.

ACKNOWLEDGMENTS

The authors acknowledge support from NSF award AST 1106391, NASA Roses APRA award NNX 13AC14G, and the JSPS (Grant-in-Aid for Research #23340051, #26220704, and #23103002). This work was supported by the Astrobiology Center (ABC) of the National Institutes of Natural Sciences, Japan and the director's contingency fund at Subaru Telescope. FM acknowledges ERC award CoG 683029. The authors wish to recognize the very significant cultural role and reverence that the summit of Maunakea has always had within the indigenous Hawaiian community. We are most fortunate to have the opportunity to conduct observations from this mountain.

References

Atkinson, D., Hall, D., Jacobson, S., & Baker, I. M. 2018, AJ, 155, 220

Atkinson, D. E., Hall, D. N. B., Baker, I. M., Goebel, S. B., Jacobson, S. M., Lockhart, C., & Warmbier, E. A. 2016, in Proc. SPIE, Vol. 9915, High Energy, Optical, and Infrared Detectors for Astronomy VII, 99150N

Atkinson, D. E., Hall, D. N. B., Jacobson, S. M., & Baker, I. M. 2017, AJ, 154, 265

Baker, I., Maxey, C., Hipwood, L., & Barnes, K. 2016, in Proceedings of the SPIE, Volume 9915, id. 991505 8 pp. (2016)., Vol. 9915

Baudoz, P., Boccaletti, A., Baudrand, J., & Rouan, D. 2006, in IAU Colloq. 200: Direct Imaging of Exoplanets: Science and Techniques, 553–558

Bordé, P. J. & Traub, W. A. 2006, ApJ, 638, 488

Bottom, M., Wallace, J. K., Bartos, R. D., Shelton, J. C., & Serabyn, E. 2017, MNRAS, 464, 2937

Finger, G., Baker, I., Alvarez, D., Dupuy, C., Ives, D., Meyer, M., Mehrgan, L., Stegmeier, J., & Weller, H. J. 2016, in Proc. SPIE, Vol. 9909, Adaptive Optics Systems V, 990912

Gach, J.-L., Feautrier, P., Stadler, E., Clop, F., Lemarchand, S., Carmignani, T., Wanwanscappel, Y., & Boutolleau, D. 2018, in Society of Photo-Optical Instrumentation Engineers (SPIE) Conference Series, Vol. 10539, 1053914

Give'on, A., Kern, B., Shaklan, S., Moody, D. C., & Pueyo, L. 2007, in Astronomical Adaptive Optics Systems and Applications III, Vol. 6691, 66910A

Goebel, S. B., Guyon, O., Hall, D. N. B., Jovanovic, N., & Atkinson, D. E. 2016, in Proc. SPIE, Vol. 9909, Adaptive Optics Systems V, 990918

Goebel, S. B., Hall, D. N. B., Guyon, O., Warmbier, E., & Jacobson, S. M. 2018, Journal of Astronomical Telescopes, Instruments, and Systems, 4, 1

Groff, T. D., Chilcote, J. K., Kasdin, J., Brandt, T., Galvin, M., Loomis, C., Carr, M., Knapp, G. R., Guyon, O., Jovanovic, N., Lozi, J., Takato, N., & Hayashi, M. 2017, in American Astronomical Society Meeting Abstracts, Vol. 229, American Astronomical Society Meeting Abstracts, 155.10

Guyon, O. 2004, ApJ, 615, 562

Guyon, O., Martinache, F., Cady, E. J., Belikov, R., Balasubramanian, K., Wilson, D., Clergeon, C. S., & Mateen, M. 2012, in Adaptive Optics Systems III, Vol. 8447, 84471X

Huby, E., Perrin, G., Marchis, F., Lacour, S., Kotani, T., Duchêne, G., Choquet, E., Gates, E. L., Woillez, J. M., Lai, O., Fédou, P., Collin, C., Chapron, F., Arslanyan, V., & Burns, K. J. 2012, A&A, 541, A55

Jovanovic, N., Absil, O., Baudoz, P., Beaulieu, M., Bottom, M., Carlomagno, B., Carlotti, A., Doelman, D., Fogarty, K., Galicher, R., Guyon, O., Haffert, S. Y., Huby, E., Jewell, J., Keller, C. U., Kenworthy, M. A., Knight, J., Khn, J., Miller, K. L., Mazoyer, J., N'Diaye, M., Por, E. H., Pueyo, L., Riggs, A. J. E., Ruane, G., Sirbu, D., Snik, F., Wallace, J. K., Wilby, M. J., & Ygouf, M. 2018, in Proc. SPIE 10703-67, Adaptive Optics Systems VI (to be published)

Jovanovic, N., Guyon, O., Lozi, J., Currie, T., Hagelberg, J., Norris, B., Singh, G., Pathak, P., Doughty, D., Goebel, S., Males, J., Kuhn, J., Serabyn, E., Tuthill, P., Schworer, G., Martinache, F., Kudo, T., Kawahara, H., Kotani, T., Ireland, M., Feger, T., Rains, A.,

Bento, J., Schwab, C., Coutts, D., Cvetojevic, N., Gross, S., Arriola, A., Lagadec, T., Kasdin, J., Groff, T., Mazin, B., Minowa, Y., Takato, N., Tamura, M., Takami, H., & Hayashi, M. 2016, in Proc. SPIE, Vol. 9909, Adaptive Optics Systems V, 99090W

Jovanovic, N., Guyon, O., Martinache, F., Clergeon, C., Singh, G., Vievard, S., Kudo, T., Garrel, V., Norris, B., Tuthill, P., Stewart, P., Huby, E., Perrin, G., & Lacour, S. 2013, in Proceedings of the Third AO4ELT Conference, ed. S. Esposito & L. Fini, 94

Jovanovic, N., Guyon, O., Martinache, F., Pathak, P., Hagelberg, J., & Kudo, T. 2015a, ApJ, 813, L24

Jovanovic, N., Martinache, F., Guyon, O., Clergeon, C., Singh, G., Kudo, T., Garrel, V., Newman, K., Doughty, D., Lozi, J., Males, J., Minowa, Y., Hayano, Y., Takato, N., Morino, J., Kuhn, J., Serabyn, E., Norris, B., Tuthill, P., Schworer, G., Stewart, P., Close, L., Huby, E., Perrin, G., Lacour, S., Gauchet, L., Vievard, S., Murakami, N., Oshiyama, F., Baba, N., Matsuo, T., Nishikawa, J., Tamura, M., Lai, O., Marchis, F., Duchene, G., Kotani, T., & Woillez, J. 2015b, Publications of the Astronomical Society of the Pacific, 127, 890

Kühn, J., Serabyn, E., Lozi, J., Jovanovic, N., Currie, T., Guyon, O., Kudo, T., Martinache, F., Liewer, K., Singh, G., Tamura, M., Mawet, D., Hagelberg, J., & Defrere, D. 2018, Publications of the Astronomical Society of the Pacific, 130, 035001

Lafrenière, D., Marois, C., Doyon, R., Nadeau, D., & Artigau, É. 2007, ApJ, 660, 770

Lozi, J., Guyon, O., Jovanovic, N., Singh, G., Goebel, S., Norris, B., & Okita, H. 2016, in Adaptive Optics Systems V, Vol. 9909, 99090J

Macintosh, B., Poyneer, L., Sivaramakrishnan, A., & Marois, C. 2005, in Astronomical Adaptive Optics Systems and Applications II, Vol. 5903, 170–177

Marois, C., Lafrenière, D., Doyon, R., Macintosh, B., & Nadeau, D. 2006, ApJ, 641, 556

Martinache, F., Guyon, O., Jovanovic, N., Clergeon, C., Singh, G., Kudo, T., Currie, T., Thalmann, C., McElwain, M., & Tamura, M. 2014, Publications of the Astronomical Society of the Pacific, 126, 565

Miller, K., Guyon, O., & Males, J. 2017, Journal of Astronomical Telescopes, Instruments, and Systems, 3, 049002

Milli, J., Banas, T., Mouillet, D., Mawet, D., Girard, J. H., Vigan, A., Boccaletti, A., Kasper, M., Wahhaj, Z., Lagrange, A. M., Beuzit, J. L., Fusco, T., Sauvage, J. F., & Galicher, R. 2016, in Adaptive Optics Systems V, Vol. 9909, 99094Z

Minowa, Y., Hayano, Y., Oya, S., Watanabe, M., Hattori, M., Guyon, O., Egner, S., Saito, Y., Ito, M., Takami, H., Garrel, V., Colley, S., Golota, T., & Iye, M. 2010, in Society of Photo-Optical Instrumentation Engineers (SPIE) Conference Series, Vol. 7736, Society of Photo-Optical Instrumentation Engineers (SPIE) Conference Series, 3

Norris, B., Schworer, G., Tuthill, P., Jovanovic, N., Guyon, O., Stewart, P., & Martinache, F. 2015, MNRAS, 447, 2894

Pearson, K. 1895, Proceedings of the Royal Society of London Series I, 58, 240

Racine, R., Walker, G. A. H., Nadeau, D., Doyon, R., & Marois, C. 1999, Publications of the Astronomical Society of the Pacific, 111, 587

Sauvage, J. F., Mugnier, L., Paul, B., & Villecroze, R. 2012, Optics Letters, 37, 4808

Serabyn, E., Wallace, J. K., & Mawet, D. 2011, Appl. Opt., 50, 5453

Smith, W. H. 1987, PASP, 99, 1344

Soummer, R., Pueyo, L., & Larkin, J. 2012, ApJ, 755, L28

Stangalini, M., Pedichini, F., Pinna, E., Christou, J., Hill, J., Puglisi, A., Bailey, V., Centrone, M., Del Moro, D., Esposito, S., Fiore, F., Giallongo, E., Hinz, P., & Vaz, A. 2017, Journal of Astronomical Telescopes, Instruments, and Systems, 3, 025001

Strehl, K. 1902, Astronomische Nachrichten, 158, 89

Vernin, J., Weigelt, G., Caccia, J. L., & Müller, M. 1991, A&A, 243, 553

Chapter 5

SCExAO/CHARIS Near-IR High-Contrast Imaging and Integral Field Spectroscopy of the HIP 79977 Debris Disk

Note: this chapter has been submitted to AJ with co-authors Thayne Currie, Olivier Guyon, Timothy D. Brandt, Tyler D. Groff, Nemanja Jovanovic, N. Jeremy Kasdin, Julien Lozi, Klaus Hodapp, Frantz Martinache, Carol Grady, Masa Hayashi, Jungmi Kwon, Michael W. McElwain, Yi Yang, and Motohide Tamura. A formal reference and DOI for this paper is not yet available.

Abstract

We present new, near-infrared (1.1–2.4 μm) high-contrast imaging of the bright debris disk surrounding HIP 79977 with the Subaru Coronagraphic Extreme Adaptive Optics system (SCExAO) coupled with the CHARIS integral field spectrograph. SCExAO/CHARIS resolves the disk down to smaller angular separations of ($0\farcs11$; $r \sim 14$ au) and at a higher significance than previously achieved at the same wavelengths. The disk exhibits a marginally significant east-west brightness asymmetry in H band that requires confirmation. Geometrical modeling suggests a nearly edge-on disk viewed at a position angle of $\sim 114.6°$ east of north. The disk is best-fit by scattered-light models assuming strongly forward-scattering grains ($g \sim 0.5$–0.65) confined to a torus with a peak density at $r_0 \sim 53$–75 au.

We find that a shallow outer density power law of α_{out} =-1– -3 and flare index of $\beta = 1$ are preferred. Other disk parameters (e.g. inner density power law and vertical scale height) are more poorly constrained. The disk has a grey to slightly blue intrinsic color and its profile is broadly consistent with predictions from birth ring models applied to other debris disks. While HIP 79977's disk appears to be more strongly forward-scattering than most resolved disks surrounding 5–30 Myr-old stars, this difference may be due to observational biases favoring forward-scattering models for inclined disks vs. lower inclination, ostensibly neutral-scattering disks like HR 4796A's. Deeper, higher signal-to-noise SCExAO/CHARIS data can better constrain the disk's dust composition.

5.1 Introduction

Debris disks around young stars are signposts of massive planets (e.g. Marois et al. 2008; Lagrange et al. 2010) and critical reference points for understanding the structure, chemistry, and evolution of the Kuiper belt (Wyatt 2008). Debris disks may be made visible by recently-formed icy Pluto-sized objects stirring and causing collisions between surrounding boulder-sized icy planetesimals. The luminosity distribution of debris disks over a range of ages then traces the evolution of debris produced by icy planet formation. (Currie et al. 2008; Kenyon & Bromley 2008)). Similarly, massive jovian planets may create gaps in some of these debris disks and sculpt the distribution of their icy planetesimals (Mustill & Wyatt 2009).

Resolved imaging of debris disks in scattered light has revealed dust sculpted in morphologies ranging from diffuse structures or extended torii to sharp rings; disks exhibited scattering properties ranging from neutral to strongly forward scattering (e.g. Smith & Terrile 1984; Schneider et al. 1999, 2005, 2009; Kalas et al. 2005, 2006, 2007a; Soummer et al. 2014; Currie et al. 2015, 2017b). Furthermore, multi-wavelength imaging and spectroscopy of debris disks in scattered light provide further insights into the nature of debris disk properties. The differing grain properties of debris disks can result in a spread in intrinsic

disk colors from blue (e.g. HD 15115, Kalas et al. 2007b), where dust is reflecting light more efficiently at shorter wavelengths compared to what it receives from the star, to red (e.g. β Pic, Golimowski et al. 2006). Detailed photometric color characterization provides insights into grain properties, and low-resolution spectroscopy (even as low as R $\sim$ 10) probes the presence of ices and organics (e.g. Debes et al. 2008; Rodigas et al. 2014; Currie et al. 2015).

Extreme adaptive optics (ExAO) systems coupled with integral field spectrographs improve the ability to detect and characterize debris disks, especially at small angles. For example, resolved imaging and spectroscopy of the HD 115600 debris disk with the *Gemini Planet Imager*, the first object discovered with ExAO, revealed a sharp ring at $r \lesssim 0\farcs5$, modeling for which suggested neutral-scattering and possibly icy dust and a pericenter offset caused by a hidden jovian planet (Currie et al. 2015). Milli et al. (2017) resolved the well-known HR 4796A disk at far smaller angular separations than done previously. They showed that a seemingly neutral-scattering dust ring has a strong forward-scattering peak at small angles, inconsistent with a single Henyey-Greenstein-like scattering function. Resolved imaging and spectroscopy over a longer wavelength baseline enables better constraints on the properties of other debris disks (e.g. Rodigas et al. 2015; Milli et al. 2017).

HIP 79977 is another young star whose debris disk can better understood using multi-wavelength imaging and spectroscopy with ExAO. This is an F2/3V star (1.5 $M_\odot$) located 131.5 $\pm$ 0.9 pc away (Gaia Collaboration 2018) in the $\sim$ 10 Myr-old Upper Scorpius association (Pecaut et al. 2012). Its infrared excess was detected by the *IRAS* satellite, and the Spitzer Multiband Imaging Photometer associated it with a debris disk (Chen et al. 2011). Thalmann et al. (2013) used Subaru's facility (conventional) AO188 adaptive optics system and the HiCIAO instrument at H band and produced the first resolved images of its debris disk. They revealed that it was viewed nearly edge-on ($i = 84^{+2}_{-3}{}^\circ$) and had tangential linear polarization varying from $\sim$ 10% at $0\farcs5$ to $\sim$ 45% at $1\farcs5$. Engler et al. (2017) performed the first ExAO characterization of HIP 79977, observing it at visible wavelengths ($\lambda_c = 735$ nm, $\Delta\lambda = 290$ nm) using the SPHERE-ZIMPOL polarimeter. They measured a polarized flux contrast ratio for the disk of $(F_{\rm pol})_{\rm disk}/F_\star = (5.5 \pm 0.9) \times 10^{-4}$ in

that band and an increase in the thickness of the disk at larger radii, which they explained by the blow-out of small grains by stellar winds.

These previous studies showed tension in some derived debris disk properties (e.g. the disk radius) and allowed a wide range of parameter space for others (e.g. the disk scattering properties). No substellar companions were decisively detected in either publication. However, Thalmann et al. (2013) did find a marginally significant point-like residual emission in their reduced image after subtracting a model of the debris disk's emission.

In this paper, we present the first near-IR resolved ExAO images of the HIP 79977 debris disk, using the Subaru Coronagraphic Extreme Adaptive Optics systems coupled with the CHARIS integral field spectrosgraph. SCExAO/CHARIS data probe inner working angles ($0\farcs15$–$0\farcs2$) comparable to those from SPHERE polarimetry reported in Engler et al. (2017) and significantly smaller than that presented in Thalmann et al. (2013). Additionally, we present the first near-IR color analysis of the disk.

The paper is organized as follows: in Section 5.2, we describe the observations and the pipeline through which the data was reduced and then PSF-subtracted; in Section 5.3, we describe the basic morphology of the disk; then, in Section 5.4.1 we discuss the process through which we generated synthetic disks and propagated them through the same pipeline as the actual data in order to understand how the PSF subtraction attenuated the disk features; we provide the results of this forward modeling in Section 5.4.2; finally, we describe the J-, H-, and K_p-band colors of the disk.

5.2 SCExAO/CHARIS Data

5.2.1 Observations and Data Reduction

We targeted HIP 79977 on UT 14 August 2017 (Program ID S17B-093, PI T. Currie) with Subaru Telescope's SCExAO (Jovanovic et al. 2015b) instrument coupled to the CHARIS integral field spectrograph, which operated in low-resolution ($R \sim 20$), broadband (1.13–

2.39 μm) mode (Peters et al. 2012; Groff et al. 2013). SCExAO/CHARIS data were obtained using the Lyot coronagraph with the 217 mas diameter occulting spot. Satellite spots, attenuated copies of the stellar PSF, were generated by placing a checkerboard pattern on the deformable mirror with a 50 nm amplitude and alternating its phase between 0° and 180° (Jovanovic et al. 2015a). These spots were used for image registration and spectrophotometric calibration; their intensity relative to the star[1] was given by

$$I_{spots}/I_{\star} = 4 \times 10^{-3}(\lambda/1.55\ \mu\mathrm{m})^{-2}. \tag{5.1}$$

Exposures consisted of 86 co-added 60 s frames (82 science frames, 4 sky frames) obtained over 92 minutes and covering a total parallactic angle rotation of 26.7°. Conditions were excellent; seeing was 0.″35-0.″40 at 0.5 μm and the wind speed was 3 m s^{-1}. Although we did not obtain a real-time estimate of the Strehl ratio, the raw contrasts at $r \sim 0.''2$–$0.''75$ later estimated from spectrophotometrically calibrated data were characteristic of those obtained with H-band Strehls of 70–80% (Currie et al. 2018).

To convert raw CHARIS files into data cubes, we employed the CHARIS Data Reduction Pipeline (CHARIS DRP, Brandt et al. 2017). After generating a wavelength solution from monochromatic ($\lambda_0 = 1.550$ μm) lenslet flats, the pipeline extracted data cubes using the least squares method described by Brandt et al. (2017), yielding a nominal spaxel scale of 0.″0164 and $\sim 1.''05$ radius field of view. Subsequent processing steps – e.g. image registration and spectrophotoemtric calibration – followed those from Currie et al. (2018).

For PSF subtraction, we utilized the KLIP algorithm (Soummer et al. 2012) in ADI-only mode as employed in Currie et al. (2014, 2017a), where PSF subtraction is performed in annular regions with a rotation gap to limit signal loss from self-subtraction of astrophysical sources. Key algorithm parameters – the width of annulus over which PSF subtraction is performed (Δr), the rotation gap (δ), the number of principal components (N_{pc}) – were varied to explore which combination maximized the total SNR of the disk in sequence-

[1]The spot intensity calibration changed following the observations described in this paper, so this equation may not match what is provided elsewhere.

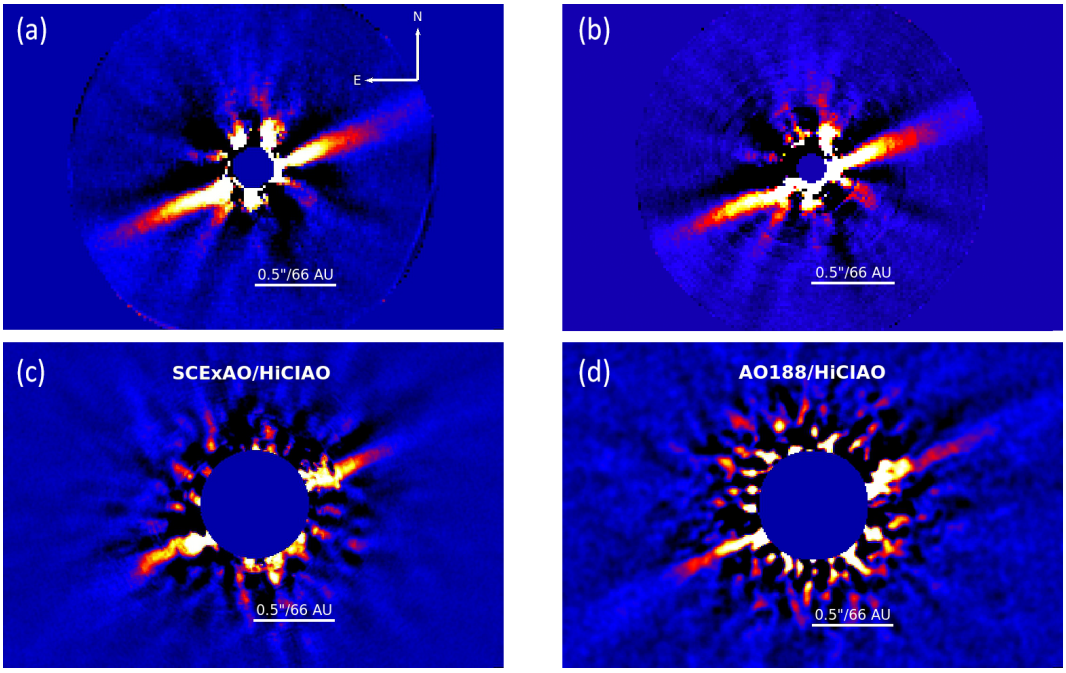

Figure 5.1 Illustrated here are the three different NIR datasets for HIP 79977. The upper panels (a and b) are our paper's main focus and show wavelength-collapsed images produced by two different KLIP-ADI reductions of the SCExAO/CHARIS data. Figure 5.1c shows July 2016 H band data from SCExAO + HiCIAO reduced using A-LOCI with local masking (Currie et al. 2012) and has stronger residuals exterior to 0.″3–0.″4. Finally, Figure 5.1d shows the data published by Thalmann et al. (2013), which were produced using the (non-extreme) AO188 and HiCIAO at H band. The data were processed using the ACORNS-ADI reduction package (Brandt et al. 2013). The four images have the same intensity scaling. The circular region in the bottom two plots denotes the field of view of the CHARIS data.

combined, wavelength-collapsed images. While the detection of the HIP 79977 debris disk was robust across the entire range of parameter space, the signal to noise of the spine of the disk was maximized with a setting with Δr = 2 pixels, $N_{\rm pc} = 2$, and $\delta = 1.0$ full width half maxima (FWHM) and then merging the wavelength channels using a robust mean with outlier rejection instead of a median combination. As described later, for computational efficiency and simplicity, we performed a second reduction with a larger annular width of Δr = 6 pixels ($\sim 2.5\lambda$/D at 1.55 μm). Reductions retaining a slightly different number of principal components or value for the rotation gap yielded comparable results.

5.2.2 Detection of the HIP 79977 Debris Disk

Figures 5.1a and 5.1b show the results of these two reductions of the CHARIS data. Figures 5.1c and 5.1d contextualize the performance gain of SCExAO/CHARIS compared to earlier observations. The disk is plainly visible down to an inner working angle of 0.″11 in 5.1a and 5.1b. Figure 5.1c shows data collected on UT 17 July 2016 (Program UH-12B, PI K. Hodapp) using SCExAO (suboptimally tuned and providing lower Strehl than that of the recent data) and the HiCIAO instrument at H band. Although the July 2016 SCExAO/HiCIAO image has a larger field of view than the SCExAO/CHARIS image, it exhibits far stronger residuals interior to about 0.″3–0.″5. Figure 5.1d shows the AO188 (Subaru's facility AO system, Minowa et al. 2010) + HiCIAO data previously published by Thalmann et al. (2013), and this has even stronger residuals, particularly at smaller angular separations, due to its much poorer AO correction.

Figure 5.2 shows the sequence-combined, wavelength-collapsed disk image scaled by the stellocentric distance squared, and analogous images obtained from combining channels covering the J (channels 1–5; 1.16–1.33 μm), H (channels 8–14; 1.47–1.80 μm), and K_p (channels 16–21; 1.93–2.29μm) passbands. This image used the first set of KLIP parameters described above. The disk is plainly visible in each image. We computed the signal-to-noise per resolution element using the standard practice of replacing each pixel with the sum within a FWHM-sized aperture, computing the radial profile of the robust standard deviation of this summed image in the wavelength-collapsed image, dividing the two images, and correcting for small sample statistics (Currie et al. 2011). The disk is detected at a SNR/resolution element (SNRE) > 3 exterior to 0.″25 and peaks at SNRE $\sim$ 9.1, 8, 9.1, and 5.8 in the broadband, J, H, and K_p images, respectively[2]. These estimates are conservative as we do not mask the disk signal when computing the noise profile. For our second reduction the SNRE values along the disk spine are slightly smaller at small angles

[2]We achieved comparable results using a different algorithm, A-LOCI, using local masking as implemented in Currie et al. (2012, 2017b).

but otherwise comparable, peaking at 9.6, 9, 8.4, and 5.6 in the broadband, J, H, and K_p images, respectively.

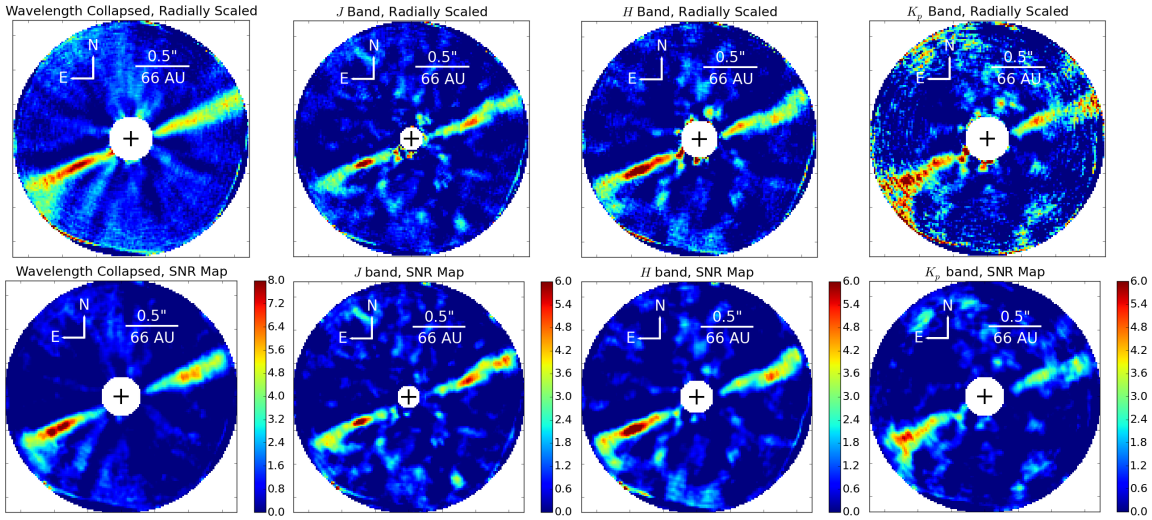

Figure 5.2 Shown here are flux images following KLIP PSF-subtraction (top) and the corresponding signal-to-noise per resolution element maps (bottom). The CHARIS low-resolution mode produces data cubes with 22 spectral layers. We coadded all the layers (left) and the bands corresponding to (proceeding rightward) J, H, and K_p bands. The flux images have arbitrary units and have been multiplied by an r^2 map in order to reveal structure away from the star. The images presented here are rotated relative to those in Figure 5.1.

For both reductions, the final images and SNR maps may reveal some evidence for a wavelength dependent brightness asymmetry between the eastern and western sides. In the wavelength-collapsed image, the eastern side of the disk appears about 50% brighter and is detected at a higher significance ($\sim 8-9\ \sigma$ vs. $5.5-6.5\ \sigma$ along the disk spine beyond $0\farcs5$). From comparing images obtained over different passbands, H and K_p band seem to be responsible for most of this brightness asymmetry.

5.3 Geometry of the HIP 79977 Debris Disk

Our images clearly trace the major axis of the HIP 79977 debris disk. To estimate the disk's position angle, we follow previous analysis performed for HD 36546 (Currie et al. 2017b) and for β Pic (Lagrange et al. 2012), determining the trace of the disk spine from

the peak brightness as a function of separation ("maximum spine" fitting) and from fitting a Lorentzian profile. Our procedure used the *mpfitellipse* package to estimate the disk spine from disk regions between $0\farcs15$ and $0\farcs75$, where the pixels are weighted by their SNRE, and explored a range of thresholds in SNRE (0–3) to define the spine.

Precise astrometric calibration for CHARIS is ongoing and preliminary results will be described in full in a separate early-science paper focused on κ Andromedae b (Currie et al. 2018, in prep.). Briefly, we obtained near-infrared data for HD 1160 from SCExAO/CHARIS in September 2017 and Keck/NIRC2 in December 2017. At a projected separation of $r \sim 80$ au, the low-mass companion HD 1160 B should not experience significant orbital motion (Nielsen et al. 2012; Garcia et al. 2017); Keck/NIRC2 is precisely calibrated, with a north position angle uncertainty of 0.02^o and post-distortion corrected astrometric uncertainty of 0.5 mas (Service et al. 2016). Thus, we pinned the SCExAO/CHARIS astrometry for HD 1160 B to that for Keck/NIRC2 to calibrate CHARIS's pixel scale and north position angle offset. These steps yielded a north PA offset of $\sim -2.2°$ east of north and a revised pixel scale of $\sim 0\farcs0162$. While the differences between the default and revised pixel scale lead to astrometric offsets are inconsequential for this paper (10 mas near the edge of CHARIS's field of view), the north position angle (PA) offset for CHARIS is necessary for an accurate estimate of the position angle for the disk's major axis.

After considering CHARIS's north PA offset, Lorentzian profile fitting yields a position angle of $114.59° \pm 0.40°$. "Maximum spine" fitting yields nearly identical results but with larger error bars: $114.74° \pm 1.88°$. These values are consistent with previous estimates from Engler et al. (2017) and Thalmann et al. (2013). For the rest of the paper, we adopt a position angle of 114.6°.

5.4 Modeling of the HIP 79977 Debris Disk

5.4.1 Methodology

Forward-Modeling of the Annealed Disk Due to PSF Subtraction

To assess the morphology of the HIP 79977 debris disk, we forward-modeled synthetic disk images spanning a range of properties through empty data cubes, using the same eigenvalues and eigenvectors used in the reduction of our on-sky data (e.g. Soummer et al. 2012; Pueyo 2016). Our specific implementation, following the formalism in Pueyo (2016), is described and justified in detail below.

The residual signal of a planet or disk in a target image with spatial dimensions x and an intrinsic signal $\mathbf{A(x)}$ after KLIP processing is nominally equal to the astrophysical signal in the target image minus its projection on the KLIP basis set constructed from references images from up to k = $1 \cdots K_{\mathrm{klip}}$ principal components, Z_k:

$$P_{\mathrm{residual,n}} = A(x_n) - \Big(\sum_{k=1}^{K_{\mathrm{klip}}} < A(x_n), Z_k^{KL} > Z_k^{KL}(n) \Big) \tag{5.2}$$

Here, ${\mathbf{Z}_k}^{KL}$ is the Karhunen-Loeve transform of the reference image library $\mathbf{R}$ with eigenvalues Λ_k and eigenvectors ν_k:

$$Z_k^{KL}(x) = \frac{1}{\sqrt{\Lambda_k}} \sum_{m=1}^{K_{\mathrm{klip}}} \nu_k R_m(x). \tag{5.3}$$

When the astrophysical signal in a given image is not contained in reference images used for subtraction, then annealing is entirely due to *oversubtraction*: confusion of the astrophysical signal with speckles. As described in Pueyo (2016), however, the presence of an astrophysical signal in the reference image library itself causes *self-subtraction* of the source in the target image and perturbs ${\mathbf{Z}_k}^{KL}$.

In performing forward-modeling, we consider both oversubtraction and direct self-subtraction. Pueyo (2016) delineate regimes where oversubtraction and two different

regimes of self-subtraction (direct and indirect) dominate. For small $K_{\rm klip}$ values and an astrophysical signal is small compared to the speckles over the region where principal component analysis is performed, oversubtraction dominates and a straightforward application of Equation 2 describes annealing. For intermediate $K_{\rm klip}$ values, *direct self-subtraction* dominates, scaling linearly with the astrophysical signal and inversely with the square-root of the unperturbed eigenvalues: $\epsilon/\sqrt{\Lambda_k}$. For large $K_{\rm klip}$, closer to a full-rank covariance matrix, *indirect self-subtraction* dominates and is inversely proportional to the eigenvalues: ϵ/Λ_k. Other algorithm settings (e.g. using a larger rotation gap) can remove more astrophysical signal from the reference library, reducing the influence of self-subtraction.

These arguments and previous measurements of the HIP 79977 disk help identify the important biases/sources of annealing for our HIP 79977 data set. In our reductions, the number of removed KL modes is small compared to the size of the reference library ($\rm K_{klip} \ll N_{images/channel}$). In most channels, the disk is $\approx 5\%$ of the brightness of the local speckles. Furthermore, we perform PSF subtraction in annular regions. Over the angular separations modeled ($0\farcs16$–$0\farcs75$), results from Engler et al. (2017, see their Fig. 6b) imply that the nearly edge-on disk is present in no more than 10–20% of the pixels at each angular separation. Our rotation gap criterion (1 PSF footprint) further reduces self-subtraction. As a result, the perturbed KL modes ΔKL are far smaller than the unperturbed ones dominated by signal from the speckles: the indirect self-subtraction term is negligible. Thus, in performing forward-modeling we consider oversubtraction (the dominant contribution) and direct self-subtraction (a secondary contribution) only.

Scattered Light Disk Models

Synthetic scattered light disk models were drawn from the GRaTeR code developed in Augereau et al. (1999), convolved with the SCExAO/CHARIS instrumental PSF, and inserted into empty data cubes with the same position angles as the real data. We then forward-modeled the annealing of each model disk due to KLIP PSF subtraction as described

above and compared the wavelength-collapsed image of the residual disk model to the real data. The fidelity of each model disk to the data is determined in the subtraction residuals in binned (by the instrument PSF size) pixels ($\sim 0\farcs04$) over a region of interest defining the trace of the disk and any self-subtraction footprints (see Figure 5.3). This evaluation region encloses 237 binned pixels (N_{data}).

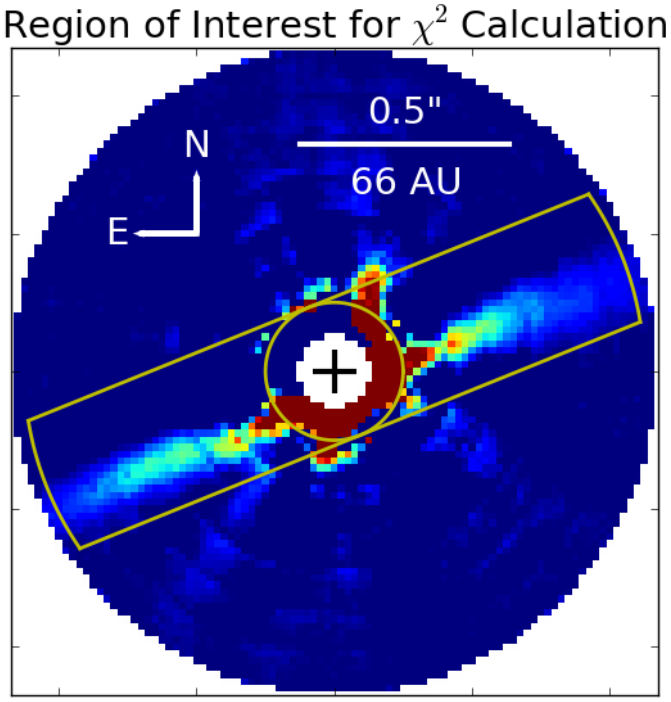

Figure 5.3 The region bounded by the yellow lines was used for scaling the PSF-subtracted synthetic model disks and then computing their χ^2 residuals relative to the on-sky data. The outer boundary is defined by the intersection of a rectangular box that is 100 pixels by 20 pixels where the major axis is rotated 22° north of west and a circle of radius $r = 45$ pixels. The inner region is a circle of radius $r = 10$ pixels. The disk in this figure is plotted from the same data as that used in Figure 5.2, but it has not been multiplied by an r^2 map.

The set of acceptably-fitting solutions have chi-squared values of $\chi^2 \leq \chi^2_{\rm min} + \sqrt{2N_{\rm data}}$ (see Thalmann et al. 2013). At the 95% confidence limit, this criterion equals $\chi^2_\nu \lesssim 1.092$.

Because we performed KLIP PSF subtraction in annuli (not the entire field at once) and in 22 wavelength channels (not single-channel camera data), exploring 10^6 models covering a large parameter space as in Engler et al. (2017) would be extremely computationally expensive. Rather, we leverage on inspection of the SCExAO/CHARIS wavelength-

collapsed final image, our disk geometry modeling, and previous results from Engler et al. (2017) to focus on a smaller parameter space range.

Inspection of the final CHARIS image shows that the disk is detected only on the near side, out to an angular separation of 0.″5–0.″6 before gradually fading in brightness at wider separations. Our fitting to the geometry of the disk reaffirms a position angle of 114.6^o. Thus, our parameter space generally explores disks with moderate to strong forward-scattering, a sharp inner cutoff to the belt, and a shallower decay in dust density beyond the fiducial radius.

We varied six parameters in our search for the disk that best reproduced the on-sky data. First, the Henyey-Greenstein parameter (Henyey & Greenstein 1941) probes the visible extent of the dust's phase scattering function. While it lacks a pure physical motivation and is known to fail at very small scattering angles for at least some debris disks (Milli et al. 2017)[3], it is widely adopted in debris disk modeling literature and thus helps cast our results within the context established by other debris disks. The H-G parameter ranges from -1 to 1; $g = 0$ corresponds to neutral scattering, $g = -1$ indicates perfect backward scattering, and $g = 1$ indicates dust that scatters light solely forward.

Second, we varied values of the fiducial radius r_0 of the disk, inside of which α_{in} ($\alpha_{in} > 0$) describes the power law for the increase in dust particle number density and outside of which α_{out} ($\alpha_{out} < 0$) describes the power law for its decrease. These three variables, which were the second through fourth fitted parameters, combine to give the radial distribution profile $R(r)$:

$$R(r) = \left[\left(\frac{r}{r_0} \right)^{-2\alpha_{in}} + \left(\frac{r}{r_0} \right)^{-2\alpha_{out}} \right]^{-1/2} \tag{5.4}$$

where r is the distance from the center of the disk. The vertical profile $Z(h)$ is given by

$$Z(h) = \exp\left(\frac{-|h|}{H(r)} \right), \tag{5.5}$$

[3]These angles correspond to the semimajor axis of the HIP 79977 debris disk and are inaccessible with our data.

where h is the distance above the disk midplane. $H(r)$ is the scale height at radius r and is given by

$$H(r) = \xi \left(\frac{r}{r_0} \right)^{\beta}, \tag{5.6}$$

where ξ is the scale height at r_0 and β is the disk's flare index. ξ and β were the fifth and sixth parameters in our grid search.

We tested models with $g = 0.3 - 0.8$, corresponding to moderate to strong forward scattering. Based on visual estimates of the disk images, we produced model disks with fiducial radii of $r_0 = 43 - 91$ au. The parameters α_{in} and α_{out} determine the power laws for the inner and outer radial emission profiles, respectively, and we selected values that produced disks with relatively sharp inner cutoffs and slow radial decays. We sampled disks with a scale height at the fiducial radius in the range of $\xi = 0.5 - 3.2$ au; values outside this range would not be consistent with the self-subtracted images. We adopt our value for the disk position angle determined in Section 5.3. and used our available computing resources to probe a greater variety of the other parameters. Values outside these parameter ranges produced synthetic disks whose morphology differed greatly from the on-sky results. The left two columns of Table 5.1 list each parameter and the associated range in parameter space explored. Our nominal search considered only circular disks and consisted of 20,480 models.

Table 5.1. The grid of synthetic model disks used in our forward modeling.

Parameter	Values tested	Value for best model	Acceptably-fitting values
Radius of belt r_0 (au)	[43, 53, 64, 69, 75, 80, 86, 91]	53	[53, 64, 69, 75]
Inner radial index α_{in}	[3, 4, 5, 6]	6	[3, 4, 5, 6]
Outer radial index α_{out}	[-1, -1.5, -2, -2.5, -3, -3.5, -4.5, -5.5]	-1.5	[-1, -1.5, -2, -2.5, -3]
Vertical scale height ξ (au)	[0.5, 1.1, 1.6, 2.1, 3.2]	3.2	[0.5, 1.1, 1.6, 2.1, 3.2]
Flare index β	[1, 2]	1	[1, 2]
H-G parameter g_{sca}	[0.3, 0.4, 0.5, 0.55, 0.6, 0.65, 0.7, 0.8]	0.6	[0.5, 0.55, 0.6, 0.65]

Note. — We assumed inclination $i = 84.5°$, eccentricity $e = 0$, and position angle $\theta = 114.6°$. ξ and r_0 are not round numbers because they were initially chosen based on the distance to HIP 79977 provided by van Leeuwen (2007), which was refined by Gaia Collaboration (2018), causing the scale to change by $\sim 7\%$. If one value of a parameter fell below the acceptably-fitting χ^2_ν threshold for at least one model, it was included here. Figure 5.6 shows which parameters values most frequently produced acceptably-fitting models.

5.4.2 Results

Of the 20,480 synthetic disks, 132 produced residuals of $\chi^2_\nu \lesssim 1.092$ and therefore were acceptably fitting. The best model, which we defined as the model yielding the smallest χ^2_ν, produced $\chi^2_\nu = 1.000$. The three panels of Figure 5.4 show the best-fitting synthetic disk before and after PSF subtraction and the resulting residuals after it was subtracted from the on-sky data. This disk model had $g = 0.6$, indicating moderately strong forward scattering, a fiducial radius of $r = 53$ au, a flare index of $\beta = 1$, a disk scale height at the fiducial radius of $\xi = 3.2$ au, and dust emission with an inner power law of $\alpha_{in} = 6$ and outer power law of $\alpha_{out} = -1.5$.

The range of parameters covered by the acceptably-fitting models is summarized in the fourth column of Table 5.1. We produced contour maps of the average fit quality for every value of every parameter against every value of every other parameter. An example map, showing the average χ^2_ν for each value of r_0 and g averaged across the other parameters, is shown in Figure 5.5. These maps helped us ensure that we were sampling a reasonable range of values for each parameter. Additionally, histograms of the parameter values that produced these acceptably-fitting models are shown in Figure 5.6.

Our modeling yielded improved constraints on the disk's radius and its scattering properties. As shown in Figure 5.5, there is a clear minimum in χ^2_ν around $g \approx 0.55$ and $r_0 \approx 70$ au. As shown in Figure 5.6, the family of acceptably-fitting solutions has a small spread around these values. Our contour plots showed a strong preference for $\beta = 1$, indicating that the disk has low flaring.

On the other hand, the acceptably-fitting models covered the full range of considered values of α_{in}, indicating that α_{in} is not further constrained by our model fitting beyond what was done in (Engler et al. 2017). This is likely because there was minimal disk available between the inner working angle and the fiducial radius for the α_{in} fitting to occur.

We find numerically a good match between the wavelength-collapsed image and forward-modeled non-eccentric disk models, which show no brightness asymmetry. However, as evidenced by Figure 5.2, the HIP 79977 disk appears to exhibit asymmetrical brightness.

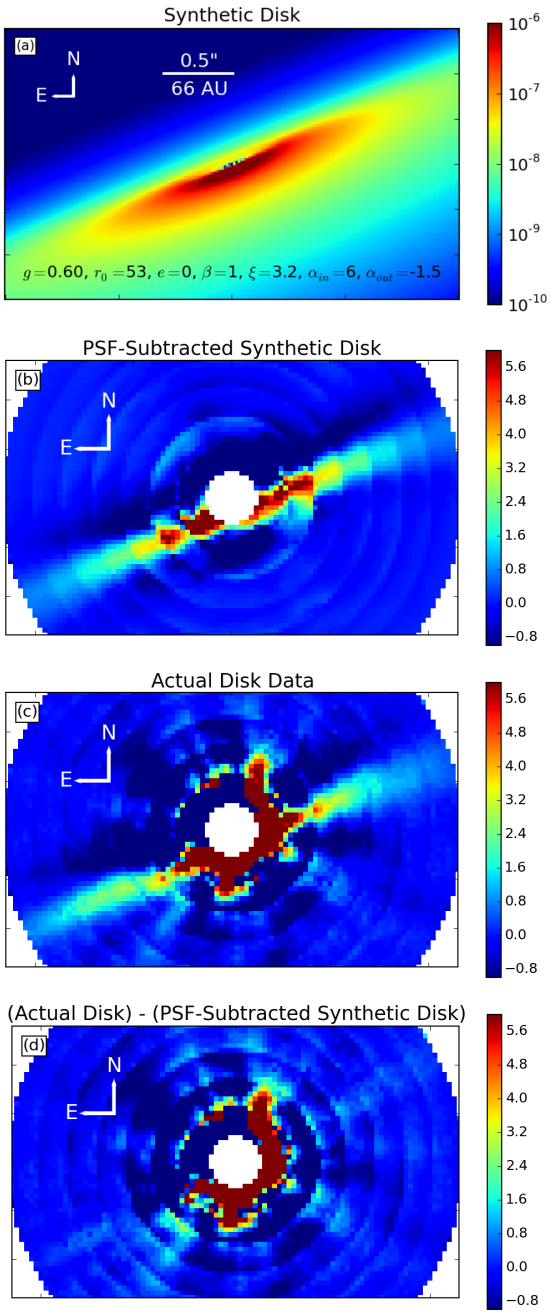

Figure 5.4 From top to bottom are (a) the best-fitting synthetic disk; (b) that disk after it was convolved with the SCExAO PSF and then propagated through the KLIP PSF-subtraction using the same eigenvalues and eigenvectors as the on-sky data; (c) the wavelength-collapsed disk image (same as Figure 5.1b) used in the χ^2 comparison with the synthetic model; and (d) the difference between panels (c) and (b). Minimal structure remains in panel (d), indicating that the synthetic disk closely matches the actual data. The units are arbitrary. The distance scale is the same in all four panels.

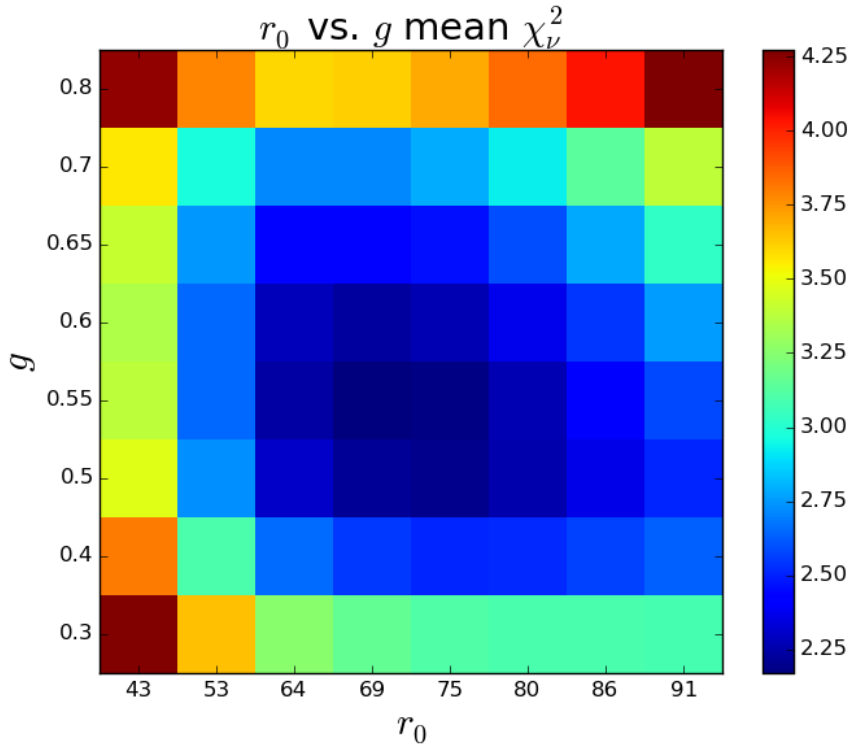

Figure 5.5 Shown here is the mean χ^2_ν for each value of r_0 and g. All values for the other parameters were included in the mean when calculating the value of each pixel. We produced these maps for every variable against every other variable; this map is illustrative of the results. We used these maps to verify that our tested values adequately spanned the parameter space. The region of parameter space minimizing χ^2 is clear and well behaved.

The east side of the disk is clearly brighter than the west side in H band, and less clearly so in others. This brightness asymmetry may also be present in SCExAO/HiCIAO H band data from 2016 (Figure 5.1c). This suggests that it may not be an artifact of the data or processing. Plausible causes of the disk asymmetry are discussed in Section 5.6.

5.5 HIP 79977 Disk Surface Brightness Profile and Colors

Next, we computed the surface brightness profile of the HIP 79977 disk in the J, H, and K_p bands. We began by using the satellite speckles (the PSF core was hidden by a coronagraph, but the flux of the satellite speckles was given by Equation 5.1) and knowledge of the star's spectral type to spectrophotometrically calibrate the data cube. Second, we rotated

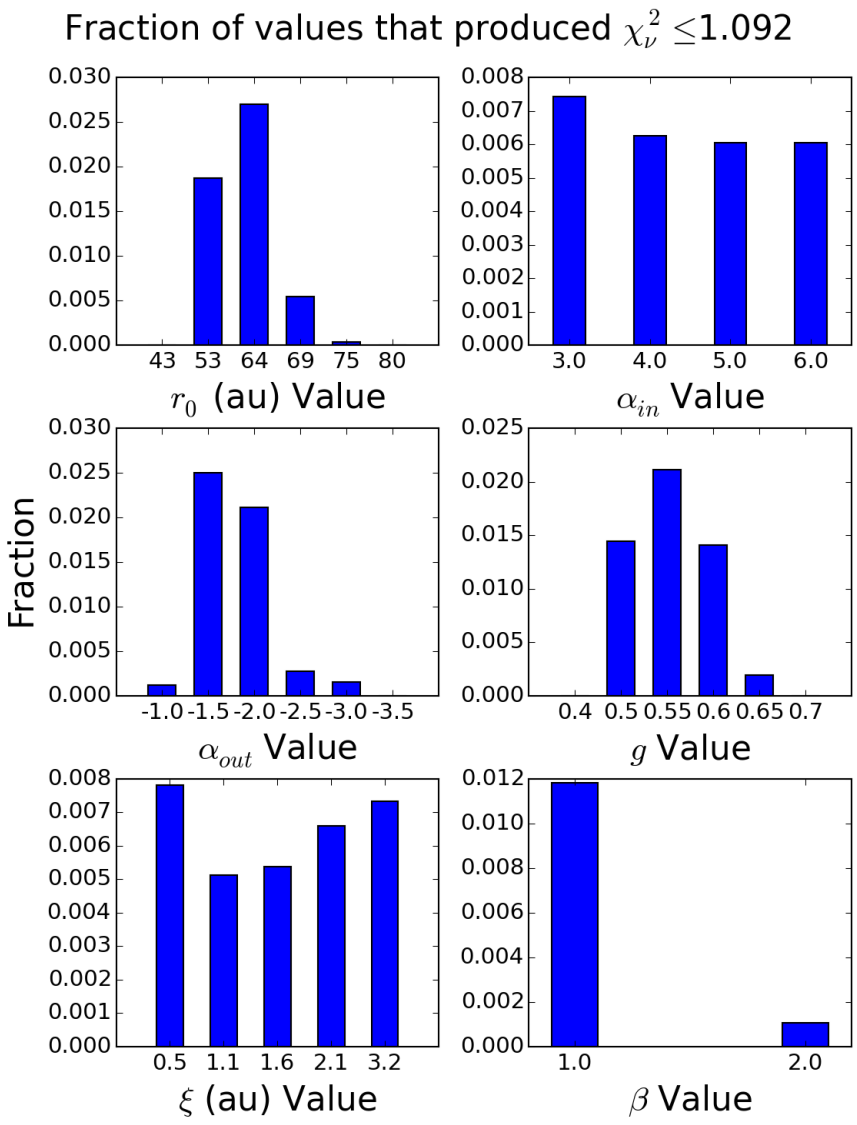

Figure 5.6 Each histogram bin contains the ratio of all models with that parameter value that produced an acceptably fitting χ^2_ν compared to the number of models with that parameter value. The average of the bin heights in each plot is $132/20480 \approx 0.0064$. Some values with zero well-fitting disks have not been plotted in order to improve readability.

the image so that the disk's spine was approximately horizontal and then fitted modified Gaussian functions along the disk in order to find the spine's location with greater precision. We then fit a fourth-order polynomial to these positions in order to smooth them and used this fit as the trace of the disk in the subsequent steps. Next, we merged the appropriate

spectral channels to produce images equivalent to J, H, and K_p bands and calculated a nominal surface brightness in each band along the disk's spine at radial intervals of one PSF footprint. Uncertainties were calculated using the technique described in Section 5.2. We divided the post-PSF-subtraction best-fitting synthetic model disk by the pre-PSF-subtraction version in order to produce a map of the attenuation that occurred during the PSF subtraction. The PSF subtraction attenuated the disk spine by typically $15 - 20\%$, and the attenuation increased with vertical displacement from the disk. Finally, we scaled the nominal surface brightnesses by to the attenuation map.

Figures 5.7 and 5.8 show the surface brightnesses/reflectance on the east and west sides of the disk for the three color bands. The uncertainties decrease significantly at radial separations of $\gtrsim 0\farcs25$. These measurements extend the surface brightness measurements inward from those calculated by Thalmann et al. (2013). The reflectance of the disk is either comparable in all three bands, suggesting a grey color, or is slightly blue. Figure 5.8 clearly shows the excess H band brightness of the east side of the disk compared to that of the west side. This asymmetry appears present at J band at a smaller inner separation and is marginal but plausible at K_p band at a larger separation. The disk's surface brightness radial profile can be well fit with a power law with an exponential decay term of -4.1 ± 0.4.

5.6 Discussion

Our improved signal to noise and inner working angle compared to those of previous work enabled us to better constrain HIP 79977's disk parameters. Our fitted parameters agreed with those derived by Engler et al. (2017) within 1σ except for the fiducial radius, which differs by 1.4σ (this takes into account the different distance they assumed). While our picture of the disk qualitatively agrees with much of that from the discovery paper (Thalmann et al. 2013), we exclude some of the parameter space for dust scattering that

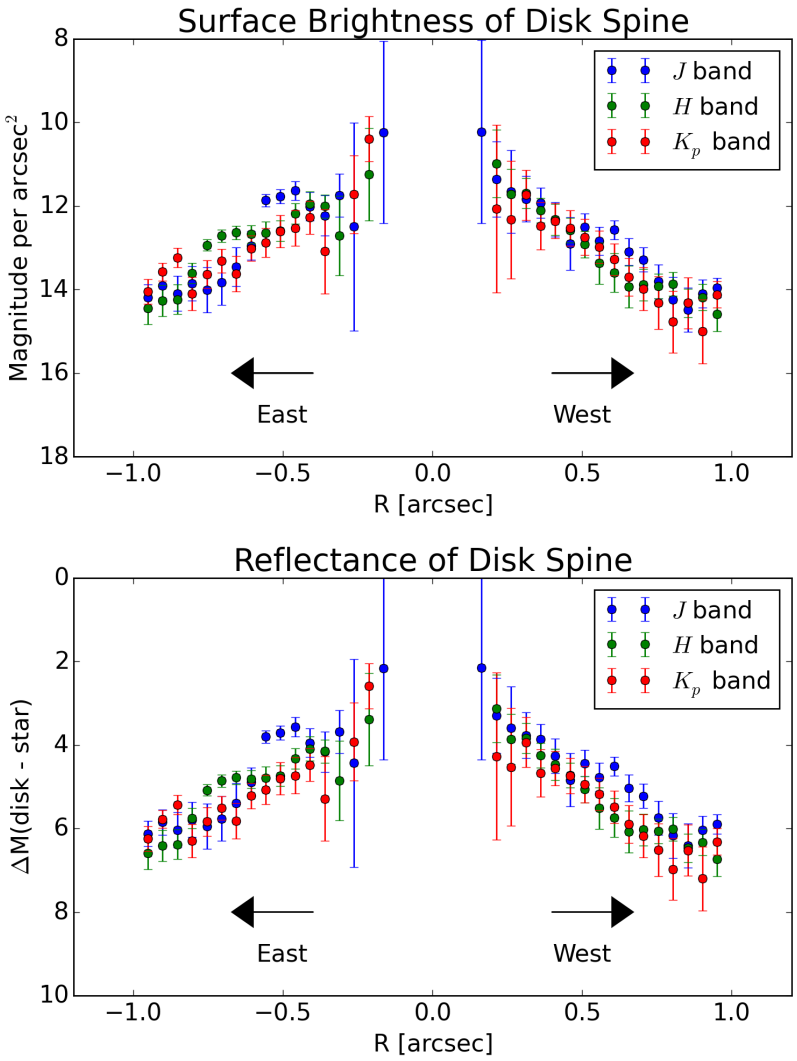

Figure 5.7 The J, H, and K_p band surface brightnesses along the disk spine are shown in the top plot. In the lower plot, we have subtracted the flux of the star ($J = 8.062, H = 7.854, K = 7.800$) in order to see the disk's colors after removal of the stellar color. The disk is largely gray, though slightly blue at some radial separations. The three bands plotted individually are shown in Figure 5.8.

they find (e.g. $g = 0.4$) and find a larger disk radius than they adopted in their paper ($r_0 = 40$ au).

Thalmann et al. (2013) also note a candidate point source-like emission peak located $0\farcs5$ from the star, which appeared after subtracting their best-fit disk model. They posited that, if confirmed, this peak could be a localized clump of debris or thermal emission from

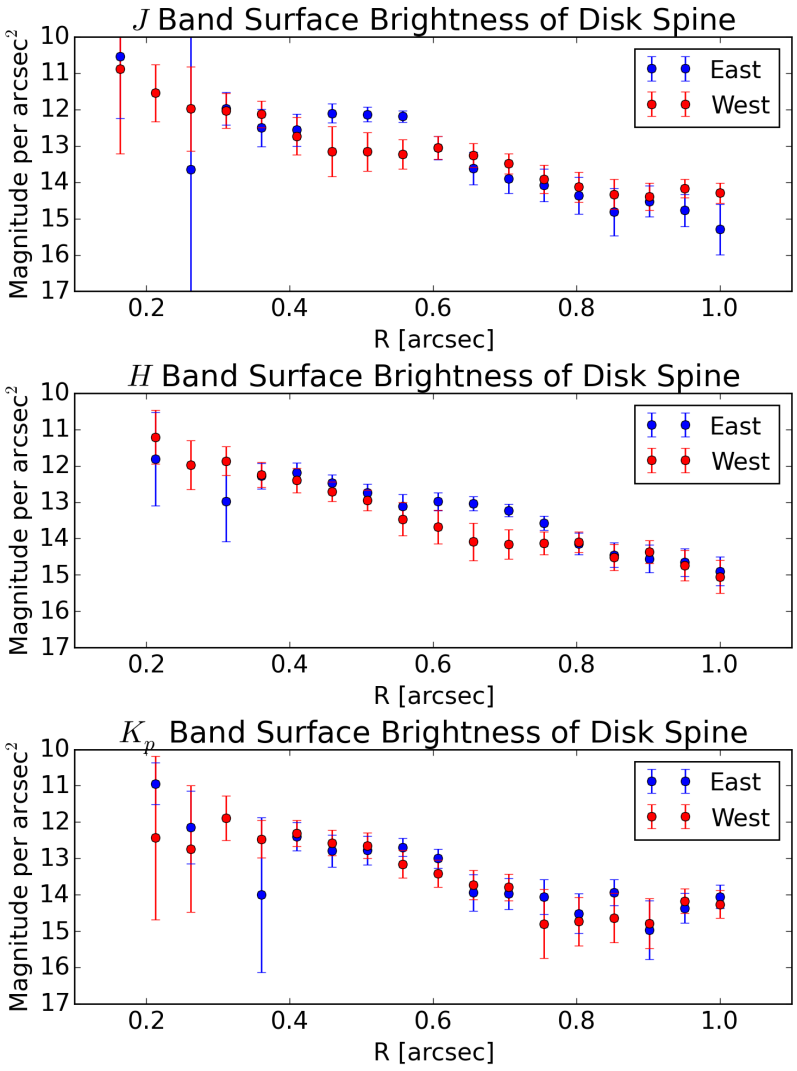

Figure 5.8 From top to bottom are plots of the J, H, and K_p band surface brightnesses of the disk. The brightness asymmetry of the east and west sides of the disk are visible in these plots, albeit at differing separations and significance.

a $3-5M_J$ planet[4]. While our rereduction of the Thalmann et al. data likewise show this emission, it does not appear in the SCExAO/CHARIS data (Figure 5.9) nor in the 2016 SCExAO/HiCIAO data. Given that both SCExAO data sets yield significantly deeper contrasts, we conclude that the emission peak seen in AO188 data is likely residual speckle

[4]SCExAO is a rapidly evolving platform that achieved a significant performance gain in the months after our data were taken (O. Guyon, T. Currie, 2018 unpublished). Thus, we defer discussion of limits on direct planet detections for a future HIP 79977 paper reporting new, substantially better data.

noise whose brightness highlights the stiff challenges in interpreting high-contrast imaging data where significant residual noise remains.

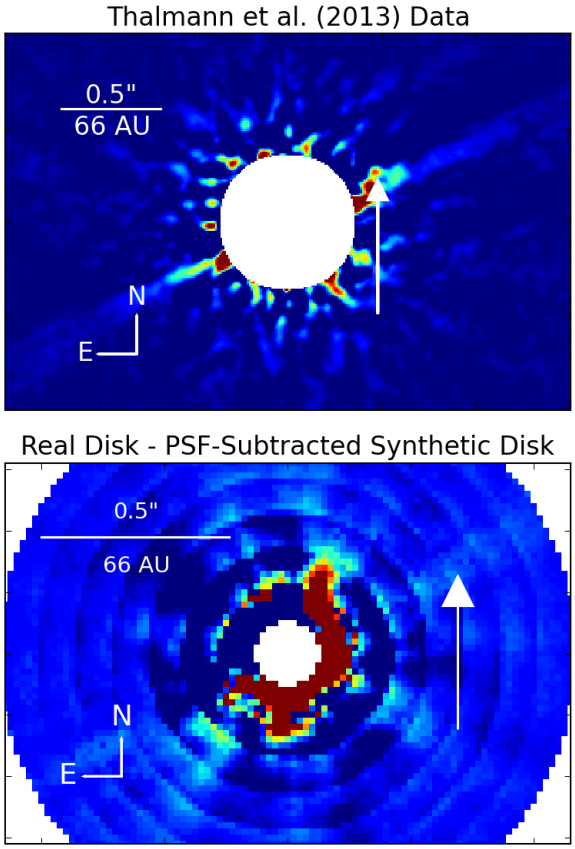

Figure 5.9 Top panel: reduction of the Thalmann et al. (2013) HIP 79977 data. An arrow points to the 4.6σ significance clump in their data. Bottom panel: our residuals after the forward-modeled best-fitting synthetic disk has been subtracted from the image. The same location is indicated with an arrow.

Table 5.2. Scattered Light Resolved Debris Disks Around 5-30 Myr old Stars

Star Name	Other Name	Age (Myr)	r_0 (au)	H-G Parameter g	Inclination i (°)	References
HD 146897	HIP 79977	11	53	0.6	84.5	Thalmann et al. (2013), this work
GSC 0739-00759	-	23	70	0.50	83	Sissa et al. (2018)
HD 15115	HIP 11360	<100	90	0.25	86.2	Kalas et al. (2007b); Mazoyer et al. (2014)
HD 36546	HIP 26062	3-10	85	0.85	75	Currie et al. (2017b)
HD 39060	β Pic	23	24–140	0.74	85.2	Smith & Terrile (1984), Millar-Blanchaer et al. (2015)
HD 95086	HIP 53524	17	100–300	-		Chauvin et al. (2018)
HD 106906	HIP 59960	13	65	0.6	85.3	Lagrange et al. (2016)
HD 109573	HR 4796A	10	77	–[a]	76.5	Schneider et al. (1999), Milli et al. (2017)
HD 110058	HIP 61782	17	32	-	$\sim$ 90?	Kasper et al. (2015)
HD 111520	HIP 62657	17	40-75	-	88?	Draper et al. (2016)

[a]Note that a Henyey-Greenstein scattering function fails to reproduce this disk's scattering phase function (Milli et al. 2017). See Discussion.

Note. — References are given for the first peer-reviewed publication of resolved optical/NIR imaging of the disk and the most recent paper that fitted for r_0 and g. We report the age and best-fitting values of g and r_0 from the second cited paper, unless there has only been one publication, in which case we use its values.

Table 5.3. Table 5.2 Continued.

Star Name	Other Name	Age (Myr)	r_0 (au)	H-G Parameter g	Inclination i (°)	References
HD 114082	HIP 64184	16	26-31[b]	0.07-0.23[b]	82.3	Wahhaj et al. (2016)
HD 115600	HIP 64995	15	48	0	79.5	Currie et al. (2015)
HD 120326	HIP 67497	16	59, 130[c]	0.82, -[c]	80	Bonnefoy et al. (2017)
HD 129590	HIP 72070	10-16	59	0.43	75	Matthews et al. (2017)
HD 131835	HIP 73145	15	90	0.15	75.1	Hung et al. (2015), Feldt et al. (2017)
HD 181327	HIP 95270	23	88	0.3[d]	31.7	Schneider et al. (2006), Schneider et al. (2014)
HD 197481	AU Mic	23	40-50	> 0.7[e]	~ 90?	Kalas et al. (2004), Graham et al. (2007)
TWA 7	CE Ant	10	25	0.63	13	Choquet et al. (2016), Olofsson et al. (2018)
TWA 25	V1249 Cen	7-13	78	0.7	75	Choquet et al. (2016)

[b]Wahhaj et al. (2016) reported values for three different data reductions, and we summarized their range of outcomes. Also, instead of parameterizing the disk with r_0, inside and outside of which the disk drops off in brightness, they assumed constant brightness between r_{in} and $r_{in}+\Delta r$, with falloff outside this range, and fit for both parameters. We reported their mean ring thickness $r_{in} + \frac{1}{2}\Delta r$.

[c]Bonnefoy et al. (2017) detected two rings around HIP 67497 and modeled for both of them.

[d]In their discovery paper, Schneider et al. (2006) reported that HD 181327 had $r_0 = 86$ au and $g = 0.3$. Later data modeled by Schneider et al. (2014) found $r_0 = 88$ au and surface brightness asymmetries that were not well parameterized by a Henyey-Greenstein scattering function$g$ (see also Stark et al. 2014).

[e]Au Mic has been extensively studied since Graham et al. (2007). However, publications since then then have stopped fitting for r_0 and g and have instead focused on characterization of finer structures in the disk (e.g. Boccaletti et al. 2018).

Table 5.2 casts the derived dust scattering properties and radius for HIP 79977's debris disk within the context of other scattered light resolved debris disks around young (5–30 Myr old) stars that have been observed at near-infrared wavelengths. Our derived value of the Henyey-Greenstein parameter ($g = 0.6$) falls in the middle to upper end of the range observed for other debris disks resolved in scattered light around 5–30 Myr old stars. The fiducial radius of the HIP 79977 disk is fairly typical of values measured for other debris disks. Taking both parameters together, the location and dust scattering properties of the HIP 79977 disk appear most similar to that for HD 106906 (Lagrange et al. 2016), GSC 07396-00759 (Sissa et al. 2018), and TWA 25 (Choquet et al. 2016). In particular, HD 106906's disk is likewise best modeled (within the Henyey-Greenstein formalism) by strongly forward-scattering dust and exhibits a clear east-west brightness asymmetry, similar to what our data hint at for HIP 79977.

However, HIP 79977's derived dust scattering parameter need not imply that its dust is *intrinsically* more forward-scattering than that of other young, resolved debris disks. Early studies employing a single Henyey-Greenstein scattering function implied neutral dust grains ($g \lesssim 0.16$ Schneider et al. 2009; Thalmann et al. 2011). However, more recent analysis based on extreme-AO observations probing small scattering angles showed that the disk's scattering function is not well-fit by a single Henyey-Greenstein parameterization but by a weighted combination of a strongly forward-scattering and strongly backward-scattering H-G component (Milli et al. 2017). Further improvements to scattering phase functions may require departures from standard Mie theory, e.g. Distribution of Hollow Spheres (e.g. Milli et al. 2017).

Furthermore, as shown in Hughes et al. (2018), the derived H-G g value strongly correlates with the range of probed scattering angles: the closer to the forward-scattering peak probed by the data, the higher the derived g value. Indeed, all of the ostensibly strongly forward-scattering disks listed in Table 5.2 are highly inclined, where such small angles are accessible. If there is little intrinsic difference in the scattering properties of young debris disks, then a single scattering phase function (e.g. Hong 1985) should be able

to reproduce the available data. On the other hand, higher quality data for other ostensibly neutral scattering disks like HD 115600 (Currie et al. 2015) should likewise reveal a forward-scattering component inconsistent with the Henyey-Greenstein formalism.

The disk flux in our images is scattered primarily by dust grains that are micron-sized and larger. Grains much smaller than our observing wavelengths scatter light isotropically, whereas larger grains preferentially forward scatter light (Hughes et al. 2018). Therefore, if the disk was dominated by grains with sizes smaller than a micron, we would not have observed the forward scattering that we did. Additionally, grains smaller than the observing wavelength scatter light in the Rayleigh regime and thereby produce blue colors, and except for marginally blue colors at certain radial separations, we do not observe this. The quality of our data limits our ability to make further inferences about the dust properties; the disk's dust properties could be better constrained by resolved spectra with higher signal to noise than our observations or multi-band polarimetric analysis.

A possible brightness asymmetry appears in our three bands (albeit at differing radii) and seems plausible from the 2016 HiCIAO data (Figure 5.1c) but will require confirmation with additional data sets of comparable or greater depth. If confirmed, there are several plausible physical explanations for this emission asymmetry. For example, the disk could be eccentric, and the preferential forward scattering of the dust causes the side of the disk closer to us to appear brighter. Alternatively, collisions of the debris in the disk could produce lumpiness and anisotrophies of brightness, and these would fade away on the dynamical timescale of the disk. While Engler et al. (2017) did not identify this brightness asymmetry, their data were at optical wavelengths and in polarized intensity.

The surface brightness power law measured in Section 5.5 is consistent with the disk model proposed by Strubbe & Chiang (2006). They suggest that at the fiducial radius $r = r_0$, micron-size grains are produced by the collisions of parent bodies with circular orbits. Outward of this radius lie grains large enough to remain gravitationally bound to the star but having orbits that have become eccentric due to stellar winds and radiation pressure from the star. This model produces a surface brightness profile that drops off

beyond the fiducial radius as $r^{-\alpha}$, where $\alpha \approx 4-5$. This agrees with our measured value of -4.1 ± 0.4.

Since the acquisition of the data presented in this paper, SCExAO has achieved significant performance improvements, reaching in excess of 90% Strehl at 1.6 μm for bright stars (Currie et al. 2018, in prep.). Thus, future, deeper SCExAO/CHARIS observations of HIP 79977 will enable a more robust characterization of the HIP 79977 disk's morphology and access the inner $0\farcs25$ with higher signal to noise. Multi-wavelength photometry obtained from these data can identify color gradients in the disk possibly traceable to different dust properties (e.g. Debes et al. 2008). These photometric points, complementary L_p imaging, and spatially-resolved spectra can provide crucial insights into how the morphology and composition of HIP 79977's debris disk compare to the Kuiper belt and other debris disks probing the epoch of icy planet formation (e.g. Currie et al. 2015; Rodigas et al. 2015; Milli et al. 2017).

Acknowledgments

We thank the anonymous referee for helpful suggestions that improved the quality of this work. We also thank Laurent Pueyo for helpful conversations about KLIP forward-modeling. TC is supported by a NASA Senior Postdoctoral Fellowship. MT is partly supported by the JSPS Grant-in-Aid (15H02063). SG is supported from NSF award AST 1106391 and NASA Roses APRA award NNX 13AC14G. The development of SCExAO was supported by the JSPS (Grant-in-Aid for Research #23340051, #26220704, #23103002), the Astrobiology Center (ABC) of the National Institutes of Natural Sciences, Japan, the Mt Cuba Foundation and the directors contingency fund at Subaru Telescope. CHARIS was built at Princeton University in collaboration with the National Astronomical Observatory of Japan under a Grant-in-Aid for Scientific Research on Innovative Areas from MEXT of the Japanese government (#23103002). We wish to emphasize the pivotal cultural role and reverence that the summit of Maunakea has always had within the indigenous Hawaiian

community. We are most fortunate to have the privilege to conduct scientific observations from this mountain.

References

Augereau, J. C., Lagrange, A. M., Mouillet, D., Papaloizou, J. C. B., & Grorod, P. A. 1999, A&A, 348, 557

Boccaletti, A., Sezestre, E., Lagrange, A. M., Thébault, P., Gratton, R., Langlois, M., Thalmann, C., Janson, M., Delorme, P., Augereau, J. C., Schneider, G., Milli, J., Grady, C., Debes, J., Kral, Q., Olofsson, J., Carson, J., Maire, A. L., Henning, T., Wisniewski, J., Schlieder, J., Dominik, C., Desidera, S., Ginski, C., Hines, D., Ménard, F., Mouillet, D., Pawellek, N., Vigan, A., Lagadec, E., Avenhaus, H., Beuzit, J. L., Biller, B., Bonavita, M., Bonnefoy, M., Brandner, W., Cantalloube, F., Chauvin, G., Cheetham, A., Cudel, M., Gry, C., Daemgen, S., Feldt, M., Galicher, R., Girard, J., Janin- Potiron, P., Kasper, M., Le Coroller, H., Mesa, D., Peretti, S., Perrot, C., Samland, M., Sissa, E., Wildi, F., Rochat, S., Stadler, E., Gluck, L., Origné, A., Llored, M., Baudoz, P., Rousset, G., Martinez, P., & Rigal, F. 2018, ArXiv e-prints, arXiv:1803.05354

Bonnefoy, M., Milli, J., Ménard, F., Vigan, A., Lagrange, A. M., Delorme, P., Boccaletti, A., Lazzoni, C., Galicher, R., Desidera, S., Chauvin, G., Augereau, J. C., Mouillet, D., Pinte, C., van der Plas, G., Gratton, R., Beust, H., & Beuzit, J. L. 2017, A&A, 597, L7

Brandt, T. D., McElwain, M. W., Turner, E. L., Abe, L., Brandner, W., Carson, J., Egner, S., Feldt, M., Golota, T., Goto, M., Grady, C. A., Guyon, O., Hashimoto, J., Hayano, Y., Hayashi, M., Hayashi, S., Henning, T., Hodapp, K. W., Ishii, M., Iye, M., Janson, M., Kandori, R., Knapp, G. R., Kudo, T., Kusakabe, N., Kuzuhara, M., Kwon, J., Matsuo,

T., Miyama, S., Morino, J.-I., Moro-Martín, A., Nishimura, T., Pyo, T.-S., Serabyn, E., Suto, H., Suzuki, R., Takami, M., Takato, N., Terada, H., Thalmann, C., Tomono, D., Watanabe, M., Wisniewski, J. P., Yamada, T., Takami, H., Usuda, T., & Tamura, M. 2013, ApJ, 764, 183

Brandt, T. D., Rizzo, M., Groff, T., Chilcote, J., Greco, J. P., Kasdin, N. J., Limbach, M. A., Galvin, M., Loomis, C., Knapp, G., McElwain, M. W., Jovanovic, N., Currie, T., Mede, K., Tamura, M., Takato, N., & Hayashi, M. 2017, Journal of Astronomical Telescopes, Instruments, and Systems, 3, 048002

Chauvin, G., Gratton, R., Bonnefoy, M., Lagrange, A. M., de Boer, J., Vigan, A., Beust, H., Lazzoni, C., Boccaletti, A., Galicher, R., Desidera, S., Delorme, P., Keppler, M., Lannier, J., Maire, A. L., Mesa, D., Meunier, N., Kral, Q., Henning, T., Menard, F., Moor, A., Avenhaus, H., Bazzon, A., Janson, M., Beuzit, J. L., Bhowmik, T., Bonavita, M., Borgniet, S., Brandner, W., Cheetham, A., Cudel, M., Feldt, M., Fontanive, C., Ginski, C., Hagelberg, J., Janin-Potiron, P., Lagadec, E., Langlois, M., Le Coroller, H., Messina, S., Meyer, M., Mouillet, D., Peretti, S., Perrot, C., Rodet, L., Samland, M., Sissa, E., Olofsson, J., Salter, G., Schmidt, T., Zurlo, A., Milli, J., van Boekel, R., Quanz, S., Wilson, P. A., Feautrier, P., Le Mignant, D., Perret, D., Ramos, J., & Rochat, S. 2018, ArXiv e-prints, arXiv:1801.05850

Chen, C. H., Mamajek, E. E., Bitner, M. A., Pecaut, M., Su, K. Y. L., & Weinberger, A. J. 2011, ApJ, 738

Choquet, É., Perrin, M. D., Chen, C. H., Soummer, R., Pueyo, L., Hagan, J. B., Gofas-Salas, E., Rajan, A., Golimowski, D. A., Hines, D. C., Schneider, G., Mazoyer, J., Augereau, J.-C., Debes, J., Stark, C. C., Wolff, S., N'Diaye, M., & Hsiao, K. 2016, ApJ, 817, L2

Currie, T., Brittain, S., Grady, C. A., Kenyon, S. J., & Muto, T. 2017a, Research Notes of the American Astronomical Society, 1, 40

Currie, T., Burrows, A., Itoh, Y., Matsumura, S., Fukagawa, M., Apai, D., Madhusudhan, N., Hinz, P. M., Rodigas, T. J., Kasper, M., Pyo, T.-S., & Ogino, S. 2011, ApJ, 729, 128

Currie, T., Debes, J., Rodigas, T. J., Burrows, A., Itoh, Y., Fukagawa, M., Kenyon, S. J., Kuchner, M., & Matsumura, S. 2012, ApJ, 760, L32

Currie, T., Guyon, O., Tamura, M., Kudo, T., Jovanovic, N., Lozi, J., Schlieder, J. E., Brandt, T. D., Kuhn, J., Serabyn, E., Janson, M., Carson, J., Groff, T., Kasdin, N. J., McElwain, M. W., Singh, G., Uyama, T., Kuzuhara, M., Akiyama, E., Grady, C., Hayashi, S., Knapp, G., Kwon, J.-m., Oh, D., Wisniewski, J., Sitko, M., & Yang, Y. 2017b, ApJ, 836, L15

Currie, T., Kasdin, N. J., Groff, T. D., Lozi, J., Jovanovic, N., Guyon, O., Brandt, T., Martinache, F., Chilcote, J., Skaf, N., Kuhn, J., Pathak, P., & Kudo, T. 2018, Publications of the Astronomical Society of the Pacific, 130, 044505

Currie, T., Kenyon, S. J., Balog, Z., Rieke, G., Bragg, A., & Bromley, B. 2008, ApJ, 672, 558

Currie, T., Lisse, C. M., Kuchner, M., Madhusudhan, N., Kenyon, S. J., Thalmann, C., Carson, J., & Debes, J. 2015, ApJ, 807, L7

Currie, T., Muto, T., Kudo, T., Honda, M., Brandt, T. D., Grady, C., Fukagawa, M., Burrows, A., Janson, M., Kuzuhara, M., McElwain, M. W., Follette, K., Hashimoto, J., Henning, T., Kandori, R., Kusakabe, N., Kwon, J., Mede, K., Morino, J.-i., Nishikawa, J., Pyo, T.-S., Serabyn, G., Suenaga, T., Takahashi, Y., Wisniewski, J., & Tamura, M. 2014, ApJ, 796, L30

Debes, J. H., Weinberger, A. J., & Schneider, G. 2008, ApJ, 673, L191

Draper, Z. H., Duchêne, G., Millar-Blanchaer, M. A., Matthews, B. C., Wang, J. J., Kalas, P., Graham, J. R., Padgett, D., Ammons, S. M., Bulger, J., Chen, C., Chilcote, J. K., Doyon, R., Fitzgerald, M. P., Follette, K. B., Gerard, B., Greenbaum, A. Z., Hibon,

P., Hinkley, S., Macintosh, B., Ingraham, P., Lafrenière, D., Marchis, F., Marois, C., Nielsen, E. L., Oppenheimer, R., Patel, R., Patience, J., Perrin, M., Pueyo, L., Rajan, A., Rameau, J., Sivaramakrishnan, A., Vega, D., Ward-Duong, K., & Wolff, S. G. 2016, ApJ, 826, 147

Engler, N., Schmid, H. M., Thalmann, C., Boccaletti, A., Bazzon, A., Baruffolo, A., Beuzit, J. L., Claudi, R., Costille, A., Desidera, S., Dohlen, K., Dominik, C., Feldt, M., Fusco, T., Ginski, C., Gisler, D., Girard, J. H., Gratton, R., Henning, T., Hubin, N., Janson, M., Kasper, M., Kral, Q., Langlois, M., Lagadec, E., Ménard, F., Meyer, M. R., Milli, J., Mouillet, D., Olofsson, J., Pavlov, A., Pragt, J., Puget, P., Quanz, S. P., Roelfsema, R., Salasnich, B., Siebenmorgen, R., Sissa, E., Suarez, M., Szulagyi, J., Turatto, M., Udry, S., & Wildi, F. 2017, A&A, 607, A90

Feldt, M., Olofsson, J., Boccaletti, A., Maire, A. L., Milli, J., Vigan, A., Langlois, M., Henning, T., Moor, A., Bonnefoy, M., Wahhaj, Z., Desidera, S., Gratton, R., Kóspál, Á., Abraham, P., Menard, F., Chauvin, G., Lagrange, A. M., Mesa, D., Salter, G., Buenzli, E., Lannier, J., Perrot, C., Peretti, S., & Sissa, E. 2017, A&A, 601, A7

Gaia Collaboration. 2018, VizieR Online Data Catalog, I/345

Garcia, E. V., Currie, T., Guyon, O., Stassun, K. G., Jovanovic, N., Lozi, J., Kudo, T., Doughty, D., Schlieder, J., Kwon, J., Uyama, T., Kuzuhara, M., Carson, J. C., Nakagawa, T., Hashimoto, J., Kusakabe, N., Abe, L., Brandner, W., Brandt, T. D., Feldt, M., Goto, M., Grady, C. A., Hayano, Y., Hayashi, M., Hayashi, S. S., Henning, T., Hodapp, K. W., Ishii, M., Iye, M., Janson, M., Kandori, R., Knapp, G. R., Matsuo, T., McElwain, M. W., Miyama, S., Morino, J.-I., Moro-Martin, A., Nishimura, T., Pyo, T.-S., Serabyn, E., Suenaga, T., Suto, H., Suzuki, R., Takahashi, Y. H., Takami, H., Takami, M., Takato, N., Terada, H., Thalmann, C., Turner, E. L., Watanabe, M., Wisniewski, J., Yamada, T., Usuda, T., & Tamura, M. 2017, ApJ, 834, 162

Golimowski, D. A., Ardila, D. R., Krist, J. E., Clampin, M., Ford, H. C., Illingworth, G. D., Bartko, F., Benítez, N., Blakeslee, J. P., Bouwens, R. J., Bradley, L. D., Broadhurst, T. J., Brown, R. A., Burrows, C. J., Cheng, E. S., Cross, N. J. G., Demarco, R., Feldman, P. D., Franx, M., Goto, T., Gronwall, C., Hartig, G. F., Holden, B. P., Homeier, N. L., Infante, L., Jee, M. J., Kimble, R. A., Lesser, M. P., Martel, A. R., Mei, S., Menanteau, F., Meurer, G. R., Miley, G. K., Motta, V., Postman, M., Rosati, P., Sirianni, M., Sparks, W. B., Tran, H. D., Tsvetanov, Z. I., White, R. L., Zheng, W., & Zirm, A. W. 2006, AJ, 131, 3109

Graham, J. R., Kalas, P. G., & Matthews, B. C. 2007, ApJ, 654, 595

Groff, T. D., Peters, M. A., Kasdin, N. J., Knapp, G., Galvin, M., Carr, M., McElwain, M. W., Brandt, T., Janson, M., Gunn, J. E., Lupton, R., Guyon, O., Martinache, F., Jovanovic, N., Hayashi, M., & Takato, N. 2013, in Proc. SPIE, Vol. 8864, Techniques and Instrumentation for Detection of Exoplanets VI, 88640H

Henyey, L. G. & Greenstein, J. L. 1941, ApJ, 93, 70

Hong, S. S. 1985, A&A, 146, 67

Hughes, A. M., Duchene, G., & Matthews, B. 2018, ArXiv e-prints, arXiv:1802.04313

Hung, L.-W., Duchêne, G., Arriaga, P., Fitzgerald, M. P., Maire, J., Marois, C., Millar-Blanchaer, M. A., Bruzzone, S., Rajan, A., Pueyo, L., Kalas, P. G., De Rosa, R. J., Graham, J. R., Konopacky, Q., Wolff, S. G., Ammons, S. M., Chen, C. H., Chilcote, J. K., Draper, Z. H., Esposito, T. M., Gerard, B., Goodsell, S., Greenbaum, A., Hibon, P., Hinkley, S., Macintosh, B., Marchis, F., Metchev, S., Nielsen, E. L., Oppenheimer, R., Patience, J. L., Perrin, M. D., Rantakyrö, F. T., Sivaramakrishnan, A., Wang, J. J., Ward-Duong, K., & Wiktorowicz, S. J. 2015, ApJ, 815, L14

Jovanovic, N., Guyon, O., Martinache, F., Pathak, P., Hagelberg, J., & Kudo, T. 2015a, ApJ, 813, L24

Jovanovic, N., Martinache, F., Guyon, O., Clergeon, C., Singh, G., Kudo, T., Garrel, V., Newman, K., Doughty, D., Lozi, J., Males, J., Minowa, Y., Hayano, Y., Takato, N., Morino, J., Kuhn, J., Serabyn, E., Norris, B., Tuthill, P., Schworer, G., Stewart, P., Close, L., Huby, E., Perrin, G., Lacour, S., Gauchet, L., Vievard, S., Murakami, N., Oshiyama, F., Baba, N., Matsuo, T., Nishikawa, J., Tamura, M., Lai, O., Marchis, F., Duchene, G., Kotani, T., & Woillez, J. 2015b, PASP, 127, 890

Kalas, P., Duchene, G., Fitzgerald, M. P., & Graham, J. R. 2007a, ApJ, 671, L161

Kalas, P., Fitzgerald, M. P., & Graham, J. R. 2007b, ApJ, 661, L85

Kalas, P., Graham, J. R., & Clampin, M. 2005, Nature, 435, 1067

Kalas, P., Graham, J. R., Clampin, M. C., & Fitzgerald, M. P. 2006, ApJ, 637, L57

Kalas, P., Liu, M. C., & Matthews, B. C. 2004, Science, 303, 1990

Kasper, M., Apai, D., Wagner, K., & Robberto, M. 2015, ApJ, 812, L33

Kenyon, S. J. & Bromley, B. C. 2008, ApJS, 179, 451

Lagrange, A.-M., Boccaletti, A., Milli, J., Chauvin, G., Bonnefoy, M., Mouillet, D., Augereau, J. C., Girard, J. H., Lacour, S., & Apai, D. 2012, A&A, 542, A40

Lagrange, A.-M., Bonnefoy, M., Chauvin, G., Apai, D., Ehrenreich, D., Boccaletti, A., Gratadour, D., Rouan, D., Mouillet, D., Lacour, S., & Kasper, M. 2010, Science, 329, 57

Lagrange, A. M., Langlois, M., Gratton, R., Maire, A. L., Milli, J., Olofsson, J., Vigan, A., Bailey, V., Mesa, D., Chauvin, G., Boccaletti, A., Galicher, R., Girard, J. H., Bonnefoy, M., Samland, M., Menard, F., Henning, T., Kenworthy, M., Thalmann, C., Beust, H., Beuzit, J. L., Brandner, W., Buenzli, E., Cheetham, A., Janson, M., le Coroller, H., Lannier, J., Mouillet, D., Peretti, S., Perrot, C., Salter, G., Sissa, E., Wahhaj, Z., Abe, L., Desidera, S., Feldt, M., Madec, F., Perret, D., Petit, C., Rabou, P., Soenke, C., & Weber, L. 2016, A&A, 586, L8

Marois, C., Macintosh, B., Barman, T., Zuckerman, B., Song, I., Patience, J., Lafrenière, D., & Doyon, R. 2008, Science, 322, 1348

Matthews, E., Hinkley, S., Vigan, A., Kennedy, G., Rizzuto, A., Stapelfeldt, K., Mawet, D., Booth, M., Chen, C., & Jang-Condell, H. 2017, ApJ, 843, L12

Mazoyer, J., Boccaletti, A., Augereau, J. C., Lagrange, A. M., Galicher, R., & Baudoz, P. 2014, A&A, 569, A29

Millar-Blanchaer, M. A., Graham, J. R., Pueyo, L., Kalas, P., Dawson, R. I., Wang, J., Perrin, M. D., moon, D.-S., Macintosh, B., Ammons, S. M., Barman, T., Cardwell, A., Chen, C. H., Chiang, E., Chilcote, J., Cotten, T., De Rosa, R. J., Draper, Z. H., Dunn, J., Duchêne, G., Esposito, T. M., Fitzgerald, M. P., Follette, K. B., Goodsell, S. J., Greenbaum, A. Z., Hartung, M., Hibon, P., Hinkley, S., Ingraham, P., Jensen-Clem, R., Konopacky, Q., Larkin, J. E., Long, D., Maire, J., Marchis, F., Marley, M. S., Marois, C., Morzinski, K. M., Nielsen, E. L., Palmer, D. W., Oppenheimer, R., Poyneer, L., Rajan, A., Rantakyrö, F. T., Ruffio, J.-B., Sadakuni, N., Saddlemyer, L., Schneider, A. C., Sivaramakrishnan, A., Soummer, R., Thomas, S., Vasisht, G., Vega, D., Wallace, J. K., Ward-Duong, K., Wiktorowicz, S. J., & Wolff, S. G. 2015, ApJ, 811, 18

Milli, J., Vigan, A., Mouillet, D., Lagrange, A.-M., Augereau, J.-C., Pinte, C., Mawet, D., Schmid, H. M., Boccaletti, A., Matrà, L., Kral, Q., Ertel, S., Chauvin, G., Bazzon, A., Ménard, F., Beuzit, J.-L., Thalmann, C., Dominik, C., Feldt, M., Henning, T., Min, M., Girard, J. H., Galicher, R., Bonnefoy, M., Fusco, T., de Boer, J., Janson, M., Maire, A.-L., Mesa, D., Schlieder, J. E., & SPHERE Consortium. 2017, A&A, 599, A108

Minowa, Y., Hayano, Y., Oya, S., Watanabe, M., Hattori, M., Guyon, O., Egner, S., Saito, Y., Ito, M., Takami, H., Garrel, V., Colley, S., Golota, T., & Iye, M. 2010, in Society of Photo-Optical Instrumentation Engineers (SPIE) Conference Series, Vol. 7736, Society of Photo-Optical Instrumentation Engineers (SPIE) Conference Series, 3

Mustill, A. J. & Wyatt, M. C. 2009, MNRAS, 399, 1403

Nielsen, E. L., Liu, M. C., Wahhaj, Z., Biller, B. A., Hayward, T. L., Boss, A., Bowler, B., Kraus, A., Shkolnik, E. L., Tecza, M., Chun, M., Clarke, F., Close, L. M., Ftaclas, C., Hartung, M., Males, J. R., Reid, I. N., Skemer, A. J., Alencar, S. H. P., Burrows, A., de Gouveia Dal Pino, E., Gregorio-Hetem, J., Kuchner, M., Thatte, N., & Toomey, D. W. 2012, ApJ, 750, 53

Olofsson, J., van Holstein, R. G., Boccaletti, A., Janson, M., Thébault, P., Gratton, R., Lazzoni, C., Kral, Q., Bayo, A., Canovas, H., Caceres, C., Ginski, C., Pinte, C., Asensio-Torres, R., Chauvin, G., Desidera, S., Henning, T., Langlois, M., Milli, J., Schlieder, J. E., Schreiber, M. R., Augereau, J. C., Bonnefoy, M., Buenzli, E., Brandner, W., Durkan, S., Engler, N., Feldt, M., Godoy, N., Grady, C., Hagelberg, J., Lagrange, A. M., Lannier, J., Ligi, R., Maire, A. L., Mawet, D., Ménard, F., Mesa, D., Mouillet, D., Peretti, S., Perrot, C., Salter, G., Schmidt, T., Sissa, E., Thalmann, C., Vigan, A., Abe, L., Feautrier, P., Le Mignant, D., Moulin, T., Pavlov, A., Rabou, P., Rousset, G., & Roux, A. 2018, ArXiv e-prints, arXiv:1804.01929

Pecaut, M. J., Mamajek, E. E., & Bubar, E. J. 2012, The Astrophysical Journal, 746, 154

Peters, M. A., Groff, T., Kasdin, N. J., McElwain, M. W., Galvin, M., Carr, M. A., Lupton, R., Gunn, J. E., Knapp, G., Gong, Q., Carlotti, A., Brandt, T., Janson, M., Guyon, O., Martinache, F., Hayashi, M., & Takato, N. 2012, in Proc. SPIE, Vol. 8446, Ground-based and Airborne Instrumentation for Astronomy IV, 84467U

Pueyo, L. 2016, ApJ, 824, 117

Rodigas, T. J., Debes, J. H., Hinz, P. M., Mamajek, E. E., Pecaut, M. J., Currie, T., Bailey, V., Defrere, D., De Rosa, R. J., Hill, J. M., Leisenring, J., Schneider, G., Skemer, A. J., Skrutskie, M., Vaitheeswaran, V., & Ward-Duong, K. 2014, ApJ, 783, 21

Rodigas, T. J., Stark, C. C., Weinberger, A., Debes, J. H., Hinz, P. M., Close, L., Chen, C., Smith, P. S., Males, J. R., Skemer, A. J., Puglisi, A., Follette, K. B., Morzinski, K., Wu,

Y.-L., Briguglio, R., Esposito, S., Pinna, E., Riccardi, A., Schneider, G., & Xompero, M. 2015, ApJ, 798, 96

Schneider, G., Grady, C. A., Hines, D. C., Stark, C. C., Debes, J. H., Carson, J., Kuchner, M. J., Perrin, M. D., Weinberger, A. J., Wisniewski, J. P., Silverstone, M. D., Jang-Condell, H., Henning, T., Woodgate, B. E., Serabyn, E., Moro-Martin, A., Tamura, M., Hinz, P. M., & Rodigas, T. J. 2014, AJ, 148, 59

Schneider, G., Silverstone, M. D., & Hines, D. C. 2005, ApJ, 629, L117

Schneider, G., Silverstone, M. D., Hines, D. C., Augereau, J.-C., Pinte, C., Ménard, F., Krist, J., Clampin, M., Grady, C., Golimowski, D., Ardila, D., Henning, T., Wolf, S., & Rodmann, J. 2006, ApJ, 650, 414

Schneider, G., Smith, B. A., Becklin, E. E., Koerner, D. W., Meier, R., Hines, D. C., Lowrance, P. J., Terrile, R. J., Thompson, R. I., & Rieke, M. 1999, ApJ, 513, L127

Schneider, G., Weinberger, A. J., Becklin, E. E., Debes, J. H., & Smith, B. A. 2009, AJ, 137, 53

Service, M., Lu, J. R., Campbell, R., Sitarski, B. N., Ghez, A. M., & Anderson, J. 2016, PASP, 128, 095004

Sissa, E., Olofsson, J., Vigan, A., Augereau, J. C., D'Orazi, V., Desidera, S., Gratton, R., Rigliaco, M. L. E., Boccaletti, A., Kral, Q., Lazzoni, C., Mesa, D., Messina, S., Sezestre, E., Thébault, P., Zurlo, A., Bhowmik, T., Bonnefoy, M., Chauvin, G., Feldt, M., Hagelberg, J., Lagrange, A.-M., Janson, M., Maire, A.-L., Ménard, F., Schlieder, J., Schmidt, T., Szulágyi, J., Stadler, E., Deboulbé, D. M. A., Feautrier, P., Ramos, J., & Rigal, R. 2018, ArXiv e-prints

Smith, B. A. & Terrile, R. J. 1984, Science, 226, 1421

Soummer, R., Perrin, M. D., Pueyo, L., Choquet, É., Chen, C., Golimowski, D. A., Hagan, J. B., Mittal, T., Moerchen, M., N'Diaye, M., Rajan, A., Wolff, S., Debes, J., Hines, D. C., & Schneider, G. 2014, ApJ, 786, L23

Soummer, R., Pueyo, L., & Larkin, J. 2012, ApJ, 755, L28

Stark, C. C., Schneider, G., Weinberger, A. J., Debes, J. H., Grady, C. A., Jang-Condell, H., & Kuchner, M. J. 2014, ApJ, 789, 58

Strubbe, L. E. & Chiang, E. I. 2006, ApJ, 648, 652

Thalmann, C., Janson, M., Buenzli, E., Brandt, T. D., Wisniewski, J. P., Dominik, C., Carson, J., McElwain, M. W., Currie, T., Knapp, G. R., Moro-Martín, A., Usuda, T., Abe, L., Brandner, W., Egner, S., Feldt, M., Golota, T., Goto, M., Guyon, O., Hashimoto, J., Hayano, Y., Hayashi, M., Hayashi, S., Henning, T., Hodapp, K. W., Ishii, M., Iye, M., Kandori, R., Kudo, T., Kusakabe, N., Kuzuhara, M., Kwon, J., Matsuo, T., Mayama, S., Miyama, S., Morino, J.-I., Nishimura, T., Pyo, T.-S., Serabyn, E., Suto, H., Suzuki, R., Takami, M., Takato, N., Terada, H., Tomono, D., Turner, E. L., Watanabe, M., Yamada, T., Takami, H., & Tamura, M. 2013, AJ, 763, L29

Thalmann, C., Janson, M., Buenzli, E., Brandt, T. D., Wisniewski, J. P., Moro-Martín, A., Usuda, T., Schneider, G., Carson, J., McElwain, M. W., Grady, C. A., Goto, M., Abe, L., Brandner, W., Dominik, C., Egner, S., Feldt, M., Fukue, T., Golota, T., Guyon, O., Hashimoto, J., Hayano, Y., Hayashi, M., Hayashi, S., Henning, T., Hodapp, K. W., Ishii, M., Iye, M., Kandori, R., Knapp, G. R., Kudo, T., Kusakabe, N., Kuzuhara, M., Matsuo, T., Miyama, S., Morino, J.-I., Nishimura, T., Pyo, T.-S., Serabyn, E., Suto, H., Suzuki, R., Takahashi, Y. H., Takami, M., Takato, N., Terada, H., Tomono, D., Turner, E. L., Watanabe, M., Yamada, T., Takami, H., & Tamura, M. 2011, ApJ, 743, L6

van Leeuwen, F. 2007, A&A, 474, 653

Wahhaj, Z., Milli, J., Kennedy, G., Ertel, S., Matrà, L., Boccaletti, A., del Burgo, C., Wyatt, M., Pinte, C., Lagrange, A.-M., Absil, O., Choquet, E., Gómez González, C. A.,

Kobayashi, H., Mawet, D., Mouillet, D., Pueyo, L., Dent, W. R. F., Augereau, J.-C., & Girard, J. 2016, A&A, 596, L4

Wyatt, M. C. 2008, ARA&A, 46, 339

Appendix A

The Codes used to Produce the Preceding Results

A repository of the codes Sean produced during his graduate school career can be viewed at `https://github.com/seangoebelgradschool?tab=repositories`. Most of the codes contain some self-documentation. Sean's codes were primarily written in (decreasing order of prevalence) Python 2.7, IDL 7.1, or Bash. This section contains brief descriptions of a selection of his codes.

Below are some of the codes used to produce the content of Chapter 2 ("Overview of SAPHIRA for AO Applications").

- `scexao/rrrfail.py` produced Figure 2.1.
- `scexao/badbias.py` and `scexao/badbias_analysis.py` were used to produce Figure 2.2.
- `scexao/rrreduce.py` was widely used to form median dark/bias frames and subtract them from the data frames in order to reduce read-reset data.
- `scexao/powspecproper.py` took into account how the detector spent its time during clocking (including the periods at ends of rows and frames) in order to string together frames and compute the power spectrum of noise common to all 32 outputs over frequencies from 1 Hz to 500 kHz. An example result of this process was shown in Figure 2.3.

- `diodecapacitanceplot.py` produced Figure 2.4. The data plotted were measured by Ian Baker of Leonardo and sent by private correspondence.

Below are some of the codes used to produce the content of Chapter 3 ("Commissioning of Cryogenic Preamplifiers for SAPHIRA").

- `scexao/powspecproper.py` took into account how the detector spent its time during clocking (including the periods at ends of rows and frames) in order to string together frames and compute the power spectrum of noise common to all 32 outputs over frequencies from 1 Hz to 500 kHz. An example result of this process was shown in Figure 3.1.

- `scexao/voltgain.py` and `laptop/detectors/saphira/2018spie/voltgain_complicated.py` measured volt gains at SCExAO and in the lab, respectively. `laptop/detectors/saphira/2018spie/vgprettyplot.py` took their results and plotted them in Figures 3.4 and 3.6.

Below are some of the codes used to produce the content of Chapter 4 ("Measurements of Speckle Lifetimes in Near-Infrared Extreme Adaptive Optics Images for Optimizing Focal Plane Wavefront Control").

- `scexao/rrreduce.py` was widely used to form median dark/bias frames and subtract them from the data frames in order to reduce read-reset data.

- `scexao/tiptiltastrometric.py` calculated offsets between frames in a user-specified image cube by locating the artificial astrometric speckles. It then shifted the images in order to remove tips/tilts and saved them in a new file. In my testing, this was slightly more accurate than using the cross-correlation method, but also significantly slower.

- `scexao/tiptilt4.py` calculated offsets between frames in a user-specified image cube by cross-correlating frames. It then shifted the images in order to remove tips/tilts and saved them in a new file.

- `scexao/alignmulti.py` computed the shifts from one frame to the next using cross-correlations and saved them in text files. Because this was computationally intensive and involved millions of images, it multi-threaded it for improved performance.

- `scexao/tiptilt5.py` read in the offsets produced by `alignmulti.py`, performed some smoothing, shifted the images in order to remove the tip/tilt, and saved the aligned images.

- `scexao/specklelives5.py` produced the plots shown in Section 4.3.2

- `scexao/corrcoeffs.py` was initially written to compute the Pearson's correlation coefficients discussed in Section 4.4.2.

- `scexao/corrcoeffs2.py` computed the Pearson's correlation coefficients discussed in Section 4.4.2. This was forked from `scexao/corrcoeffs.py` and optimized for speed, but it is less human-understandable. When compared to `scexao/corrcoeffs.py`, this uses less RAM, computes quantities ahead of time and stores them in order to not re-compute them, and has the ability to multi-thread its calculations across many CPUs.

- `scexao/specklelivesfig2.py` produced Figure 4.1.

Below are some of the codes used to produce the content of Chapter 5 ("SCExAO/CHARIS Near-IR High-Contrast Imaging and Integral Field Spectroscopy of the HIP 79977 Debris Disk").

- `scexaodisks/partialsub/charis_klip_disk_fwdmod.pro` performs the forward modeling process. It reads in a selection of synthetic disk models and propagates

them through the KLIP PSF-subtraction process (`charis_subsklip.pro`) using the eigenvalues and eigenvectors saved from the processing of the actual data.

- `scexaodisks/psfsub/charis_subsklip.pro` performs the KLIP PSF-subtraction of a user-specified image cube using a user-specified PSF.

- `scexaodisks/sean/klipgrid.pro` calls `charis_subsklip.pro` for multiple models in order to check the effects of different reduction settings.

- `scexaodisks/sean/scrapefitsinfo.pro` reads the header information of all the forward-modeled synthetic models in order to compare them to and outputs it to a text file in order to compare them to the actual data and decide which synthetic disks are well-fitting.

- `scexaodisks/specphotcal/calc_disk_sb.pro` calculates the surface brightness along the disk spine. This is used in conjunction with `sbplot.py` and `sbplot2.py` to generate Figures 5.7 and 5.8.

- `scexaodisks/syndisks/call_grater.pro`, `scexaodisks/syndisks/scimage.pro`, and `scexaodisks/syndisks/density.pro` produce a synthetic model disk using user-specified parameters.

- `scexaodisks/syndisks/grater_grid.pro` calls `call_grater.pro` in order to produce synthetic model disks for a range of user-specified parameters. This has a deeply scandalous 11 nested for loops, so viewer discretion is advised.

- `planet.py` produced Figure 5.9.

- `sbplot.py` used the data from `calc_disk_sb.pro` to produce Figure 5.7.

- `spinefit.py` performed a fit to the spine of the disk in order to find its trace. This was then used in the surface brightness calculations.

- `contours.py` plotted the average χ^2 of all disk parameters against all other disk parameters, producing a number of interesting images. One of them was shown in Figure 5.5.
- `fwmodeling.py` produced Figure 5.4.
- `plthists.py` produced Figure 5.6.
- `showroi.py` produced Figure 5.3.
- `diskcomparison.py` produced an alternative version of Figure 5.1
- `makediskpics.py` produced Figure 5.2.
- `sbplot2.py` used the data from `calc_disk_sb.pro` to produce Figure 5.8.
- `snrcompare.py` compares the per-channel SNR of PSF-subtracted disks produced using various KLIP parameters in order to find the best set of parameters.

Below are other useful codes.

- `scexao/pbserver/gui_pizzabox` provides an easy user interface for operating the Rev. 3 Pizza Box, which is what was used at SCExAO deployments.
- `scexao/pbserver/gui_saphira` provides an easy user interface for starting and stopping image saving at SCExAO, viewing the live images, and viewing data statistics.
- `scexao/pbserver/temp.py` queries the Lakeshore temperature controller for SAPHIRA's temperature and prints it to the screen.
- `scexao/pbserver/temp_notify2.py` is meant to be called from a cronjob. It queries the Lakeshore temperature controller for SAPHIRA's temperature. If the temperature is out of range, it emails the user a warning. This proved infinitely useful during the many power surges at Subaru which regularly caused the detector to start to warm.